Julian Köpfler

On Topological Mechanics of 3D Chiral Metamaterials

On Topological Mechanics
of 3D Chiral Metamaterials

Zur Erlangung des akademischen Grades eines
DOKTORS DER NATURWISSENSCHAFTEN (Dr. rer. nat.)
von der KIT-Fakultät für Physik des
Karlsruher Instituts für Technologie (KIT)

genehmigte

DISSERTATION

von

M. Sc. Julian Köpfler
geboren in Titisee-Neustadt

Contents

PUBLICATIONS

PARTS OF THIS THESIS HAVE ALREADY BEEN PUBLISHED . . .
. . . in scientific journals:

- J. Köpfler, T. Frenzel, M. Kadic, J. Schmalian, and M. Wegener, "Topologically Protected Twist Edge States for a Resonant Mechanical Laser-Beam Scanner", *Phys. Rev. Appl.* **11**, 034059 (2019).

- J. Köpfler, T. Frenzel, J. Schmalian, and M. Wegener, "Fused-Silica 3D Chiral Metamaterials via Helium-Assisted Micro-Casting Supporting Topologically Protected Twist Edge Resonances with High Mechanical Quality Factors", *Adv. Mater.* **33**, 2103205 (2021).

- T. Frenzel*, J. Köpfler*, A. Naber, and M. Wegener, "Detecting Atomic-Scale Displacements by Optical-Image Cross-Correlation Analysis and 3D Printed Marker Arrays", *Sci. Rep.* **11**, 2304 (2021). *equally contributing authors.*

. . . at scientific conferences (only own presentations):

- J. Köpfler, T. Frenzel, M. Kadic, J. Schmalian, and M. Wegener, "Design of a Resonant Laser Beam Scanner Based on a Topologically Protected Twist Edge State", MRS Fall Meeting, United States of America, Boston, November 2018.

- J. Köpfler, T. Frenzel, M. Kadic, J. Schmalian, and M. Wegener, "Resonant Laser-Beam Scanner Based on Topologically Protected Twist Edge-States of Three-Dimensional Chiral Metamaterials", Metamaterials Congress, Italy, Rome, September 2019.

- J. Köpfler, T. Frenzel, J. Schmalian, and M. Wegener, "High Quality-Factor Topological Ultrasound Resonances in a Microstructured SiO_2-Based 1D Diatomic Chain of 3D Chiral Mechanical Metamaterial Unit Cells", Metamaterials Congress (online), United States of America, New York, September 2021.

ADDITIONAL RELATED WORK HAS ALREADY BEEN PUBLISHED . . .

. . . in scientific journals:

- T. Frenzel, J. Köpfler, E. Jung, M. Kadic, and M. Wegener, "Ultrasound Experiments on Acoustical Activity in Chiral Mechanical Metamaterials", *Nat. Commun.* **10**, 1-6 (2019).

- J. Feis, D. Beutel, J. Köpfler, X. Garcia-Santiago, C. Rockstuhl, M. Wegener, and I. Fernandez-Corbaton, "Helicity-Preserving Optical Cavity Modes for Enhanced Sensing of Chiral Molecules", *Phys. Rev. Lett.* **124**, 033201 (2020).

. . . at scientific conferences (only own presentations):

- J. Feis, D. Beutel, J. Köpfler, X. Garcia-Santiago, C. Rockstuhl, M. Wegener, "Achiral and Helicity Preserving Cavity for Enhanced Infrared Sensing of Chiral Molecules", Metamaterials Congress, Italy, Rome, September 2019.

- T. Frenzel, J. Köpfler, A. Naber, and M. Wegener "Metrology with Atomic-Scale Localization Errors by Optical-Image Cross-Correlation Analysis", SPIE Metamaterials, Metadevices, and Metasystems (online), United States of America, San Diego, August 2020.

1

INTRODUCTION

"It is often very simple ideas which are the deepest" [1]. This statement was made by J. Michael Kosterlitz when honoring his colleague David J. Thouless in his Nobel lecture in December 2016. Together with F. Duncan M. Haldane, they had just received the Nobel prize for their *"theoretical discoveries of topological phase transitions and topological phases of matter"* [1]. Among other achievements, Thouless had described the quantum Hall effect [2] in terms of topology [3]. Thereby, he launched the new material class of topological insulators [4].

In contrast to conventional insulators, topological insulators are governed by an inherent link between their bulk and boundary properties. On the one hand, they are insulating and lack eigenstates within the energy gap of their bulk. On the other hand, they have robust states available at their boundaries. In the quantum Hall effect, these robust boundary states manifest themselves as one-dimensional unidirectional channels with an exactly quantized conductance. Triggered by such an exceptional property, topological insulators turned into a hot topic with plenty of theoretical and experimental research on quantum-mechanical systems [4, 5] as well as on classical wave systems, such as topologically robust photonic and phononic waveguides [6–8]. Thereby, a remarkable effort is put into the complicated design of a system's bulk to achieve control over its boundary. But does it have to be complicated to get topological? As Kosterlitz pointed out in his statement, also simple physical systems can have deep implications.

In its very essence, this thesis deals with nothing more than masses and springs of alternating stiffness lined up in a chain. Most physicists would agree that such a one-dimensional mass-spring model is a indeed rather simple system. The model appears in almost every introductory lecture on solid-state physics and nicely illustrates the emergence of a band gap in the bulk of a periodic system. However, the discussion gets a bit more involved as soon as we remind ourselves that every real-world bulk has to come with some boundary. It turns out that the finite version of this mass-spring model exhibits protected boundary modes similar to the quantum Hall system in two dimensions. In fact, the system is

the mechanical analog of a one-dimensional electronic topological insulator, the so-called Su-Schrieffer-Heeger model [9]. Hence, in the spirit of Kosterlitz, the investigation of a simple finite mass-spring model can be cutting-edge research in its best sense.

As for mass-spring models in a lecture, the focus of metamaterial research is commonly on bulk properties as well. A metamaterial is a rationally designed structure with effective properties that go beyond those of its ingredient materials [10]. These effective properties are naturally related to the metamaterial's bulk, not to its boundary. For instance, mechanical metamaterials were designed to be ultralight and ultrastiff [11], to manipulate acoustic wave propagation [12], or to realize unusual dispersion relations in elastic media [13, 14]. Furthermore, three-dimensional chiral mechanical metamaterials were introduced that escape the description by standard continuum mechanics [15]. Such chiral metamaterials twist upon a push and are capable of rotating the polarization direction of transverse elastic waves [16].

Altogether, mechanical metamaterials and mechanical topological insulators are two complementary building blocks required to gain full control of the propagation of acoustic or elastic waves. What both concepts have in common is that they seek to offer much more than the mere material platform they are realized on. Still, their exceptional properties, may it be within the bulk or at the boundaries, cannot be untied from a mostly undesired real-world material effect: Both metamaterial mechanisms and topologically protected boundary modes of classical wave systems suffer from dissipation. Thereby, their highly praised potential gets easily lost when working toward an actual application. For systems based on three-dimensional laser-printed polymeric microstructures, viscous material damping can be such a show-stopper [17].

In this thesis, I will combine the bulk control provided by a chiral mechanical metamaterial with the boundary control of a topological insulator, starting from the simple mass-spring model described above. I will design, realize, and characterize a metamaterial that exhibits a topologically protected boundary mode. Via such a mode, a small axial push can be resonantly converted to a large rotational motion. In a proof-of-principle design, the chiral topological metamaterial will serve to realize a resonant mechanical laser-beam scanner. To overcome limitations due to dissipation in viscoelastic materials, I will introduce a novel approach that allows for the fabrication of three-dimensional microstructures out of fused-silica glass.

Outline of this thesis

Chapter 2 will capture the required theoretical background on the field of topological mechanics. After a brief introduction on topology in general, I will present the key concepts of topological band theory, emerging as an extension of the well-known band theory in solid-state physics. Shifting the focus from electronic wave functions to classical systems, I will then discuss the mechanical analog of the Su-Schrieffer-Heeger model, which is a prototype model of a topological insulator as well as the starting point of the investigations in this work. I will close the chapter and prepare for the next one by proceeding from mass-spring models to continuum mechanics and its basic principles and equations.

In **chapter** 3, I will describe the route to design a chiral topological mechanical metamaterial that exhibits protected edge modes. Starting from a definition and examples for metamaterials in general, I will show how chirality in mechanics, in combination with the Su-Schrieffer-Heeger model, leads to a coupled model with its own particular topological features. I will describe and explain these features in detail, especially the emergence of the aimed-at topological edge modes, and transfer the configured mass-spring model to a three-dimensional (3D) metamaterial design.

In **chapter** 4, I will show how 3D microstructures, in particular the designed chiral topological metamaterial, can be fabricated out of fused-silica glass by using a glass nanocomposite, two-photon 3D laser printing, and helium-assisted microcasting. The latter is a novel fabrication technique that is introduced in the context of this work. The capabilities and limits of this technique will be discussed to close the chapter.

In **chapter** 5, I will show how the fabricated 3D microstructures can be characterized via measurements at ultrasound frequencies and subsequent optical-image cross-correlation. The resonances of micro tuning forks made of polymer and fused-silica glass will be measured to reveal the materials' stiffness and the relevant damping mechanisms. As the main findings of this chapter, I will then present and discuss the experiments that verify the existence of the aimed-at topological edge resonance of the realized chiral mechanical metamaterial.

In a brief excurse in **chapter** 6, I will show both the design and experiments on a 3D microstructure which is refined toward a potential application as a functional resonant mechanical laser-beam scanner.

Finally, I will summarize the key results of this work in **chapter** 7 and give a brief outlook.

2 Chapter 2
Topology and Mechanics

In this chapter, I will provide the theoretical foundation for this thesis. In the first section, I will shortly introduce the basic concepts and the terminology of topology via two descriptive and intuitive examples. The concepts will then be applied to the standard band theory of solid state physics to explain the celebrated bulk-boundary correspondence of topological insulators and its remarkable implications on the existence of so-called topologically protected boundary modes. Subsequently, I will focus on a one-dimensional (1D) topological mechanical system, i.e., the mass-spring-model analog of the electronic Su-Schrieffer-Heeger model, and discuss its topology in detail. This model is the starting point for the topological metamaterial design as will be presented in chapter 3. Also, I will briefly discuss the effects of dissipation on mass-spring systems and topological systems in general. In the last section, I will make the step from discrete mass-spring models to continuum mechanics and summarize the basic equations required to describe the dynamical behavior of elastic structures, including viscoelastic effects. As outlook toward the next chapter, I will discuss the band structure of an exemplary 1D periodic elastic structure.

2.1 An Introduction to Topology

At the latest in elementary school, children get into contact with the concepts of geometry and sooner or later learn how to calculate lengths and angles of simple objects. In an abstract sense, geometry provides a *quantitative* description of geometrical objects, or generally mathematical spaces, by introducing metrics [18]. The importance of geometry for natural sciences, technology, and industry is self-understood, and a remarkable amount of geometrical principles have already been stated more than two thousand years ago.

In strong contrast, the field of topology emerged only a few centuries ago. As it seeks to describe and classify objects only in terms of their *qualitative* properties, its application, e.g., in physics, remained elusive for a long time [19]. However, in the framework of topology, problems can be solved that are not captured by

(a) (b) (c)

$\chi=2$ $\chi=2$ $\chi=0$
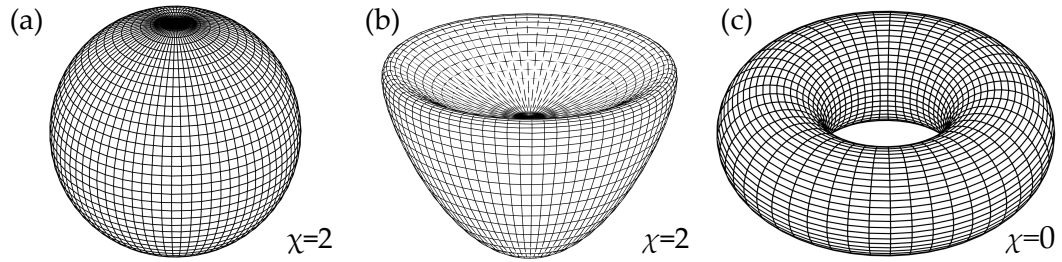
Figure 2.1: Different objects and their Euler characteristic χ. While the sphere (a) and the bowl (b) are geometrically different, they have the same Euler characteristic and are said to be in the same topological phase. (c) The torus with its hole has a different Euler characteristic and is hence said to be in a distinct topological phase.

geometrical considerations. One of the earliest examples is the problem of the bridges of Königsberg [20]. Thereby, the question was if all parts of Königsberg can be visited by crossing each of the seven bridges exactly once. In 1736, Leonard Euler analyzed the problem and showed that this is indeed not possible [21]. Clearly, the proof did not depend on any specific length or angle of the bridges but only on the qualitative structure of the problem. A similar but more recent example is the inscribed rectangle problem. There, it can be proven by a topological argumentation that, for an arbitrary closed contour in a plane, it is always possible to find a rectangle having all its four corners lying on this contour [22]. Notably, a corresponding proof for an inscribed square remains elusive up to date [23]. While these two specific problems seem to be quite peculiar, topology finally found its way into the field of physics in the 1960s, triggered for instance by the Aharonov-Bohm effect [19, 24]. To understand the implications of topology on solid-state physics and in particular on band theory, we start with two simple examples that are introduced along the lines of reference [6] and [25], and along my master's thesis [26].

Euler Characteristic and Genus of Objects

Generally, topology classifies objects or spaces qualitatively by properties that are invariant under continuous deformations [6, 27]. The probably most illustrative example for such an invariant property is the Euler characteristic, which is basically given by the number of holes, also called genus, of a given geometrical object. Figure 2.1 shows three objects: a sphere, a bowl, and a torus. While all three objects have a clearly different geometry, two of them share the same number of holes, i.e., zero. In terms of topology, the sphere and the bowl are said to be in the same *topological phase*, as they are classified by the same *topological invariant* or *topological index*, whereas the torus with its hole in the middle is in a distinct

topological phase. Only by tearing apart the surface of an object and reclosing it differently, and thus by a non-continuous transformation, the number of holes can be changed. Such a change is then called a *topological phase transition*.

From this simple example, two key concepts of topology become apparent: First, the number of holes is always an integer quantity, such that the associated topological invariant can only assume discrete values. This allows for a unique classification and distinction of geometrical objects. Second, a topological invariant is a global property. The number of holes does not depend on the exact geometry of an object and it is not sensitive to local continuous deformations. Still, the global topological properties have to somehow emerge from the local properties. For the genus of geometrical objects, this is captured by the Gauss-Bonnet theorem. It states, that the Euler characteristic χ, linked to the genus g, is obtained by integration of the local curvature K over the closed surface S of the geometrical object [28]:

$$\chi = 2 - 2g = \frac{1}{2\pi} \int_S K \mathrm{d}S. \tag{2.1}$$

Here, the integration appears as the obvious operation to link local to global properties. This will as well hold true for the calculation of topological indices in the context of the topological band theory in section 2.2.

Möbius Strip

A second prominent example for distinct topological phases are the cylinder strip and the Möbius strip, shown in Figure 2.2. Both objects can be described as a fiber bundle E that associates a fiber $F = [-1, 1]$ to each point of a base space which is the unit circle $B = S^1$ [25]. Sitting at some arbitrary position and just describing each strip locally, both fiber bundles can be expressed as the direct product of the base and fiber space, i.e., $E = B \times F$. For the Möbius strip, however, this description breaks down globally. After undergoing a complete roundtrip over the base space, one realizes that the strip is wound up, such that the fiber has to do a transition from $F = [-1, 1] \rightarrow [1, -1]$. As a consequence, the Möbius strip has just one edge and a single, non-orientable surface. Its vector bundle is called *topologically nontrivial*, as the strip globally winds by an angle of π. It has a nonzero *winding number* as topological index. In contrast, the vector bundle of the cylinder is called *topologically trivial*, as its global behavior shows nothing exceptional as compared to the local behavior. Its winding number is zero. Notably, despite differing in their winding numbers, the surface of the cylinder strip and Möbius strip have the same Euler characteristic, i.e., $\chi = 0$. Hence, to properly evaluate and distinguish topological properties, it is crucial to find the topological invariant that is meaningful in a given case.

Figure 2.2: Topologically trivial and nontrivial bundles. (a) The fiber bundle of a cylinder strip can be globally represented by the direct product $E = B \times F$ of a periodic base space B and some fiber F that is assigned to each point of the base. (b) For the Möbius strip this representation works only locally. Due to the nonzero winding, it fails when going once around the strip. Hence, the Möbius bundle is said to be topologically nontrivial. Adapted from [26].

trivial bundle E

periodic base B

nontrivial bundle E
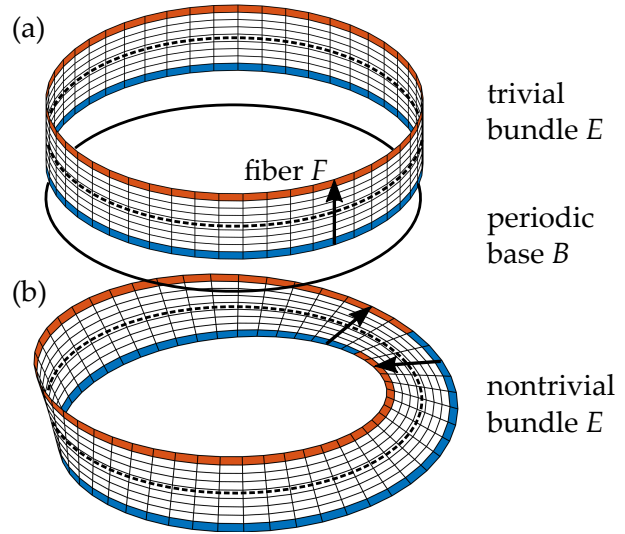
The example of the cylinder and Möbius strip indicates the role of periodicity for topological considerations: Only the periodicity of the unit circle S^1 together with the requirement of having a continuous strip quantizes the possible winding angles to integer multiples of π. Thereby, it creates the distinct topological phases with their associated discrete topological indices. Taking for instance some non-periodic interval $B = [0, 1]$ as a base space, the resulting open strips could have any winding angle and a topological distinction between these objects would be impossible. We will see in the following, that also the topological classification in band theory depends on periodicity, namely on that of the reciprocal space.

2.2 TOPOLOGICAL BAND THEORY

In general, band theory is the conceptual framework to describe the physical properties of spatially periodic media. Originally, band theory was introduced to explain the electronic properties of crystalline solids, such as insulators, metals, and especially semiconductors, by solving the quantum-mechanical Schrödinger equation for electrons in a periodic potential. For quite some time, the focus was on understanding and manipulating the band structure, i.e., the energy spectrum of the solids' bulk, which consists of energy bands and band gaps.

This situation started to change with the discovery of the integer quantum Hall effect (IQHE) for a 2D electron gas in a static magnetic field by Klitzing *et al.* in 1980 and its interpretation in terms of topology [2, 3, 29, 30]. It turned out that the number of unidirectional 1D conduction channels along the boundary of an otherwise insulating 2D electron gas is equal to a topological invariant of its bulk [31]. This equality is now known as the bulk-boundary correspondence. It

implies that the surface properties are somehow encoded in the bulk properties of a solid. However, to see this encoding, the focus has to be shifted away from the energy eigenvalues of the band structure toward the eigenstates associated to these eigenvalues [29, 30, 32].

In the following, the basics of topological band theory are established along the lines of several publications [4, 27, 33, 34]. However, while most discussions are based on 2D systems with the IQHE as a natural example, I will limit the formal description to the equations relevant for 1D periodic systems and otherwise stick to qualitative explanations.

2.2.1 Band Theory

Although we will later discuss phononic band structures of elastic media, we start in the historic context with the eigenstate $|\psi\rangle$ and eigenenergy E of an electron obeying the time-independent Schrödinger equation with a given Hamiltonian $\hat{\mathcal{H}}$:

$$\hat{\mathcal{H}} |\psi\rangle = E |\psi\rangle. \tag{2.2}$$

For a crystalline solid with its periodic potential, the eigenproblem is subject to a discrete spatial translation invariance given by a Bravais lattice. In d dimensions, the Bravais lattice $\mathbf{R}$ and the associated reciprocal lattice $\mathbf{G}$ are constructed via the real-space and the reciprocal lattice vectors $\mathbf{a}_i$ and $\mathbf{b}_i$, respectively:

$$\mathbf{R} = \sum_{i=1}^{d} z_i \mathbf{a}_i \quad \text{and} \quad \mathbf{G} = \sum_{i=1}^{d} m_i \mathbf{b}_i, \quad \text{with} \quad z_i, m_i \in \mathbb{Z} \quad \text{and} \quad \mathbf{a}_i \mathbf{b}_i = 2\pi \delta_{ij}. \tag{2.3}$$

According to Bloch's theorem, the electronic eigenstates can be written as a state $|u_n(\mathbf{k})\rangle$ periodic in the lattice $\mathbf{R}$, modulated by a spatial phase factor:

$$|\psi_n(\mathbf{k})\rangle = \mathrm{e}^{\mathbf{ikr}} |u_n(\mathbf{k})\rangle. \tag{2.4}$$

Here, n is the band index. The wave vector or quasimomentum $\mathbf{k}$ is defined inside of the first Brillouin zone of the reciprocal lattice and the eigenstates are subject to the periodicity

$$|\psi_n(\mathbf{k})\rangle = |\psi_n(\mathbf{k} + \mathbf{G})\rangle. \tag{2.5}$$

Using the Bloch ansatz on equation 2.2, we get the eigenequation

$$\hat{H}(\mathbf{k}) |u_n(\mathbf{k})\rangle = E_n(\mathbf{k}) |u_n(\mathbf{k})\rangle, \tag{2.6}$$

with the wave-vector-dependent Hamiltonian $\hat{H}(\mathbf{k})$. Following the periodicity of the eigenstates, the associated eigenenergies are also periodic, leading to the

formation of energy bands. As a consequence, all the information about the eigenstates $|u_n(\mathbf{k})\rangle$ and eigenenergies $E_n(\mathbf{k})$ is captured in the band structure within the first Brillouin zone. We know that $|u_n(\mathbf{k})\rangle$ and $|u_n(\mathbf{k} + \mathbf{G})\rangle$ are equivalent states, up to a phase factor that follows from equations 2.4 and 2.5 [34]:

$$|u(\mathbf{k} + \mathbf{G})\rangle = \mathrm{e}^{-\mathrm{i}\mathbf{G}\mathbf{r}} |u(\mathbf{k})\rangle . \tag{2.7}$$

2.2.2 Berry Phase

Comparable to the Möbius strip in the previous section, the band structure can mathematically be understood as a fiber or vector bundle, as shown in Figure 2.3(a). The periodic base space of this bundle is the first Brillouin zone, which is linked to the space of states $|u_n(\mathbf{k})\rangle$ via the Hamiltonian $\hat{H}(\mathbf{k})$ [25]. To check, whether such a vector bundle is wound up, one has to go once around the base space and evaluate the change of the eigenstates, or more precisely, the change in their phase.

For two eigenstates $|u_n(\mathbf{k})\rangle$ and $|u_n(\mathbf{k} + \mathrm{d}\mathbf{k})\rangle$ that are neighboring in the base space and separated by $\mathrm{d}\mathbf{k}$, the phase difference $\mathrm{d}\gamma$ is given by

$$\mathrm{e}^{-\mathrm{i}\mathrm{d}\gamma} = \frac{\langle u_n(\mathbf{k})|u_n(\mathbf{k} + \mathrm{d}\mathbf{k})\rangle}{|\langle u_n(\mathbf{k})|u_n(\mathbf{k} + \mathrm{d}\mathbf{k})\rangle|}. \tag{2.8}$$

Taking the first order approximation in $\mathrm{d}k$ on both sides yields

$$\mathrm{d}\gamma = \mathrm{i} \langle u_n(\mathbf{k})|\nabla_\mathbf{k}|u_n(\mathbf{k})\rangle \, \mathrm{d}\mathbf{k}. \tag{2.9}$$

Here, the eigenstates are assumed to be normalized. Reformulating the equation, we obtain the local phase change of the eigenstates in the reciprocal space, called the *Berry connection* [35]:

$$\mathbf{A}_n(\mathbf{k}) = \frac{\mathrm{d}\gamma}{\mathrm{d}\mathbf{k}} = \mathrm{i} \langle u_n(\mathbf{k})|\nabla_\mathbf{k}|u_n(\mathbf{k})\rangle = -\operatorname{Im} \langle u_n(\mathbf{k})|\nabla_\mathbf{k}|u_n(\mathbf{k})\rangle . \tag{2.10}$$

Notably, the phase of the individual eigenstates $|u_n(\mathbf{k})\rangle$ can be chosen arbitrarily without affecting the physics behind [27]:

$$|u_n(\mathbf{k})\rangle \rightarrow \mathrm{e}^{\mathrm{i}\alpha(\mathbf{k})} |u_n(\mathbf{k})\rangle . \tag{2.11}$$

Of course, such a transformation also changes the phase difference between the eigenstates, meaning that the Berry connection is not gauge-invariant with respect to this phase ambiguity and hence has no direct physical meaning. Only by integrating the Berry connection over a closed contractible loop in reciprocal space, one obtains an observable physical quantity, the *Berry phase*

$$\gamma_n^\mathrm{B} = \oint_\mathcal{C} \mathbf{A}_n(\mathbf{k})\mathrm{d}\mathbf{k}. \tag{2.12}$$
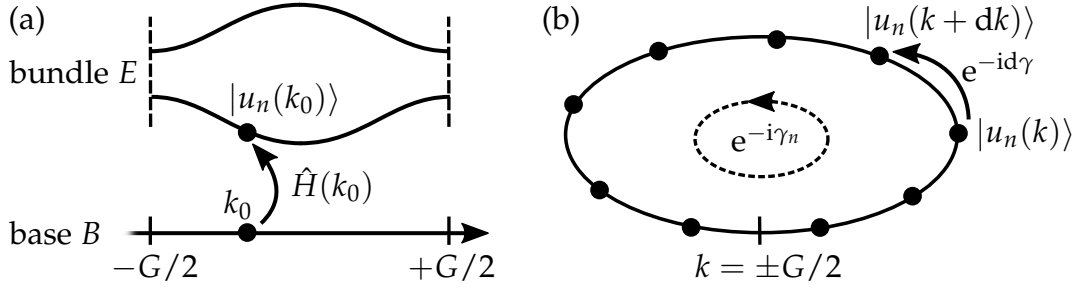
Figure 2.3: (a) Exemplary band structure of a 1D lattice. The Bloch Hamiltonian $\hat{H}(k_0)$ assigns the eigenstates $|u_n(k_0)\rangle$ of individual bands n to each wave number k_0. The resulting bundle has the 1D first Brillouin zone as its periodic base space. (b) The winding of such a bundle is measured via the Berry phase accumulated across the 1D Brillouin zone, i.e., the Zak phase γ_n. For a discretized version of the reciprocal space, the Zak phase can be calculated by summing up the phases $d\gamma$ between neighboring Bloch eigenstates. Adapted from [26].

As it appears in a phase factor, the Berry phase is only defined up to an integer multiple of 2π. By moving on a closed loop from eigenstate to eigenstate in the reciprocal space, each of their arbitrary phases will appear once in bra- and once in ket-notation in the scalar product in equation 2.8. Thus, in total, the phases cancel out and make the Berry phase a gauge-independent quantity [35]. As Berry himself stated in his paper [32], the Berry phase is generally a geometrical phase that is acquired by adiabatically driving a quantum-mechanical system through some parameter space. However, it is not merely a concept for electronic Bloch eigenstates in the reciprocal space but can be equally applied to other quantum-mechanical systems, and even to classical systems. Examples are the Aharanov-Bohm phase for electrons propagating around a confined magnetic flux, the polarization rotation of light in a twisted fiber, and the rotation of Foucault's pendulum [36].

2.2.3 Zak Phase

From Berry's geometrical phase it is only a small step to the actual topological invariant of a band structure. For this, it is necessary to not only consider the phase change of the Bloch eigenstates over some closed loop in the reciprocal space but rather over the complete periodic base space, i.e., the complete first Brillouin zone.

The apparently simplest case is a 1D crystal with lattice constant a and the corresponding wave number k lying in first Brillouin zone $k \in [-\pi/a, +\pi/a]$. Given the periodic boundaries of the wave number, the Brillouin zone can be represented by a circle, and the closed loop around it automatically covers the

whole reciprocal space, as shown in Figure 2.3(b). Using equations 2.10 and 2.12 for the Berry connection and Berry phase, we get the so-called *Zak phase* [37]

$$\gamma_n = -\operatorname{Im} \int_{-\pi/a}^{\pi/a} \langle u_n(k) | \partial_k u_n(k) \rangle \, \mathrm{d}k, \tag{2.13}$$

$$= -\operatorname{Im} \sum_{k_i=-\pi/a}^{\pi/a-\mathrm{d}k} \ln \langle u_n(k_i) | u_n(k_i + \mathrm{d}k) \rangle. \tag{2.14}$$

The second equation is just the integral for k-values discretized into steps of $\mathrm{d}k$ and follows directly from equation 2.8. It will be useful to perform numerical calculations. As the Berry phase, the Zak phase is only defined up to an integer multiple of 2π. We will see that the Zak phase is quantized given the proper symmetries of the Hermitian operator in the eigenequation 2.6 and can only assume the value 0 for a topologically trivial band or π for a topologically nontrivial band. Thus, it is called a $\mathcal{Z}_2$ topological invariant and it is the quantity that will be evaluated for the 1D band structures discussed in this work. In analogy to the Möbius strip, the acquisition of a nonzero Zak phase is often described as a winding or twisting of an individual band. The winding of the Bloch states will be visualized when discussing the Su-Schrieffer-Heeger model in section 2.3. There, we will also see that the Zak phase is not invariant under a change of the unit cell convention of the 1D crystal lattice. This makes it a quite peculiar topological invariant as compared to invariants in higher dimensions, such as the Chern number for the IQHE in 2D, which is shortly introduced in appendix A.1.

2.2.4 *Bulk-Boundary Correspondence and Topological Insulators*

The emergence of the bulk-boundary correspondence will be shown in detail for the 1D Su-Schrieffer-Heeger model in section 2.3. In the following, I will only provide a qualitative general explanation, as a conclusive formal explanation involves a larger set of equations and is beyond the scope of this work. For explanations based on the 2D IQHE, I would like to refer to reference [33] or [35].

As introduced in the formalism for the Berry and Zak phase, i.e., in equation 2.13, topological invariants are generally assigned to individual isolated bands of a given band structure. However, Berry deduced that a nontrivial band with nonzero topological invariant is actually a result of virtual interactions with the eigenstates of other bands [32]. By these virtual interactions, the eigenstates of the bands can mutually wind up themselves, such that each of the bands obtains the opposite winding direction and a topological invariant with opposite sign. As a consequence of this exchange of winding, the complete vector bundle of all
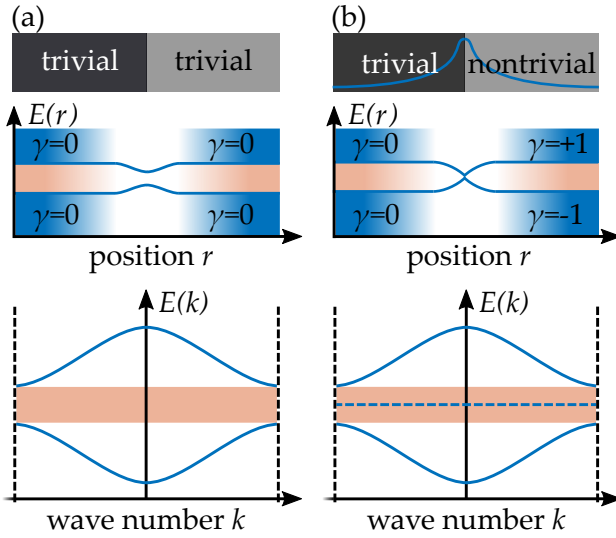
Figure 2.4: Bulk-boundary correspondence for a 1D topological insulator. (a) At the spatial interface of two trivial insulators with equal topological indices γ, a topological phase transition is not required. The band gap (red region) stays open. (b) For a trivial-nontrivial interface with unequal γ, the band gap has to close such that the bands can undergo a topological phase transition. This generates a boundary state localized to the interface. The energy E of the boundary state (blue dashed line) lies inside of the band gap of the bulk's energy spectrum.

bands of a system has always a total winding of zero and thus stays trivial [19]. Only subsets of bands can be nontrivial. Since the topological invariants of individual bands are quantized, they cannot be changed by smooth deformations of the band structure. As for the Euler characteristic, a non-continuous transformation is required to change the invariants and the topological phase. For the energy bands, this topological phase transition can only happen if two originally isolated bands touch each other, thus become degenerate and change their winding [35].

This becomes relevant, when not only considering infinitely extended crystal lattices but also boundary effects occurring in finite systems: Assume two insulating systems that have a band gap in the same region of the energy spectrum but distinct topological indices of the bands above and below the band gap, as shown in Figure 2.4. The bulk-boundary correspondence then states that boundary states have to exist at the spatial interface between the two systems, and the number of boundary states corresponds to the difference in the topological invariants [31]. If both systems are in the same topological phase, e.g., the trivial phase with an invariant of zero, there is no need for a topological phase transition across the interface, such that the band gap will stay open. However, if the invariants differ, the bands have to touch. This generates one or more boundary states which have their energy inside of the band gap and hence have to be spatially confined to the interface region. The result is a *topological insulator* that is insulating in the bulk due to its band gap but has states available at the boundary. In the simplest case, the boundary around the bulk of a topological insulator is just the vacuum around it, which is basically just a trivial insulator [34]. In such a case, the band gap of a topological insulator is often simply referred to as a *topological band gap*, omitting the specification *nontrivial* in the naming.

The boundary states are the cause for the great interest in topological insulators, as can be seen already from the IQHE. For a 2D bulk, these states are 1D edge channels that are guaranteed to exist and robust against perturbation and defects. Thereby, the robustness holds true as long as the symmetries inducing the non-triviality of the bulk bands are also present at the boundary. For the IQHE, it is the rather the absence of a symmetry, namely broken time-reversal symmetry due to an applied magnetic field, that generates the nontrivial band gap. It renders the edge states not only guaranteed but also unidirectional and thereby immune to back-scattering [4]. These features together made 2D topological insulators extremely popular as platform to design 1D conduction channels and 1D waveguides for classical systems [6, 8]. For 1D bulk systems, the interest lies in the existence of zero-dimensional (0D) edge states that are spatially localized and spectrally isolated from the bulk modes, as we will see in the course of this thesis.

2.2.5 Topology and Symmetry

As already indicated, the topological properties of bulk bands are imposed by the symmetries that are present or absent. Triggered by the proposal of the quantum spin Hall effect in 2005 [38–41], it became clear that time-reversal breaking is not the only way to realize topological insulators. The quantum spin Hall insulator obeys time-reversal symmetry and has separate edge states for spin-up and spin-down states with propagation in opposite directions. As the Euler characteristic did not describe the Möbius strip properly, the Chern number of the IQHE turned out to be a meaningless topological invariant for quantum spin Hall systems. Hence, other topological invariants for other topological phases had to be identified. By systematically classifying all 10 possible symmetry classes for generic Hamiltonians, a variety of 15 different topological classes for 1D, 2D, and 3D systems were identified [5]. Following Altland and Zirnbauer [42], every electronic Hamiltonian can be classified by time-reversal symmetry, charge-conjugation symmetry, and chiral symmetry. The three symmetries determine how Bloch eigenstates can evolve when varying the wave vector $\mathbf{k}$ within the first Brillouin zone and thus also what results can be obtained for the topological invariants, e.g., for the Zak phase in equation 2.13.

Time-reversal symmetry is present, if the Bloch Hamiltonian $\hat{H}(\mathbf{k})$ fulfills

$$\hat{T}\hat{H}^T(\mathbf{k})\hat{T}^{-1} = \hat{H}(-\mathbf{k}) \qquad \text{with} \qquad \hat{T}^2 = \pm 1, \tag{2.15}$$

where $\hat{T}$ is a unitary operator mapping the Bloch eigenstates from $\mathbf{k}$ to $-\mathbf{k}$. The case $\hat{T}^2 = +1$ corresponds to bosonic time-reversal symmetry. Charge-conjugation symmetry also links wave vectors with opposite sign, with an additional sign

inversion of the Bloch Hamiltonian:

$$\hat{C}\hat{H}^T(\mathbf{k})\hat{C}^{-1} = -\hat{H}(-\mathbf{k}) \qquad \text{with} \qquad \hat{C}^2 = \pm 1. \qquad (2.16)$$

Again, $\hat{C}$ has to be some unitary operator. The third symmetry, called chiral symmetry, is just the combination of the first two, resulting in

$$\hat{S}\hat{H}(\mathbf{k})\hat{S}^{-1} = -\hat{H}(\mathbf{k}) \qquad \text{with} \qquad \hat{S}^2 = 1, \qquad (2.17)$$

for a unitary $\hat{S}$. The names of the three symmetries refer to their meaning when acting on electronic Hamiltonians. In classical wave systems, these symmetries should be rather seen as purely formal constraints on the Hermitian operator of a given eigenproblem [7].

Strong Topological Insulators and Topological Crystalline Insulators

As the above classification applies to any generic Hamiltonian, no assumptions were made about additional discrete spatial symmetries that might be present in a given crystal. The three symmetries are thus called nonspatial or global symmetries and are preserved at boundaries of a system independent of the exact spatial termination [34]. This guarantees that the bulk-boundary correspondence is valid even in the presence of lattice disorder. As a consequence, the topological classes that only rely on these nonspatial symmetries are labeled as strong topological insulators.

When taking spatial symmetries into account, such as inversion [43], rotation, and reflection, the Bloch Hamiltonian and Bloch eigenstates can be subject to additional restrictions, e.g.,

$$\hat{P}\hat{H}(\mathbf{k})\hat{P}^{-1} = \hat{H}(-\mathbf{k}) \qquad \text{with} \qquad \hat{P}^2 = \pm 1, \qquad (2.18)$$

with a unitary or antiunitary parity operator $\hat{P}$ which is distinct from the ones in equations 2.15 to 2.17. By this, the topological classification gets even more detailed and it is expected that an own classification scheme has to be established for each discrete space-group symmetry [44, 45]. If the nontriviality of a topological insulator and thus the existence of topologically protected boundary states depends on such spatial symmetries, the system is called a topological crystalline insulator. We will see in section 2.3 that the quantization of the Zak phase for the Su-Schrieffer-Heeger model depends both on a nonspatial and a spatial symmetry.

2.2.6 *From Electronics to Mechanics*

Given the historic context, the topological band theory introduced so far was only based on electronic states obeying the Schrödinger equation. Yet, after the concepts of band theory were transferred to classical wave systems, such as photonic crystals [46–48] and phononic crystals [12, 49, 50], the design of topological classical systems began as well. The starting points were the theoretical description of the analog of the quantum Hall effect in photonic crystals [51, 52] and topological phonon modes in self-assembled hollow protein tubes [53]. Such systems are also described in terms of an eigenequation similar to equation 2.6 with a Hermitian eigenoperator and eigenvalues dependent on a periodic wave vector. By mapping the classical equations of motion to a differential equation in the form of the Schrödinger equation, the topological classification established for electronic systems can be adopted for classical systems [7]. In fact, it was proposed that each of the 15 strong topological classes can be mimicked by adequately coupling classical passive elements [54]. In this way, classical systems can serve as interesting toy models for topological classes that are not easy to experimentally realize as electronic topological insulators. Taking also platforms that rely on spatial symmetries into account, plenty of classical topological systems have been proposed and demonstrated [6, 8].

In acoustic and elastic systems, analogs of the quantum Hall insulator with its unidirectional edge states [55–58] were established as well as analogs of the quantum spin Hall insulator [59–63]. Also 3D systems exhibiting topological features such as Weyl degeneracies [64, 65] and higher-order topological insulators with boundary states that can be confined to more than one dimension less as compared to the bulk system were investigated [66]. Topological states were also discussed in terms of isostatic mechanical lattices [67]. Acoustic and elastic topological systems in 1D are mostly realizations of the Su-Schrieffer-Heeger model [8]. This model is discussed in the following section and will be the starting point for the design of a more complex topological system as will be presented in chapter 3.

2.3 THE MECHANICAL SU-SCHRIEFFER-HEEGER MODEL

The Su-Schrieffer-Heeger (SSH) model was initially established to describe the electronic properties of the polymer *trans*-polyacetylene [9]. As shown in Figure 2.5(a), *trans*-polyacetylene is a linear chain of sp^2-hybridized carbon atoms. The molecule can be described via a tight-binding approach where each electron is strongly bound to a carbon atom but can hop to the neighboring ones according to hopping parameters. In the dimerized configuration, *trans*-polyacetylene has

(a)

(b)

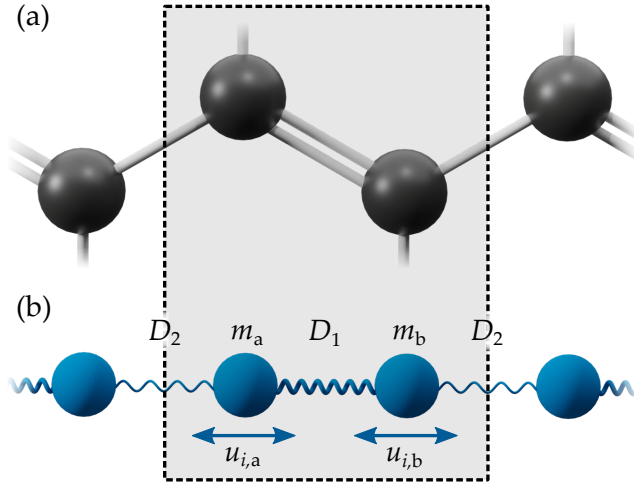D_2 m_a D_1 m_b D_2

$u_{i,a}$ $u_{i,b}$

Figure 2.5: Su-Schrieffer-Heeger model. (a) The linear polymer *trans*-polyacetylene with alternating single and double carbon bonds can be described via a tight-binding model with a diatomic basis. (b) The mechanical analog is a mass-spring chain with equal masses $m_a = m_b = m$ and alternating springs D_1 and D_2 of different stiffness. The dashed gray box shows a possible unit cell convention with the displacements $u_{i,a}$ and $u_{i,b}$ in cell i at the two sublattice sites, a and b, respectively.

alternating double and single carbon bonds, which requires a description using a unit cell with a diatomic basis and two sublattice sites. While the SSH model was discussed in the course of rather exotic properties, i.e., topological solitons and conducting polymers [68], the model configuration itself is very basic and its tight-binding Hamiltonian can be mimicked easily in mechanics by a mass-spring model, as shown in Figure 2.5(b). It requires equal masses that are connected via alternating strong and weak springs, corresponding to the double and single carbon bonds, respectively. In fact, this SSH-like mass-spring model is close to a diatomic model that is very often presented in lectures to show the emergence of phononic band gaps. There, however, usually the masses are alternated instead of the spring constants, which will turn out to be fundamentally different in terms of the band structure's topology.

To see this, we start with a mass-spring model with different masses m_a and m_b at the two sublattice sites a and b, coupled by intracell springs and intercell springs with spring constant D_1 and D_2, respectively. From Newton's second law and Hooke's law we get the equations of motion for the two time-dependent longitudinal displacements $u_{i,a}(t)$ and $u_{i,b}(t)$ in each unit cell i:

$$\begin{aligned}
\frac{\mathrm{d}^2 u_{i,a}}{\mathrm{d}t^2} &= \frac{D_1}{m_a}\left(u_{i,b} - u_{i,a}\right) + \frac{D_2}{m_a}\left(u_{i-1,b} - u_{i,a}\right), \\
\frac{\mathrm{d}^2 u_{i,b}}{\mathrm{d}t^2} &= \frac{D_1}{m_b}\left(u_{i,a} - u_{i,b}\right) + \frac{D_2}{m_b}\left(u_{i+1,a} - u_{i,b}\right).
\end{aligned} \tag{2.19}$$

To solve these equations for all discrete lattice sites, we use a wave ansatz with angular eigenfrequency ω and wave number k, e.g., for sublattice site a,

$$u_{i,a}(t) = u_a(k) \cdot \mathrm{e}^{\mathrm{i}(kR_i - \omega t)}, \tag{2.20}$$

where $R_i = ia$ are the discrete lattice positions and a the corresponding lattice constant. Thereby, we get an eigenequation similar to the Bloch equation 2.6:

$$\hat{D}(k)\mathbf{u}_n(k) = \omega_n^2(k)\mathbf{u}_n(k),$$
$$\text{with} \quad \mathbf{u}_n(k) = (\sqrt{m_a}u_{n,a}(k), \sqrt{m_b}u_{n,b}(k))^T. \tag{2.21}$$

Here, $\mathbf{u}_n(k)$ are the Bloch eigenvectors of the two bands $n = 1, 2$, defined within the first Brillouin zone $k \in [-\pi/a, +\pi/a]$. Note that the Bloch vector components $u_{n,a(b)}(k)$ and real space displacement amplitudes $u_{i,a(b)}(t)$ are used in parallel in this thesis and should not be confused. The phase relation of the displacements at the two sublattice sites is absorbed in the complex components $u_{n,a}(k)$ and $u_{n,b}(k)$. The dynamical matrix $\hat{D}(k)$ is given by

$$\hat{D}(k) = \begin{pmatrix} \frac{D_1+D_2}{m_a} & \frac{-D_1-D_2 e^{-ika}}{\sqrt{m_a m_b}} \\ \frac{-D_1-D_2 e^{ika}}{\sqrt{m_a m_b}} & \frac{D_1+D_2}{m_b} \end{pmatrix}, \tag{2.22}$$

which is Hermitian, i.e., $\hat{D}^\dagger(k) = \hat{D}(k)$. For a moment, we limit ourselves to equal masses $m_a = m_b = m$ and obtain the dispersion relation

$$\omega_{1,2}^2(k) = \frac{D_1 + D_2}{m} \pm \frac{\sqrt{D_1^2 + D_2^2 + 2D_1 D_2 \cos(ka)}}{m}. \tag{2.23}$$

To make the discussion independent of the parameters that merely act as scaling factors, the dispersion relation can be expressed in terms of the normalized (angular) frequencies

$$\tilde{\omega} = 2\pi \frac{a}{\lambda} = \omega \frac{a}{c_l}, \tag{2.24}$$

where λ is the wavelength and $c_l = a\sqrt{(D_1 + D_2)/m}$ the phase velocity of the lower band close to $k = 0$. As shown in Figure 2.6(a), one obtains a 1D band gap in the spectrum of this mechanical analog of the SSH model for the two parameter regimes $D_2 < D_1$ and $D_2 > D_1$, thus for a nonzero normalized difference

$$\Delta = \frac{D_1 - D_2}{D_1 + D_2}. \tag{2.25}$$

For $D_1 = D_2$ and $\Delta = 0$, however, the band gap closes at the Brillouin zone boundary at $k = \pm\pi/a$. Following the ideas of topological band theory, a topological phase transition could come along with this gap closing, rendering the bands topologically nontrivial in one of the two regimes.
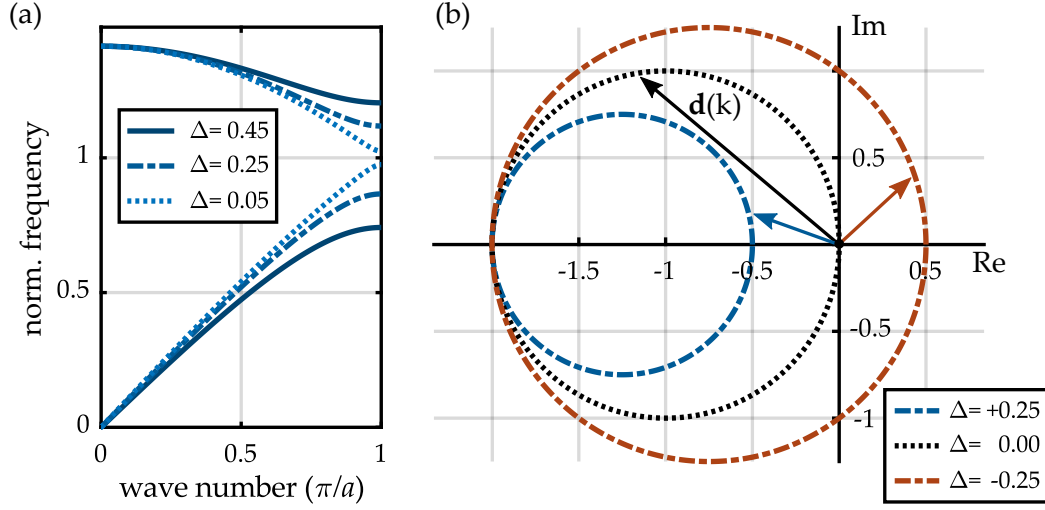
Figure 2.6: (a) Band structure of the mechanical SSH model with two bands separated by a band gap. The band gap reduces when decreasing the normalized spring constant difference Δ. (b) Contours of the vector $\mathbf{d}(k)$ representing the dynamical matrix. For $\Delta > 0$ ($D_2 < D_1$), the vector does not wind around the origin, while for $\Delta < 0$ ($D_2 > D_1$), the nonzero winding indicates a topologically nontrivial phase. The distance between the vector's tip and the origin is proportional to the width of the band gap. For equal spring constants, i.e., $\Delta = 0$, the band gap closes and the winding number and topological phase changes.

To verify that this is indeed the case, I will use two approaches, that are transferred from discussions on the electronic SSH model [34, 35]. In the first approach, I will focus on the dynamical matrix and clarify analytically, how the symmetries introduced in section 2.2.5 lead to distinct topological phases and to the emergence of the bulk-boundary correspondence. The second approach will show how consistent conclusions can be drawn from the eigenvectors' behavior by numerically evaluating the Zak phase as motivated in section 2.2.3.

2.3.1 Symmetry Classification

The dynamical matrix can be classified via its nonspatial and spatial symmetries following equations 2.15 to 2.18. We use the three Pauli matrices σ_x, σ_y, σ_z, and the identity matrix σ_0 (see appendix A.2), which are all unitary 2×2 matrices and involutory, i.e., they are their own inverse. From equation 2.22, it is apparent that $\hat{D}^T(k) = \hat{D}(-k)$ holds true for real-valued spring constants D_1 and D_2, such that the matrix respects the bosonic time-reversal symmetry of equation 2.15:

$$\hat{T}\hat{D}^T(k)\hat{T}^{-1} = \hat{D}(-k) \quad \text{with} \quad \hat{T}^2 = \sigma_0^2 = +1. \tag{2.26}$$

Additionally, the dynamical matrix satisfies the parity symmetry

$$\hat{P}\hat{D}(k)\hat{P}^{-1} = \hat{D}(-k) \quad \text{with} \quad \hat{P}^2 = \sigma_x^2 = +1. \tag{2.27}$$

This symmetry is only present, if the two diagonal elements of $\hat{D}$ are equal, thus only if $m_a = m_b$. In this case an inversion or mirror symmetry is established with respect to the center of the unit cell, as can be verified in Figure 2.5(b). This mirror symmetry can also be described as sublattice symmetry, as σ_x acting on the eigenvector in equation 2.21 interchanges the two sublattice sites a and b:

$$\hat{P}\begin{pmatrix} u_{n,a}(k) \\ u_{n,b}(k) \end{pmatrix} = \begin{pmatrix} u_{n,b}(k) \\ u_{n,a}(k) \end{pmatrix}. \tag{2.28}$$

The two symmetries are required to induce two topologically distinct phases in the SSH system. This becomes obvious when decomposing the dynamical matrix of equation 2.22 into the base of the three Pauli matrices and the identity matrix:

$$\hat{D}(k) = \begin{pmatrix} d_x(k) \\ d_y(k) \\ d_z(k) \end{pmatrix} \cdot \begin{pmatrix} \sigma_x \\ \sigma_y \\ \sigma_z \end{pmatrix} + d_0\sigma_0,$$

$$\text{with} \quad d_0 = \frac{D_1 + D_2}{m}, \tag{2.29}$$

$$d_x = -\frac{D_1 + D_2\cos(ka)}{m},$$

$$d_y = -\frac{D_2\sin(ka)}{m},$$

and $d_z = 0$, as long as we keep the masses m_a and m_b equal and thereby the mirror symmetry intact. The k-dependent dynamical matrix of the SSH model is affected by the mirror symmetry as follows: As long as $d_z = 0$, the matrix can be fully described by the vector

$$\mathbf{d}(k) = d_x(k) + id_y(k) = \frac{-D_1 - D_2e^{ika}}{m}, \tag{2.30}$$

which is confined to the complex plane, as shown in Figure 2.6(b). It describes a circle with radius D_2 around its center point at D_1 on the real axis when sweeping the wave number k once across the first Brillouin zone. The component d_0 can be neglected, as it is merely a k-independent offset equivalent to the first term in the dispersion relation in equation 2.23. The spectral distance between the squared eigenfrequencies of the two bands corresponds directly to the k-dependent modulus of the vector $\mathbf{d}(k)$,

$$\omega_2^2(k) - \omega_1^2(k) = 2|\mathbf{d}(k)| = 2\sqrt{d_x^2(k) + d_y^2(k)}, \tag{2.31}$$

which is the distance of this vector from the origin. For $D_2 < D_1$, the contour of the vector $\mathbf{d}(k)$ does not rotate around the origin, such that, in terms of topology, it can be labeled as topologically trivial phase with a winding number of 0. For $D_2 > D_1$, the contour includes the origin and obtains a winding number of 1, corresponding to the topologically nontrivial phase. Having a spatial interface between the trivial and nontrivial phase, the circular contour of the vector has to sweep and at some point cross the origin to change the winding number, as shown in Figure 2.6(b). Crossing the origin, according to equation 2.31, means closing the band gap at the interface and generating a 0D boundary state. This establishes the bulk-boundary correspondence for the SSH model.

The situation is fundamentally different if one allows for different masses $m_a \neq m_b$, breaking mirror symmetry and thus obtain $d_z \neq 0$. In this case, the contour of the vector $\mathbf{d}(k)$ is not confined to a plane through the origin anymore and can enclose any solid angle in the parameter space, making it impossible to define a quantized winding number. As a consequence, a topological classification becomes elusive and at a spatial boundary the vector's contour does not necessarily have to cross the origin. Hence, it will not generate a boundary state.

When going back to the more common lecture mass-spring model with alternating masses but equal spring constants, another mirror symmetry is reestablished, this time with respect to the mass position (cf. Fig. 2.5(b)). Surprisingly, this symmetry does not restrict the vector $\mathbf{d}$ to the complex plane again an hence it does also not recover the distinct topological phases. This makes the mechanical SSH model and the lecture mass-spring model fundamentally different. While both are able to explain phononic band gaps, only the SSH model provides a quantized winding number and two distinct topological phases, rendering it a 1D mechanical topological insulator.

To conclude this section, it should be noted that the symmetry classification of the SSH model, despite its simplicity, is quite controversial. In addition to bosonic time-reversal symmetry and mirror symmetry, the SSH model also exhibits the formal charge-conjugation symmetry and chiral symmetry (equations 2.16 and 2.17), which puts it into one of the 10 fundamental symmetry classes of strong topological insulators, i.e., the so-called BDI class [7]. This class is characterized by a $\mathcal{Z}$ topological invariant and has more than the two distinct trivial and nontrivial topological phases as described by the $\mathcal{Z}_2$ invariant winding number. However, this does not capture the features of the SSH model correctly, such that a classification as a topological crystalline insulator (or a so-called Dirac-insulator [34]) equipped with time-reversal symmetry and mirror or inversion symmetry is more meaningful.

2.3.2 Zak Phase

The above analysis of the SSH model via a vector describing the associated dynamical matrix illustrates its topological features nicely. However, the approach relies on the fact that the SSH model has only two degrees of freedom (DOF) per unit cell, which made it possible to decompose it into a maximum of three wave-vector-dependent parameters visualized in a 3D coordinate system. The situation will change in chapter 3 when dealing with four DOF per unit cell. There, the dynamical matrix would have to be decomposed into 16 unitary matrices and thus a vector $\mathbf{d}(\mathbf{k})$ as above would move in 16-dimensional space, making the visualization of a quantized winding number elusive. Hence, a numerical evaluation of the winding number based on the eigenvectors and their Zak phase is more advisable.

The Zak phase is calculated numerically using equation 2.14. For the Bloch eigenvectors of equation 2.21, the scalar product measuring the phase between neighboring states boils down to

$$\langle \mathbf{u}_n(k_i) | \mathbf{u}_n(k_i + \mathrm{d}k) \rangle = \sum_{c=1}^{2} u_{n,c}^*(k_i) u_{n,c}(k_i + \mathrm{d}k), \qquad (2.32)$$

with the sum over the two complex eigenvector components corresponding to the two sublattice sites. Figure 2.7(a) shows the accumulation of the Berry connection, i.e., the Zak phase evolution, across the first Brillouin zone for various spring constant differences Δ in the mirror-symmetric SSH model. In agreement with the winding number in previous sections, one obtains a quantized topological index for the two bands, now identified with an accumulated Zak phase of $\gamma_n = 0$ or $\gamma_n = \pi$ for $D_2 < D_1$ or $D_2 > D_1$, respectively. For a configuration with unequal masses $m_\mathrm{a} \neq m_\mathrm{b}$, shown in Figure 2.7(b), the mirror symmetry and the quantization breaks down. Thereby, the accumulated Zak phase can assume arbitrary values and the distinct topological phases vanish.

To obtain the Zak phase accumulation in Figure 2.7, the global arbitrary phase of each numerically calculated Bloch eigenvector entering in equation 2.32 was fixed by forcing one of its components to be real-valued. As explained in section 2.2.2, the individual phase relations of neighboring eigenvectors, i.e., the Berry connection, depend on this phase convention. Thus, it should be noted that the phase evolution across the first Brillouin zone could look quite differently for a different phase convention. The result for the overall accumulated Zak phase, however, would not be affected.
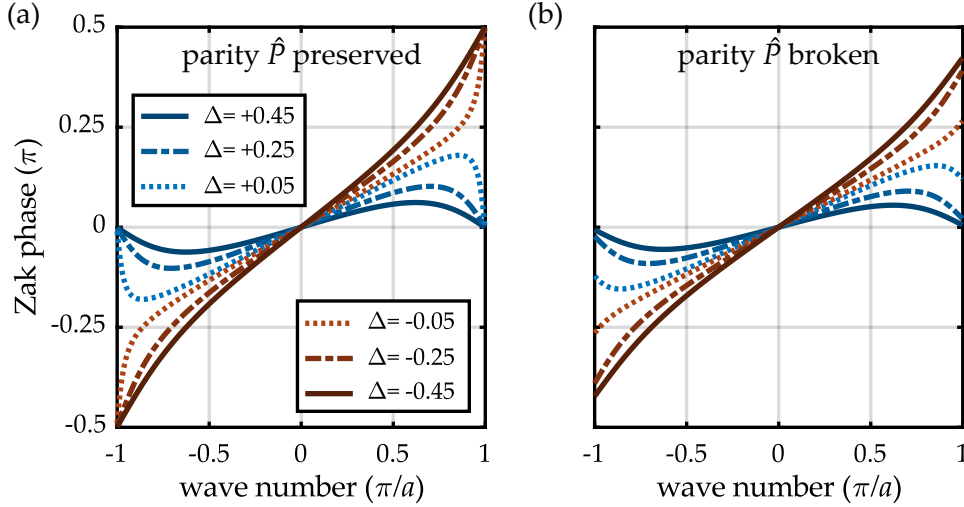
Figure 2.7: Numerically calculated Zak phase evolution of the first band for various spring constant differences Δ. (a) For the SSH model, the Zak phase accumulated across the first Brillouin zone is discretized to values of $\gamma_1 = 0$ or $\gamma_1 = \pi$, corresponding to the trivial or nontrivial phase, respectively. Even close to the phase transition at $\Delta = 0$, the phase snaps to one of these two values. (b) This holds no longer true if the mirror (parity) symmetry is broken. For an exemplary mass difference of $(m_b - m_b)/(m_b + m_b) = 0.2$, the Zak phase can change continuously. Thus, the distinct topological phases vanish and no protected boundary states are expected for this configuration.

2.3.3 Band Inversion

On first sight, the Zak phase calculation is just a black box that takes the Bloch eigenstates as input and gives the topological phase of the associated band as output. However, the eigenvectors are subject to the same symmetry considerations as the dynamical matrix itself, such that the Zak phase quantization should also be apparent for the eigenvectors. From the parity symmetry in equation 2.27, remembering that $\hat{P} = \sigma_x = \sigma_x^{-1} = \hat{P}^{-1}$, it follows that the dynamical matrix $\hat{D}(k)$ commutes with $\hat{P}$ at the high-symmetry points $k = 0$ and $k = \pi/a$, where original and sign-reversed wave numbers are equal up to a reciprocal lattice vector. Hence, $\hat{D}(k)$ and $\hat{P}$ share eigenvectors at these points and it holds

$$\hat{P}\mathbf{u}_n(0) = p_0^{(n)}\mathbf{u}_n(0),$$
$$\hat{P}\mathbf{u}_n(\pi/a) = p_\pi^{(n)}\mathbf{u}_n(\pi/a). \tag{2.33}$$

Here, the parity eigenvalues $p_0^{(n)}$ and $p_\pi^{(n)}$ of band n are $+1$ for symmetric eigenvectors and -1 for antisymmetric eigenvectors upon exchange of the two sublattice components, as in equation 2.28. The parity eigenvalues are relevant, as they can

indicate a so-called band inversion, meaning a change between symmetric and antisymmetric eigenvectors of a band between $k = 0$ and $k = \pi/a$. As proven in appendix A.3, exactly such a band inversion in combination with the present time-reversal symmetry leads to a nonzero Zak phase of a given band. The Zak phase is determined by the parity eigenvalues as [43, 69]

$$\gamma_n = \frac{\pi}{2} \left(1 - p_0^{(n)} p_\pi^{(n)} \right), \tag{2.34}$$

up to an integer multiple of 2π. This is a remarkable result, as, given the symmetries, potentially exhaustive numerical calculations of the Zak phase can be avoided and reduced to the evaluation of the eigenvectors at the two high-symmetry k-points.

For the SSH model with its diatomic basis, a symmetric mode means that the masses at the two sublattice sites oscillate in phase, which is true for the so-called acoustic band emerging at zero frequency in the center of the Brillouin zone. In the topologically trivial phase of the acoustic band, i.e., $D_2 < D_1$, the two masses are also in phase at the Brillouin zone boundary, corresponding to parity eigenvalues of $p_0 = p_\pi = +1$ and a Zak phase of zero according to equation 2.34. For the same spring constant configuration, the so-called optical band has parity eigenvalues of $p_0 = p_\pi = -1$, rendering this band trivial as well. However, in the nontrivial phase, both bands exchange their modes' symmetry at the Brillouin zone boundary. The bands are inverted and acquire a Zak phase of $\gamma_1 = \gamma_2 = \pi$. Having both bands in the nontrivial phase simultaneously is in accordance with section 2.2.4, stating that the complete vector bundle of all bands is always trivial with a total winding number of zero: The total Zak phase for both bands is $\gamma_1 + \gamma_2 = 2\pi$ and hence equivalent to zero due to its definition and its $\mathcal{Z}_2$ character. To account for this, we can define a topological index κ that determines the topological phase of a set of selected bands n' with individual Zak phases $\gamma_{n'}$ as

$$\kappa = \frac{1}{2} \left(1 - e^{i \sum_{n'} \gamma_{n'}} \right), \tag{2.35}$$

which is 0 for a trivial set and 1 for a nontrivial set. It can be directly seen that the bundle of both bands is also trivial when both bands are trivial themselves, with $\gamma_1 = \gamma_2 = 0$. The above equation will be especially useful, when discussing band gaps that separate subsets consisting of more than one band, as in the next chapter. There, the topological index κ of the subset of all bands below a band gap can be understood as the topological index of the band gap itself, such that $\kappa = 1$ indicates a topological band gap.

2.3.4 Unit Cell Convention

Although the topological classification with the trivial phase for $D_2 < D_1$ and nontrivial phase for $D_2 > D_1$ seemed to be conclusive, it has a tremendous loophole. So far we have omitted that, when setting up the SSH model with its equations of motion 2.19, one is free to chose the unit cell convention. In Figure 2.5, a natural alternative is a unit cell that is shifted by half a lattice constant. This simply interchanges the intracell and intercell spring constants, $D_1 \rightarrow D_2$ and $D_2 \rightarrow D_1$, respectively, such that literally all observations from above would become obsolete. The trivial topological phase flips to the nontrivial phase and vice versa just by arbitrarily changing unit cell convention. This is a particular property of the 1D periodic SSH model. Formally, this is reflected by a gauge dependency of the Zak phase with respect to a spatial shift of the unit cell. From equations 2.5 and 2.7, it follows that a spatial shift $b = a/2$ of half the unit cell size changes the original to new Bloch eigenvectors, $\mathbf{u}_n(k)$ and $\mathbf{u}'_n(k)$, respectively, by a phase factor:

$$\mathbf{u}'_n(k) = \mathrm{e}^{-\mathrm{i}kb}\mathbf{u}_n(k). \tag{2.36}$$

Plugging this into the equation 2.13 results in two different Zak phases γ_n and γ'_n for the two conventions [70]:

$$\gamma'_n = \gamma_n + \frac{2\pi}{a}b = \gamma_n + \pi, \tag{2.37}$$

which indeed interchanges trivial and nontrivial phases. In fact, the discussion of sections 2.3.2 and 2.3.1 is meaningless for a strictly infinite 1D system. However, we will see in the next section that the topological classification of the SSH model and also the bulk-boundary correspondence gets valid and relevant, when regarding finite systems.

2.3.5 Topologically Protected Boundary Modes

To investigate the features of a finite version of the mechanical SSH model, the mass-spring model obeying the equations of motion 2.19 has to be solved in real-space instead of reciprocal space. In discretized real-space coordinates with all DOF arranged in the vector $\mathbf{U}^{(z)}$, the eigenvalue problem for a finite mass-spring

model with N unit cells reads

$$\hat{Q}\mathbf{U}^{(z)} = \omega_z^2 \mathbf{U}^{(z)},$$

with $\quad \mathbf{U}^{(z)} = \left(\sqrt{m_a} u_{1,a}^{(z)}, \sqrt{m_b} u_{1,b}^{(z)}, ..., \sqrt{m_a} u_{N,a}^{(z)}, \sqrt{m_b} u_{N,b}^{(z)} \right)^T,$

and $\quad \hat{Q} = \begin{pmatrix} \tilde{D}_a & -\tilde{D}_1 & 0 & & 0 \\ -\tilde{D}_1 & \tilde{D}_b & -\tilde{D}_2 & \dots & 0 \\ 0 & -\tilde{D}_2 & \tilde{D}_a & & 0 \\ & \vdots & & \ddots & -\tilde{D}_1 \\ 0 & 0 & 0 & -\tilde{D}_1 & \tilde{D}_b \end{pmatrix},$ \hfill (2.38)

where $\quad \tilde{D}_{a(b)} = \dfrac{D_1 + D_2}{m_{a(b)}} \quad$ and $\quad \tilde{D}_{1(2)} = \dfrac{D_{1(2)}}{\sqrt{m_a m_b}}.$

Here, $\hat{Q}$ is the real space dynamical matrix and z the solution number. The springs at both ends are assumed to be connected to fixed points. Notably, a finite system with open ends will produce different results, as discussed in section 3.3.4. The unit cell convention can now be defined unambiguously by demanding a complete unit cell at the chain's boundary. Terminating the chain at spring D_2 leaves a whole unit cell with D_1 in the center, which makes the unit cell convention with D_1 as intercell spring correct (cf. Fig. 2.5). In contrast, if the mass-spring chain is terminated at a D_1 spring, D_2 would become the intercell spring, and the notation can be adapted via $D_2 \to D_1$ and $D_1 \to D_2$. As discussed in the previous section, this is exactly the change in the unit cell convention that flips the topological phases from trivial to nontrivial and vice versa. According to the bulk-boundary correspondence, this topological phase flip should then also switch between the presence and absence of protected states at the SSH chain's ends.

By solving the eigenvalue problem 2.38 of the finite SSH system numerically, the above reasoning can be verified. Notably, the boundary termination and hence also the appearance of the 0D edge states in the 1D band gap can be controlled independently at both ends. Figure 2.8 shows the eigenfrequencies and two selected eigenmodes of an exemplary mass-spring chain with 49 sites, corresponding to 24 and a half unit cell. The left end corresponds to a topologically trivial termination as in equation 2.38 for $D_2 < D_1$ and exhibits no edge state. However, due to the half unit cell, the right end flips into a nontrivial configuration ($D_2 > D_1$) and consequently a localized state emerges, with its frequency inside of the band gap. Intuitively, the emergence of edge states can be understood in the limit of $D_1 \to 0$, which is called the fully dimerized limit for the electronic SSH model. In this limit, the bulk of the 1D chain is decomposed into isolated pairs of coupled sublattice sites. Each pair exhibits a symmetric and antisymmetric state, generating two flat bulk bands [35]. For the mechanical SSH model, this can be seen in the dispersion
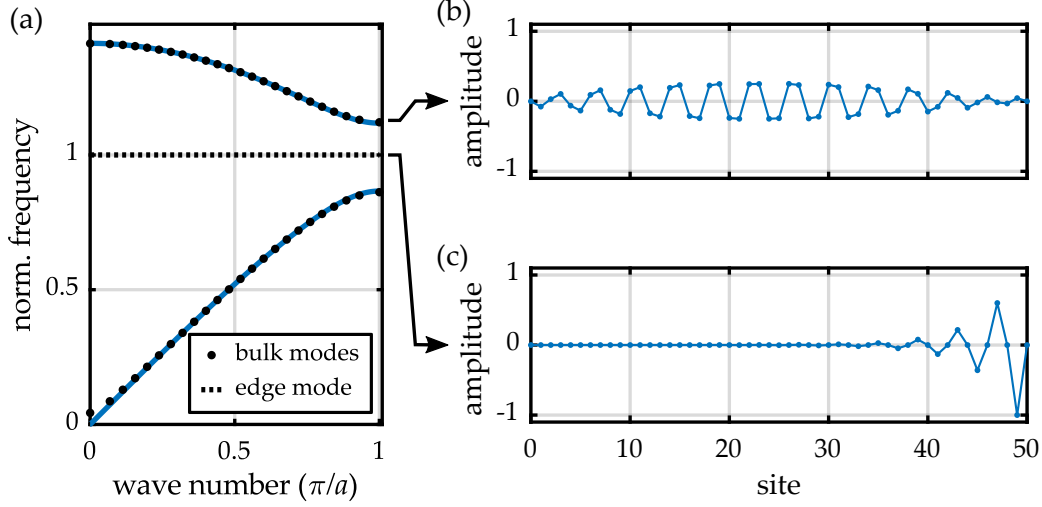
Figure 2.8: Finite SSH mass-spring chain with 49 sites and fixed ends at site 0 and 50. (a) The eigenfrequencies (black dots) of the bulk modes resemble the band structure of the infinite chain (blue line). For each bulk mode, an associated quasi wave number has been calculated via spatial Fourier transformation. A single eigenfrequency (dashed line) lies in the band gap, corresponding to the topological edge mode. (b) Exemplary amplitude pattern of a bulk mode in the upper band. (c) Amplitude pattern of the edge mode. Due to the uneven number of sites, only the right end is in the nontrivial configuration, while the left end is trivial.

relation 2.23, where $\omega_1(k) = 0$ and $\omega_2(k) = \sqrt{2D_2/m}$ for the symmetric and antisymmetric state, respectively. Only for the nontrivial boundary termination, an additional single mass is bound to the fixed end via a spring D_2 (cf. Fig. 2.8(c)). The eigenfrequency of this isolated state is $\sqrt{D_2/m}$, which is in the gap between the two flat bands. Due to the discrete topological nature of the SSH model, this localized state cannot vanish when D_1 is switched on again. Only if the coupling is increased up to $D_1 > D_2$ again, the state vanishes due to the topological phase transition.

It should be noted that such localized states are not only possible at outer boundaries but can also appear at inner boundaries, i.e., at interfaces between a trivial and nontrivial SSH-model domain. This corresponds for instance to an interface with two neighboring D_1 bonds [71]. Interface states of this kind will not be discussed in the course of this work. However, a similar configuration is discussed in chapter 6.

SSH Model as Topological Insulator

The dependence of the edge states on the boundary termination makes the SSH model a quite peculiar topological insulator. Despite very often presented as simple introductory topological toy model [7, 35], it is clearly different from other topological classes, such as the 2D IQHE class. There, an explicit boundary dependency of the topological phase and the edge states is absent. The peculiarity of the SSH model ultimately originates from its dimensionality, combined with the dependence on a spatial symmetry. Following a strictly formal definition, the SSH model itself should be rather seen as one of two topological phases of a generalized model, the so called Rice-Mele model [34, 44, 72].

Nevertheless, it is exactly the boundary-dependence of 1D mirror-symmetric system that provides additional freedom in the design of the edge states. Simply by choosing an appropriate boundary, edge states can switched on or off. That the two configurations are indeed distinct was also proven experimentally via Bloch oscillations in optical lattices [70]. Therein, the gauge invariant difference between the Zak phases of two distinct configurations was measured to be $\Delta\gamma \approx \pi$.

In sections 3.3.4 and 3.4.3, we will see that once edge states are switched on, they are topologically protected and robust against perturbation, such that they stay localized and their eigenfrequencies cannot easily be pushed out of the band gap. Its simple model character combined with its rich topological features lead to a realization of SSH model analogs in various classical systems, ranging from photonic platforms [73–76], over static mechanical lattices [67], water and acoustic waves [77–82], to elastic waves in structured beams [83–85], and extensions such as 2D SSH-like systems [86] and SSH models with nonlinear springs [87]. While topological 1D bulk systems are not able to provide any kind of the often desired protected boundary transport, they are promising for applications that require spatially and spectrally isolated stable modes, e.g., for lasing and sensing [8, 88], and also for the design of a proof-of-principle resonant mechanical laser-beam scanner in the course of this work.

2.4 EFFECTS OF DISSIPATION

In the previous sections, I have already mentioned several realization of topological systems, especially of classical 1D systems mimicking the SSH model. All such real-world experiments are usually subject to dissipation of energy, which affects a system in two ways: First, the resonant behavior of potential boundary states upon excitation will be governed by damping, as described by the well-known damped harmonic oscillator model. Second, the topological phases and the protection of the states itself may be affected, i.e., diminished or even completely lifted. The description of such effects will involve non-Hermitian topological systems. In the following, I will discuss both aspects.

2.4.1 Damped Harmonic Oscillator and Quality Factor

We start with the well-known damping effects on a harmonic oscillator. To integrate damping in mechanical systems, e.g., in the mechanical SSH model of section 2.3, we consider a simple mass-spring system with mass m, real-valued spring constant D', and displacement $u(t)$, comparable to equations 2.19. Furthermore, we introduce a velocity-dependent damping force with damping coefficient β and some external force $F(t)$:

$$\frac{d^2u}{dt^2} + \frac{\beta}{m}\frac{du}{dt} + \frac{D'}{m}u = \frac{F(t)}{m}. \tag{2.39}$$

Though this description is limited to a single mass and spring for clarity, it can be generalized to mass-spring models as in equations 2.21 or 2.38.

When driving the system time-harmonically with angular frequency ω, i.e.,

$$F(t) = \tilde{F}e^{i\omega t} \qquad \text{and} \quad u(t) = \tilde{u}(\omega)e^{i\omega t}, \tag{2.40}$$

the equation for the stationary solution $\tilde{u}(\omega)$ reads

$$-\omega^2\tilde{u} + \frac{D}{m}\tilde{u} = \frac{\tilde{F}}{m} \qquad \text{with} \quad D = D' + i\omega\beta = D' + iD''. \tag{2.41}$$

Here, we have introduced the complex-valued spring constant D with its real and imaginary part, D' and D'', respectively. This will be used in the next section. To characterize the damping, we define the eigenfrequency $\omega_0 = \sqrt{D'/m}$ and the damping ratio $\Gamma = \beta/\sqrt{4mD'}$ and calculate the resonance curve, i.e., the squared spectral amplitude

$$|\tilde{u}(\omega)|^2 = \frac{1}{(\omega_0^2 - \omega^2)^2 + (2\Gamma\omega_0\omega)^2} \cdot \frac{|\tilde{F}|^2}{m^2}. \tag{2.42}$$

The resonance curve has its maximum at $\omega_{\text{res}} = \omega_0\sqrt{1 - 2\Gamma^2}$. In this work, we will only deal with underdamped systems with small damping ratios $\Gamma \ll 1$. In this regime, we can quantify damping with the quality factor Q via the ratio of the resonance frequency to the spectral full width at half maximum (FWHM) $\Delta\omega$ of the resonance curve:

$$Q = \frac{\omega_{\text{res}}}{\Delta\omega} = \frac{\omega_{\text{res}}}{2\frac{\omega_0^2}{\omega_{\text{res}}}\sqrt{\Gamma^2 - \Gamma^4}} = \frac{1 - 2\Gamma^2}{2\sqrt{\Gamma^2 - \Gamma^4}} \overset{\Gamma \ll 1}{\approx} \frac{1}{2\Gamma} \overset{\omega \approx \omega_0}{\approx} \frac{D'}{D''}. \tag{2.43}$$

Thus, in the vicinity of the eigenfrequency ω_0, the quality factor Q is directly given by the ratio of real to imaginary part of the complex spring constant D. Note

that, when using the non-squared resonance amplitude $|\tilde{u}(\omega)|$, a scaled FWHM of $\Delta\omega' = \sqrt{3}\Delta\omega$ is obtained. There, the maximum amplitude is approximately proportional to Q. Another definition for the quality factor uses the total energy E_{tot} in the resonating system divided by the amount of energy ΔE that is dissipated per oscillation:

$$Q = 2\pi \frac{E_{\text{tot}}}{\Delta E}. \tag{2.44}$$

By integrating the damping force over one oscillation, it can be shown that the definitions in equations 2.43 and 2.44 are equivalent for underdamped systems [89]. In case multiple damping mechanisms are present, the damping coefficients add up in equation 2.41 and the total quality factor is

$$\frac{1}{Q_{\text{tot}}} = \sum_i \frac{1}{Q_i}. \tag{2.45}$$

This will become relevant when discussing different contributions to measured total quality factors in section 5.3.3.

2.4.2 Non-Hermitian Topological Systems

I will show in chapters 4 and 5, how dissipation can be strongly reduced to obtain pronounced resonances in mechanical metamaterials. However, the question remains, whether not even the smallest dissipation effects could make the above description in terms of distinct topological classes and topological boundary states obsolete. This question was discussed within the scope of the bachelor's thesis of Steven Kraus in collaboration with Jörg Schmalian [90].

As the eigenproblems to be analyzed in terms of topology, e.g., in equation 2.21, are in frequency domain, we can use the approach of complex spring constants as in equation 2.41. However, replacing the originally real-valued spring constants by complex-valued quantities renders the dynamical matrices, e.g., in equation 2.22, non-Hermitian. At first, this breaks down the formalism of topological band theory as introduced in section 2.2. The eigenvalues corresponding to the squared frequencies, $\lambda_n = \omega_n^2$, are no longer real-valued and, more importantly, the eigenvectors do not form an orthogonal set anymore. To partially recover orthogonality relations for non-Hermitian matrices, the set of left eigenvectors $|\mathbf{u}_{m,\text{L}}\rangle$ is introduced in addition to the right eigenvectors $|\mathbf{u}_{n,\text{R}}\rangle$ [91]:

$$\hat{D}\,|\mathbf{u}_{n,\text{R}}\rangle = \lambda_{n,\text{R}}\,|\mathbf{u}_{n,\text{R}}\rangle\,, \tag{2.46}$$

$$\hat{D}^\dagger\,|\mathbf{u}_{m,\text{L}}\rangle = \lambda_{m,\text{L}}^*\,|\mathbf{u}_{m,\text{L}}\rangle\,, \tag{2.47}$$

$$\Leftrightarrow \quad \langle\mathbf{u}_{m,\text{L}}|\,\hat{D} = \lambda_{m,\text{L}}\,\langle\mathbf{u}_{m,\text{L}}|\,. \tag{2.48}$$

Here, the *k*-dependency of the dynamical matrix, the eigenvectors, and the eigenstates has been omitted for a moment and we use bra-ket notation for convenience. The eigenvalues are assumed to be non-degenerate within the two distinct sets. By combining equations 2.46 and 2.48, we get

$$
\langle \mathbf{u}_{m,\mathrm{L}} | \hat{D} | \mathbf{u}_{n,\mathrm{R}} \rangle = \lambda_{m,\mathrm{L}} \langle \mathbf{u}_{m,\mathrm{L}} | \mathbf{u}_{n,\mathrm{R}} \rangle = \lambda_{n,\mathrm{R}} \langle \mathbf{u}_{m,\mathrm{L}} | \mathbf{u}_{n,\mathrm{R}} \rangle
$$
$$
\Leftrightarrow (\lambda_{m,\mathrm{L}} - \lambda_{n,\mathrm{R}}) \langle \mathbf{u}_{m,\mathrm{L}} | \mathbf{u}_{n,\mathrm{R}} \rangle = 0,
$$

(2.49)

such that we can find pairs of corresponding left eigenvectors and right eigenvectors that can be labeled with $n = m$ and share the same eigenvalue $\lambda_{n,\mathrm{R}} = \lambda_{n,\mathrm{L}} = \lambda_n$. The left and right eigenvectors are biorthogonal, meaning that each left eigenvector is orthogonal to all right eigenvectors except for its corresponding one and vice versa [92]. We can normalize the states by requiring

$$
\langle \mathbf{u}_{m,\mathrm{L}} | \mathbf{u}_{n,\mathrm{R}} \rangle = \delta_{m,n}.
$$

(2.50)

In this form, the left and right eigenvectors can be used to calculate the Zak phase of individual bands via a generalized version of equations 2.13 and 2.14 [93–95]:

$$
\gamma_n^{\mathrm{c}} = - \operatorname{Im} \int_{-\pi/a}^{\pi/a} \langle \mathbf{u}_{n,\mathrm{L}}(k) | \partial_k \mathbf{u}_{n,\mathrm{R}}(k) \rangle \, \mathrm{d}k,
$$

(2.51)

$$
= - \operatorname{Im} \sum_{k_i=-\pi/a}^{\pi/a-\mathrm{d}k} \ln \langle \mathbf{u}_{n,\mathrm{L}}(k_i) | \mathbf{u}_{n,\mathrm{R}}(k_i + \mathrm{d}k) \rangle .
$$

(2.52)

Thus, when switching on dissipation in a 1D topological system, it has to be checked if the quantization of the Zak phase of the non-dissipative system translates into a quantization of the generalized Zak phase. If that is the case, the distinct topological phases and the topological protection of boundary states stay intact.

Notably, for the numerical calculation of the generalized Zak phase, more attention has to be payed to the phase convention as compared to the Hermitian scenario in section 2.3.2. Each of the distinct left and right eigenvectors has its own arbitrary phase factor, which can spoil the result for the generalized Zak phase [96]. In the course of his bachelor's thesis, Steven Kraus defined a transformation that obeys the normalization condition of equation 2.50 and additionally fixes the phases of the left and right eigenvectors in a symmetric manner. The transformation assures a smooth phase evolution and a well-defined generalized Zak phase. It can be found in the appendix A.4. The formalism of the generalized Zak phase can be used for Hermitian problems as well. There, the left eigenvectors are equivalent to the right eigenvectors according to their definition in equation 2.47, thus resembling the standard Zak phase again.

Damped Su-Schrieffer-Heeger Model

Different non-Hermitian extensions of the SSH model have been discussed to study the influence of loss and gain on the system's topology [95, 97]. We will limit ourselves to damping implemented by complex-valued spring constants as discussed in the last two sections. Notably, both time-reversal symmetry and parity symmetry stay preserved under this transition. Therefore, the vector $\mathbf{d}(\mathbf{k})$ of equation 2.30 representing the dynamical matrix is still confined to the complex plane, as shown in Figure 2.6(b). Hence, the quantization of the winding number and the complex Zak phase are preserved. However, as the spring constants D_1 and D_2 are now complex, the center point of the rotating vector $\mathbf{d}(\mathbf{k})$ is not confined to the real axis anymore. As a consequence, the winding number now changes at the characteristic point $|D_1| = |D_2|$ and the topological phase depends also on the imaginary parts of the spring constants.

We will incorporate damping for the coupled SSH mass-spring model in section 3.3. Thereby, we will only consider imaginary parts that are proportional to the real part of each spring constant. Following the above explanation, the topological phases and even the phase transition point should not change by this. For numerical verification, the complex Zak phase equation 2.52 will be evaluated as well.

2.5 CONTINUUM MECHANICS

In this work, the aim is to design and realize a topological mechanical system in the form of 3D structures made of solid material. The static and dynamic behavior of such structured material bodies is captured via the equations of continuum mechanics. In the following, I will introduce the material properties and equations that generalize the case of discrete mass-spring models, as in section 2.3, to continuous mass distributions. The discussion will be limited to the description of an isotropic linear elastic material, including intrinsic material damping in the form of viscoelasticity. For a rigorous and complete introduction, I would like to refer to standard textbooks on continuum mechanics [98–100], which have been the basis for this short overview. As transition to the next chapter, I will present the phononic band structure of an exemplary 1D-periodic structure.

2.5.1 *Stress, Strain, and Motion*

The deformation of a material body is described by its displacement field $\mathbf{u}(\mathbf{r}, t)$, where $\mathbf{r}$ is the continuous space coordinate. As for a mass-spring model, forces are a result of local differences in the displacements which lead to nonzero strains within the material. For a continuous 3D mass distribution, the local strain is

given by the spatial gradient of the three displacement components i along the three dimensions j of the coordinate system. In the limit of small displacement gradients, the strain at each point is approximated by the infinitesimal strain tensor

$$\epsilon_{ij} = \frac{1}{2}\left(\frac{\partial u_i}{\partial r_j} + \frac{\partial u_j}{\partial r_i}\right). \tag{2.53}$$

Similarly, the forces acting within a material body have to be generalized. The local forces acting along coordinate j on a virtual surface with a unit area perpendicular to coordinate i are described by the Cauchy stress tensor σ_{ij}. Now the relation between displacements and force can be transformed to the relation between strain tensor $\hat{\epsilon}$ and stress tensor $\hat{\sigma}$. For a linear elastic Cauchy continuum, this leads to a generalized version of Hook's law:

$$\sigma_{ij} = C_{ijkl}\epsilon_{kl}, \tag{2.54}$$

using Einstein summation convention. The tensor $\hat{C}$, called stiffness tensor or elasticity tensor, defines the material properties. Assuming an isotropic material, the entries of this fourth-order tensor are fully defined by two material parameters, e.g., by Young's modulus E and the Poisson's ratio ν [100]:

$$C_{ijkl} = \frac{E}{2(1+\nu)}\left(\delta_{il}\delta_{jk} + \delta_{ik}\delta_{jl}\right) + \frac{E\nu}{(1+\nu)(1-2\nu)}\delta_{ij}\delta_{kl}. \tag{2.55}$$

Here, the Young's modulus E measures the stiffness of the isotropic material via the ratio of stress σ_{11} to strain ϵ_{11} that is induced along the same direction [101]:

$$E = \frac{\sigma_{11}}{\epsilon_{11}}. \tag{2.56}$$

The Poisson's ratio ν is defined via the lateral strain, i.e., ϵ_{22} or equally ϵ_{33}, that goes along with a strain ϵ_{11} in the perpendicular direction [101],

$$\nu = -\frac{\epsilon_{22}}{\epsilon_{11}}. \tag{2.57}$$

With the mass density ρ of the material, the equations of motion for a linear elastic material can now be written in terms of the components of the displacement and stress at each point [100]:

$$\rho\frac{\partial^2 u_j}{\partial t^2} - \frac{\partial \sigma_{ij}}{\partial r_i} = \rho\frac{\partial^2 u_j}{\partial t^2} - C_{ijkl}\frac{\partial^2 u_k}{\partial r_j \partial r_l} = f_j, \tag{2.58}$$

where f_j are components of a potential force field acting on the body, e.g., due to gravity. Leaving such forces aside and using a longitudinal plane wave ansatz,

the equations 2.53 to 2.55 plugged into equation 2.58 result in a linear dispersion relation:

$$\omega(k) = \sqrt{\frac{C_{1111}}{\rho}}k = \sqrt{\frac{E(1-\nu)}{\rho(1+\nu)(1-2\nu)}}k = c_1 k. \qquad (2.59)$$

In chapter 3, we will use the phase velocity c_1 of the longitudinal plane wave propagating in a bulk material to normalize the dispersion relation of the periodic 3D structures with respect to their material parameters. Comparable to the procedure in equation 2.24 for mass-spring models, normalized frequencies $\tilde{f}$ and ordinary frequencies f are linked via

$$\tilde{f} = \frac{a}{\lambda} = f\frac{a}{c_1}, \qquad (2.60)$$

where λ_1 is the wavelength of the longitudinal mode and a the unit cell size of the periodic structure.

2.5.2 Viscoelasticity

In section 2.4.1, a velocity-dependent damping force has been introduced to account for losses in mass-spring systems. For a bulk materials, damping arises due to a viscous contribution to the ideal linear elastic material behavior of equation 2.54 [98]. When working in frequency domain, this damping can also be absorbed by introducing an imaginary part that adds to the originally real-valued material parameters.

For a real-world material, the viscous behavior cannot be captured via a single damping term. Instead, the material has to be modeled via the so-called generalized Maxwell model to account for relaxation and retardation mechanisms [102]. Within this model, the material's relation between stress σ and strain ϵ in one dimension is modeled by multiple Maxwell elements which are connected in parallel. Thereby, each Maxwell element consist of a spring with spring constant E_i which is connected in series to a damper of viscosity η_i. The total stress σ in the material is then given by the sum of the stresses σ_i of the individual elements:

$$\sigma = E_0\epsilon + \sum_i \sigma_i. \qquad (2.61)$$

Here, E_0 represents the Young's modulus of the material in the static limit. For each Maxwell element, the strain rate $\dot{\epsilon}_i$ is given by the contributions of its spring and its damper [98]:

$$\dot{\epsilon}_i = \frac{\dot{\sigma}_i}{E_i} + \frac{\sigma_i}{\eta_i}. \qquad (2.62)$$

Assuming time-harmonic stresses and strains with an angular frequency of ω in above equations, the overall dynamic stress-strain relation of the generalized

Maxwell model results in

$$
\begin{aligned}
\tilde{\sigma}(\omega) &= \left(E_0 + \sum_i E_i \frac{\omega^2 \tau_i^2}{1 + \omega^2 \tau_i^2} - \mathrm{i} \sum_i E_i \frac{\omega \tau_i}{1 + \omega^2 \tau_i^2} \right) \tilde{\epsilon}(\omega) \\
&= (E' + \mathrm{i} E'') \tilde{\epsilon}(\omega),
\end{aligned}
\tag{2.63}
$$

with the characteristic relaxation times $\tau_i = \eta_i / E_i$ of the individual elements. Thus, for a linear viscoelastic material, we can use the complex dynamical Young's modulus $E = E' + \mathrm{i} E''$ for calculations in frequency domain. In analogy to section 2.4.1, the material damping can be characterized by the quality factor, which is approximately $Q = E'/E''$ for an underdamped system. Within the generalized Maxwell model, the real part E' of the complex dynamical Young's modulus approaches a constant value for sufficiently large frequencies $\omega \gg 1/\tau_i$, while the imaginary part E'' vanishes. In the experiments in chapter 5, the materials will be subject to dynamic stresses and strains with frequencies in the ultrasound regime. Thereby, the investigations are mostly limited to small frequency intervals, such that we will assume a constant complex dynamical Young's modulus in corresponding calculations.

2.5.3 Phononic Band Structures of Solid Periodic Structures

The equations of section 2.5.1 are sufficient to describe the static and dynamic behavior in a solid bulk in linear approximation. However, to be able to analyze 3D structured material bodies, these partial differential equations have to be solved on a potentially complex continuous domain, while respecting the given boundary conditions. The numerical tool of choice for problems of this kind is the finite-element method (FEM) [100, 103]. There, the continuous domain, for instance of a material body, is discretized into small volume elements, as shown in Figure 2.9. The differential equations are then solved only at the elements' corners, also called the nodes of the finite-element mesh, and interpolated within. A short summary of the FEM procedure for continuum mechanics is provided in appendix A.5.

In this work, the eigenmodes and response spectra of mechanical 3D structures are solved by frequency-domain FEM calculations via the commercial software COMSOL Multiphysics. In the solid mechanics module of the software, the equations of continuum mechanics are implemented, as well as the routine to define the finite elements and the matrix solver to calculate the total 3D displacement fields.

The calculation of phononic band structures of solid periodic structures goes along the same lines as for the discrete mass-spring model in section 2.3. One has to consider only a single unit cell and impose the proper boundary condi-
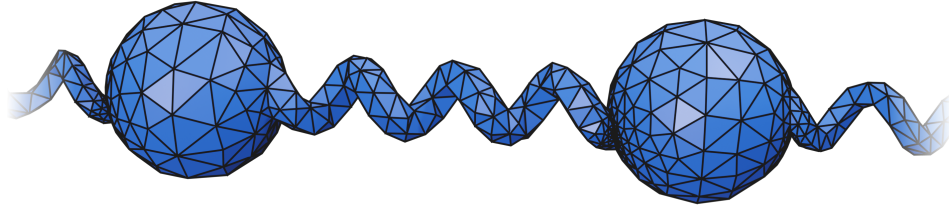
Figure 2.9: Finite-element decomposition for a solid mass-spring model with a tetrahedral mesh generated by COMSOL Multiphysics.

tions along the dimension of periodicity. Following the definition of the Bloch eigenmodes in equation 2.4, the spatial phase factor arising in the real-space displacement field $\mathbf{u}(\mathbf{r})$ between opposite sides at the planes $\mathbf{R}$ and $\mathbf{R} + \mathbf{a}$ of the unit cell is

$$\mathbf{u}(\mathbf{R} + \mathbf{a}) = e^{ik\mathbf{a}}\mathbf{u}(\mathbf{R}). \tag{2.64}$$

This so-called Floquet-Bloch periodicity can be imposed onto the corresponding boundaries in the FEM calculations to obtain the eigenfrequencies and eigenmodes for a given wave number k. The number of degrees of freedom for a continuous solid structure is infinite. In the FEM calculations with N nodes it is equal to $3N$, which is usually a large number. As a consequence, a large amount of frequency bands emerge in the band structure. While the low-frequency bands resemble the fundamental transverse (shear), rotational (torsional), and longitudinal (pressure) modes that also appear in a bulk continuum or a solid beam, additional bands appear due to higher-order backfolding of these modes, as shown exemplary in Figure 2.10. Additionally local resonances of individual structural elements can emerge. In the next chapter, the rotational and longitudinal modes and their interaction in a mechanical metamaterial will be relevant. Bands due to higher-order backfolding and local resonances in the same frequency regime will be highly undesired, as they potentially couple to the modes of interest, thereby rendering a correct description via a simple effective model elusive.

Zak Phase Calculation

In principle, the Zak phase of the phononic bands can be calculated in the same way as for a simple mass-spring model. However, the number of components of the FEM Bloch vector $|\mathbf{u}(k)\rangle$ that have to be summed up to evaluate the scalar product in equation 2.32 will drastically increase. At the same time, to get a smooth Zak phase evolution, the calculation will also require a high resolution in k-space. Indeed, for a specific 1D continuous periodic acoustic system, such Zak phase calculations were conducted explicitly [78]. However, for a complex elastic structure, the overall FEM calculations would be computationally extremely
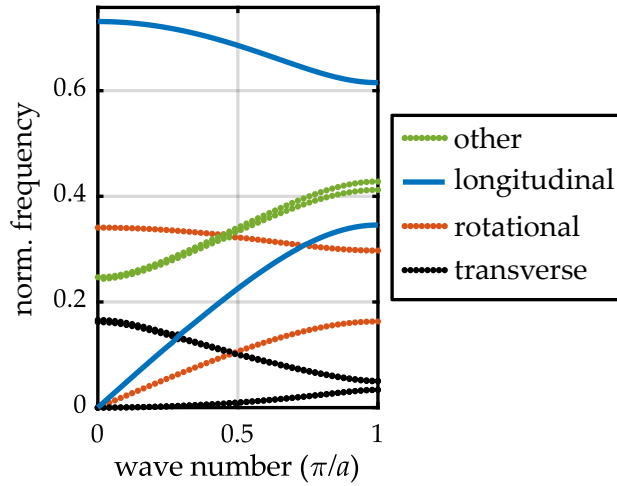
Figure 2.10: Exemplary phononic band structure of a solid mass-spring chain as in Figure 2.9. The lowest ten eigenfrequencies per wave number k, obtained via FEM calculations, are shown. In contrast to a mass-spring model with only two longitudinal (axial) DOF per unit cell, a solid structure has infinitely many DOF, which reduce to $3N$ DOF in a corresponding FEM band structure calculation with N mesh nodes per unit cell. Fundamental transverse (shear) and rotational (torsional) bands as well as other bands emerge, e.g., due to higher-order backfoldings or local resonances.

costly and bring parameter sweeps and optimization routines out of reach. Hence, as an efficient alternative, we will rely on the symmetry of the displacements fields to obtain the Zak phase via the band inversion procedure, as presented in section 2.3.3.

3 Chapter 3
Design of a Chiral Topological Metamaterial

In this chapter, I will show the step-by-step design of a chiral mechanical metamaterial beam that exhibits a 1D topologically nontrivial band gap and associated protected modes at the boundary of a finite system. Such a metamaterial beam can resonantly convert a small axial excitation to a large rotational oscillation and will be used to design a proof-of-principle mechanical laser-beam scanner.

First, I will explain the general concept of metamaterials and introduce a 3D chiral mechanical metamaterial cell that was developed by Tobias Frenzel *et al.* [15–17]. Based on this metamaterial cell, I will derive a mass-spring model that resembles two coupled Su-Schrieffer-Heeger (SSH) models. I will explore the topological features of this model and identify the parameter regime that provides the desired topologically protected edge modes. From the findings of the mass-spring model, I will infer the design of a corresponding chiral metamaterial beam and investigate its band structure and edge resonances via finite-element method (FEM) calculations. I will close the chapter by summarizing the findings for both the mass-spring model and the chiral metamaterial beam.

The key theoretical findings of this chapter have already been published previously [104]. In this thesis, the geometrical dimensions and material parameters used for the metamaterial beam calculations have been adapted according to the fabricated structures, as will be presented in chapter 4. I have conducted all calculations on the infinite and finite version of the coupled SSH model. Also, I have developed the design of the metamaterial beam and conducted corresponding FEM calculations. Together with Tobias Frenzel, I have worked out the chirally coupled mass-spring model. Jörg Schmalian has strongly contributed to the topological classification of the coupled SSH model. Martin Wegener has had an advisory role in all aspects.

3.1 3D CHIRAL MECHANICAL METAMATERIALS

A metamaterial can be defined as a rationally designed structure with extraordinary effective material properties that go qualitatively or quantitatively beyond those of its constituent materials [10]. In contrast to natural or artificial composite materials, such as wood or concrete, a metamaterial is assembled out of tailored building blocks which provide a specific functionality and thereby govern the metamaterials' behavior. Usually, these building blocks are arranged periodically along one, two, or all three dimensions of space.

At the latest after the term *metamaterial* was coined in 2001 by Walser in the context of electromagnetism [105], the concept was established in various fields and evolved quickly. The plenty of proposals and realizations of metamaterials is summarized and reviewed in several publications [10, 106, 107], some focusing on optics and photonics [108–110], or acoustics and mechanics [12, 111–114]. Prominent examples in different fields are optical metamaterials with negative refractive index, first shown in the microwave regime and later realized in the visible spectrum [115, 116], thermal cloaks [117], and chainmail-like metamaterials that reverse the sign of the effective Hall coefficient [118–120]. In mechanics, some research seeks to push effective material parameters toward their theoretical bounds, e.g., via ultralight, ultrastiff, and ultrastrong materials [11, 121], or via auxetic metamaterials, i.e., materials with negative effective Poisson's ratio [122, 123]. Other mechanical metamaterials exhibit remarkable properties in response to acoustic waves or outer conditions, such as optimal sound absorbers or reusable shock absorbers [124, 125], and metamaterials with negative effective thermal expansion or negative effective compressibility [126, 127].

The design of a specific metamaterial is usually posed as an inverse problem where the desired effective property and functionality is given as starting point and the therefore required building block and its spatial arrangement is the outcome. Depending on the target, the working principle of a metamaterial can be based on a non-resonant or resonant mechanism and might only function in the presence or absence of certain symmetries. Once a proper mechanism has been identified, a common goal is to map the metamaterial's behavior, at least in a certain regime of operation, to effective material properties [10, 128]. However, especially for structures that rely on dynamic and resonant effects, such as phononic crystals with ordinary or even topological band gaps, as presented in the last chapter, it is conceptually difficult to extract effective material parameters [10]. Also for the 1D topological mechanical metamaterial that I will present in the following sections it will not be the aim to infer an effective material description. Instead, the goal is to obtain a specific functionality. Still, on the way there, the working mechanism of chiral cubic mechanical metamaterials, which can indeed be described in terms of an effective material [15, 16], will be used. Furthermore, the metamaterial cell will be mapped to a mass-spring model with effective spring constants.
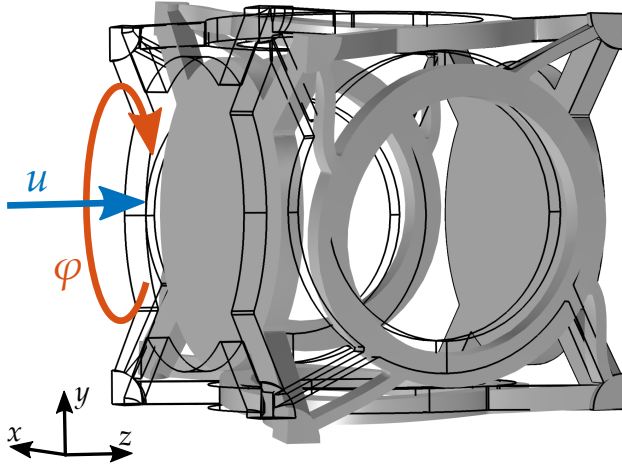
Figure 3.1: A chiral cubic metamaterial cell. The chiral cell is a uniaxial version of the cell designed by Tobias Frenzel *et al.* [15]. When pushing along the z-direction onto the left plate while fixing the right one, the axial push with displacement u causes a rotation φ around the z-axis. This push-to-twist coupling is induced via the chiral ring elements on the four sides and can be used to convert an axial to a rotational motion. The wireframe shows the cell in undeformed state.

3.1.1 *Chirality and Push-to-Twist Coupling*

Generally, an object is called chiral if it is distinct from its mirror image, in a sense that it cannot be superimposed with its mirror image by means of translation or rotation [129]. This happens, if the object lacks centrosymmetry, mirror symmetries, and rotation-reflection symmetries [130–132]. Chiral objects of both natural and artificial kind are ubiquitous and appear on all scales, ranging from spiral galaxies over screws, springs, and the human's own hands, down to enantiomeric molecules. Notably, more than half of modern medical drugs rely on chiral molecules, and the effects and side effects of two distinct mirror-imaged molecules can be drastically different due to chiral receptors in the human organism [133]. Indeed, in most cases, chirality imposes a preference onto a system, may it be the preference of a biological receptor toward a certain enantiomer, or the direction in which a screw should be driven. Similarly, in the case of chiral mechanical metamaterials, we will make use of a preferential twist direction upon a push, the so-called push-to-twist mechanism.

3D chiral mechanical metamaterials have recently been investigated in detail, both theoretically and experimentally [15–17, 132, 134]. An exemplary characteristic building block of such metamaterials is the chiral cubic cell as introduced by Tobias Frenzel [15]. Metamaterials composed of this building block have a pronounced push-to-twist mechanism in the static regime, as shown in Figure 3.1. Additionally, in the dynamical regime, they exhibit acoustical activity, meaning that the linear polarization axis of a transverse elastic wave will rotate upon propagation in the metamaterial's bulk [17]. Chiral metamaterials can be described via a generalized effective medium theory, i.e., micropolar continuum mechanics [15,

135, 136]. Within this theory, rotational degrees of freedom (DOF) φ_k are allowed in addition to the translational DOF u_l at each position of the material. The generalized Hook's law introduced in section 2.54 thereby gets extended by a second equation and additional terms, including the tensors $B_{ijkl} = B'_{klji}$ to account for the chiral coupling between rotation and translation [15]:

$$
\begin{aligned}
\sigma_{ij} &= C_{ijkl}\epsilon_{kl} + B_{ijkl}\varphi_{kl}, \\
t_{ij} &= A_{ijkl}\varphi_{kl} + B'_{ijkl}\epsilon_{kl}, \\
\text{with} \quad \epsilon_{kl} &= \frac{\partial u_l}{\partial r_k} - \varepsilon_{klm}\varphi_m, \qquad \varphi_{kl} = \frac{\partial \varphi_k}{\partial r_l},
\end{aligned}
\tag{3.1}
$$

and the Levi-Civita symbol ε_{klm}. Here, t_{ij} is called the coupled stress tensor and A_{ijkl} is the corresponding generalized elasticity tensor. In this work, we will not use the above continuum equations but rather a reduced and discretized version that describes the uniaxial push-to-twist mechanism in an individual metamaterial cell. For a single cubic cell as displayed in Figure 3.1, we can assign masses m and moments of inertia j to adjacent plates. Fixing one of the two plates while imposing a z-displacement u and an angle of rotation φ around the z-axis, an axial force F and a torque τ is induced:

$$
\begin{aligned}
F &= m\frac{\mathrm{d}^2 u}{\mathrm{d}t^2} = -Du - B\varphi, \\
\tau &= j\frac{\mathrm{d}^2\varphi}{\mathrm{d}t^2} = -A\varphi - B'u.
\end{aligned}
\tag{3.2}
$$

The effective longitudinal (axial) spring constant D, the effective torsional spring constant A, and the effective longitudinal-torsional coupling constants B and B' are dependent on the exact geometry of the chiral cube cell. It holds $B = B'$ due to energy conservation.

In section 3.3, I will use this effective mass-spring approach to design a topological mechanical metamaterial beam by combining the push-to-twist mechanism with the topological features of the SSH model introduced in the last chapter. Notably, for a complete description of the fundamental degrees of freedom of a metamaterial beam, also transverse (shear) displacements would have to be taken into account, as explained in section 2.5.3. Still, within the micropolar continuum theory [136], the transverse DOF live in an orthogonal subspace, i.e., they are decoupled from the longitudinal and rotational DOF and do not have to be included in the effective mass-spring model.
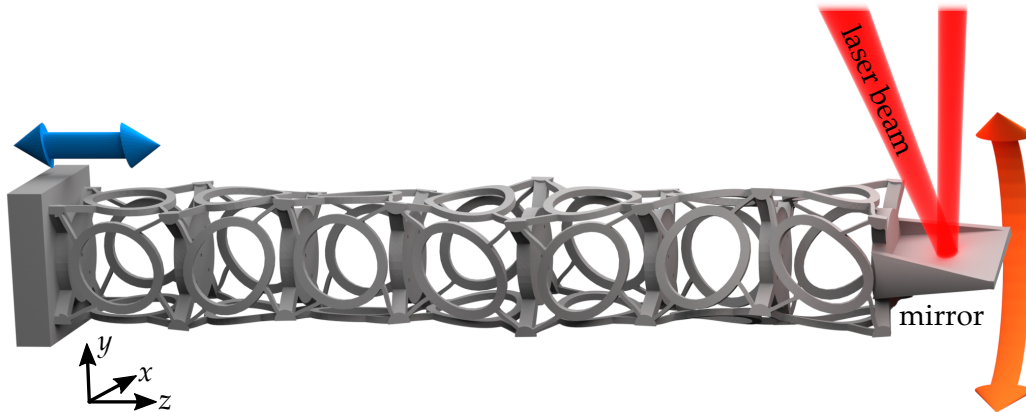
Figure 3.2: Concept of a resonant mechanical laser-beam scanner. Using a topo-logically protected edge mode, an axial excitation (blue arrow) at the left side is transformed to a rotational motion (orange arrow). The rotation is localized to the right end and resonantly enhanced with respect to the excitation. By the topological protection, a perturbation in the form of a mirror can be added without destroying the edge mode, allowing to scan a laser beam. Adapted from [137] (CC BY 4.0).

3.2 COMBINING CHIRALITY AND TOPOLOGY

The aim of this work is to design a chiral metamaterial beam that converts axial to rotational oscillations, serving to realize a resonant mechanical laser-beam scanner that operates at frequencies in the kilohertz regime. As introduced in the previous section, the conversion from axial to rotational motion is already provided by the push-to-twist coupling mechanism of the chiral cubic cell [15]. Hence, the simplest design approach for the laser-beam scanner would be to stack chiral cells along one dimension to obtain a metamaterial beam. When exciting this beam at one end with an axial oscillation, e.g., provided by a piezoelectric transducer, this would convert to a torsional oscillation after a certain distance of propagation. A mirror plate attached at that position would rotate and thereby allow to scan a laser beam. However, this basic approach has two major downsides: First, in the kilohertz regime, the axial excitation that can be provided by a piezoelectric transducer is notoriously small, with amplitudes in the range of a few nanometers only. On top, the excitation can also be undefined, meaning that it can contain undesired transverse motion. Second, as one picks up the rotational motion at the point of the mirror, the beam scanner's mode of operation will be perturbed and not working as designed anymore.

To overcome these two problems, it is advantageous to introduce a topologically protected mode into the metamaterial beam. Via this mode, the rotational amplitude can be resonantly enhanced with respect to the axial excitation amplitude

while making it robust to potential modifications or defects of the structure. The conceptual working principle of a resonant mechanical laser-beam scanner based on such a topological edge mode is shown in Figure 3.2. It consists of a finite chiral metamaterial beam that exhibits a topologically protected torsional mode, in the following also called rotational or twist mode. As introduced in chapter 2, such a protected mode has its frequency inside of a band gap and its rotation amplitude has to be localized to one of the beam's end. Due to the topological protection, we can attach a mirror plate to this end, without significantly affecting the mode and without pushing its frequency out of the band gap. In this configuration, the twist edge mode can be excited axially (longitudinally) from the other end of the beam via evanescent waves, while it is otherwise spatially and spectrally decoupled from its surrounding. This decoupling makes sure that the resonant rotational oscillation of the mirror is not perturbed by other undesired mechanical motion, such as transverse oscillations.

3.3 THE COUPLED SU-SCHRIEFFER-HEEGER MODEL

To introduce the desired topological twist edge mode into a chiral metamaterial beam, we design an extended version of the mechanical Su-Schrieffer-Heeger model presented in section 2.3. Thereby, the topological effect of a diatomic basis and the chiral push-to-twist mechanism are combined. For the chiral metamaterial beam, the diatomic basis can be realized by stacking alternating cube cells, which are distinct in their effective spring constants according to equation 3.2. Reducing the configuration to an effective mass-spring model, as shown in Figure 3.3, the system can be described via four degrees of freedom per unit cell. These are the longitudinal displacements $u_{i,a}$ and $u_{i,b}$ and the rotations $\varphi_{i,a}$ and $\varphi_{i,b}$ of the structure's plates at the two sublattice sites a and b. The resulting equations of motion for sublattice site a of unit cell i are

$$
\begin{aligned}
m_a \ddot{u}_{i,a} =& D_1 \left(u_{i,b} - u_{i,a} \right) + D_2 \left(u_{i-1,b} - u_{i,a} \right) \\
&+ B_1 \left(\varphi_{i,b} - \varphi_{i,a} \right) + B_2 \left(\varphi_{i-1,b} - \varphi_{i,a} \right),
\end{aligned}
\tag{3.3}
$$

$$
\begin{aligned}
j_a \ddot{\varphi}_{i,a} =& A_1 \left(\varphi_{i,b} - \varphi_{i,a} \right) + A_2 \left(\varphi_{i-1,b} - \varphi_{i,a} \right) \\
&+ B_1 \left(u_{i,b} - u_{i,a} \right) + B_2 \left(u_{i-1,b} - u_{i,a} \right),
\end{aligned}
\tag{3.4}
$$

where D_1 (D_2), A_1 (A_2), and B_1 (B_2) are the intracell (intercell) effective coupling constants of the two distinct chiral cell types. Equivalent equations can be derived for sublattice site b.
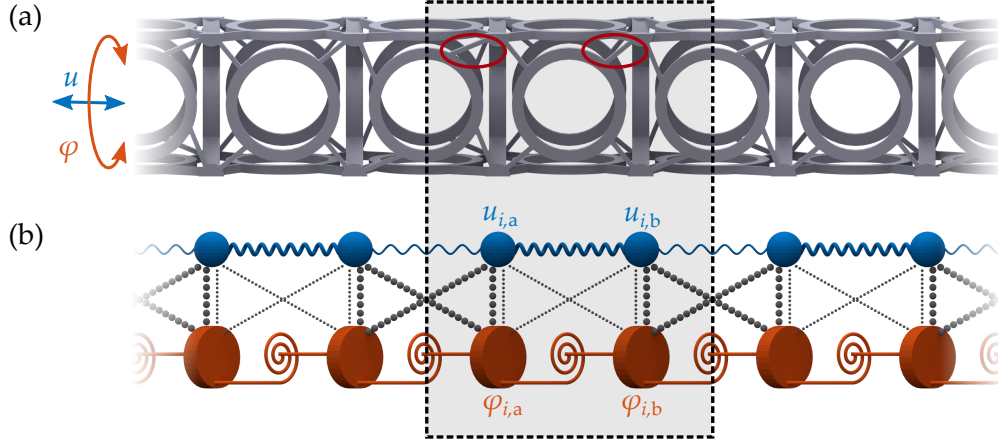
Figure 3.3: Mapping a chiral metamaterial beam to a diatomic mass-spring model. (a) The metamaterial beam consists of chiral cube cells that are alternated by a subtle structural difference (red ellipses). The vertical plates between the rings can be mapped to discrete elements with a given mass and moment of inertia, coupled via effective springs. (b) The resulting mass-spring model has both a longitudinal (axial) DOF u (in blue) and a rotational DOF φ (in orange) at each of the two sublattice sites a and b per unit cell (dashed gray box). The longitudinal and rotational subsystem each resembles a mechanical SSH model, with additional coupling due to chirality (dotted lines). Adapted from [104] with permission.

Using a wave ansatz as for the simple SSH model in equation 2.20, we get the temporally and spatially Fourier-transformed equations in matrix form:

$$\hat{D}(k)\mathbf{u}_n(k) = \omega_n^2(k)\mathbf{u}_n(k),$$

$$\text{with} \quad \mathbf{u}_n(k) = \left(\sqrt{m_\mathrm{a}}u_{n,\mathrm{a}}(k), \sqrt{m_\mathrm{b}}u_{n,\mathrm{b}}(k), \sqrt{j_\mathrm{a}}\varphi_{n,\mathrm{a}}(k), \sqrt{j_\mathrm{b}}\varphi_{n,\mathrm{b}}(k) \right)^T. \tag{3.5}$$

The Bloch vectors $\mathbf{u}_n(k)$ of the four bands with band index n contain the four degrees of freedom, normalized with respect to the masses $m_\mathrm{a(b)}$ and moments of inertia $j_\mathrm{a(b)}$ at the two sublattice sites. With this, the wave-number-dependent dynamical matrix is given by

$$\hat{D}(k) = \begin{pmatrix} \frac{D_1+D_2}{m_\mathrm{a}} & \frac{-D_1-D_2\mathrm{e}^{-ika}}{\sqrt{m_\mathrm{a}m_\mathrm{b}}} & \frac{B_1+B_2}{\sqrt{m_\mathrm{a}j_\mathrm{a}}} & \frac{-B_1-B_2\mathrm{e}^{-ika}}{\sqrt{m_\mathrm{a}j_\mathrm{b}}} \\ \frac{-D_1-D_2\mathrm{e}^{ika}}{\sqrt{m_\mathrm{a}m_\mathrm{b}}} & \frac{D_1+D_2}{m_\mathrm{b}} & \frac{-B_1-B_2\mathrm{e}^{ika}}{\sqrt{m_\mathrm{b}j_\mathrm{a}}} & \frac{B_1+B_2}{\sqrt{m_\mathrm{b}j_\mathrm{b}}} \\ \frac{B_1+B_2}{\sqrt{m_\mathrm{a}j_\mathrm{a}}} & \frac{-B_1-B_2\mathrm{e}^{-ika}}{\sqrt{m_\mathrm{b}j_\mathrm{a}}} & \frac{A_1+A_2}{j_\mathrm{a}} & \frac{-A_1-A_2\mathrm{e}^{-ika}}{\sqrt{j_\mathrm{a}j_\mathrm{b}}} \\ \frac{-B_1-B_2\mathrm{e}^{ika}}{\sqrt{m_\mathrm{a}j_\mathrm{b}}} & \frac{B_1+B_2}{\sqrt{m_\mathrm{b}j_\mathrm{b}}} & \frac{-A_1-A_2\mathrm{e}^{ika}}{\sqrt{j_\mathrm{a}j_\mathrm{b}}} & \frac{A_1+A_2}{j_\mathrm{b}} \end{pmatrix}. \tag{3.6}$$

Here, a is the lattice constant. Notably, the dynamical matrix perfectly resembles two individual mechanical SSH models on the two 2×2 diagonal blocks. One

SSH model represents the longitudinal DOF and the other one the rotational DOF, with a chiral coupling of both via the off-diagonal blocks. In terms of the above eigenproblem it is possible to investigate the band structure and its topology along the lines of the simple SSH model in section 2.3.

3.3.1 Symmetry Classification

The analysis starts with the symmetry classification [42] of the dynamical matrix $\hat{D}(k)$ in equation 3.6. Assuming only real-valued coupling constants and thereby neglecting damping effects, the dynamical matrix is a Hermitian operator with $\hat{D}^{\dagger}(k) = \hat{D}(k)$. We find that

$$\hat{T}\hat{D}^{T}(k)\hat{T}^{-1} = \hat{D}(-k) \quad \text{with} \quad \hat{T}^2 = (\sigma_0 \otimes \sigma_0)^2 = +1, \tag{3.7}$$

resembling bosonic time-reversal symmetry. A more general consideration including damping effects will be discussed briefly in section 3.3.5. Following the results of the simple SSH model, we require a second, spatial symmetry to be present in order to generate distinct topological phases with a quantized Zak phase as their $\mathcal{Z}_2$ topological index. Such a symmetry is established by forcing the masses and moments of inertia at the two sublattice sites to be equal, i.e., $m_a = m_b = m$ and $j_a = j_b = j$. Then it holds

$$\hat{P}\hat{D}(k)\hat{P}^{-1} = \hat{D}(-k) \quad \text{and} \quad \hat{P}^2 = +1,$$

$$\text{with} \quad \hat{P} = \sigma_0 \otimes \sigma_x = \begin{pmatrix} 0 & 1 & 0 & 0 \\ 1 & 0 & 0 & 0 \\ 0 & 0 & 0 & 1 \\ 0 & 0 & 1 & 0 \end{pmatrix}. \tag{3.8}$$

As for the SSH model, the parity operator $\hat{P}$ corresponds to an inversion or mirror symmetry and exchanges the two sublattice sites in the Bloch vector:

$$\hat{P} \begin{pmatrix} \sqrt{m}\, u_{n,a}(k) \\ \sqrt{m}\, u_{n,b}(k) \\ \sqrt{j}\, \varphi_{n,a}(k) \\ \sqrt{j}\, \varphi_{n,b}(k) \end{pmatrix} = \begin{pmatrix} \sqrt{m}\, u_{n,b}(k) \\ \sqrt{m}\, u_{n,a}(k) \\ \sqrt{j}\, \varphi_{n,b}(k) \\ \sqrt{j}\, \varphi_{n,a}(k) \end{pmatrix}. \tag{3.9}$$

With the two symmetries $\hat{T}$ and $\hat{P}$, the coupled system is a topological crystalline insulator. Due to the dimensionality of the dynamical matrix, the quantization of the associated winding number and the formation of distinct topological phases cannot be easily visualized and verified via a rotating vector $\mathbf{d}(k)$ as in section 2.3.1. However, we can calculate the bands' Zak phases. Additionally, by knowing the parity operator $\hat{P}$, the principle of band inversion as introduced in section 2.3.3
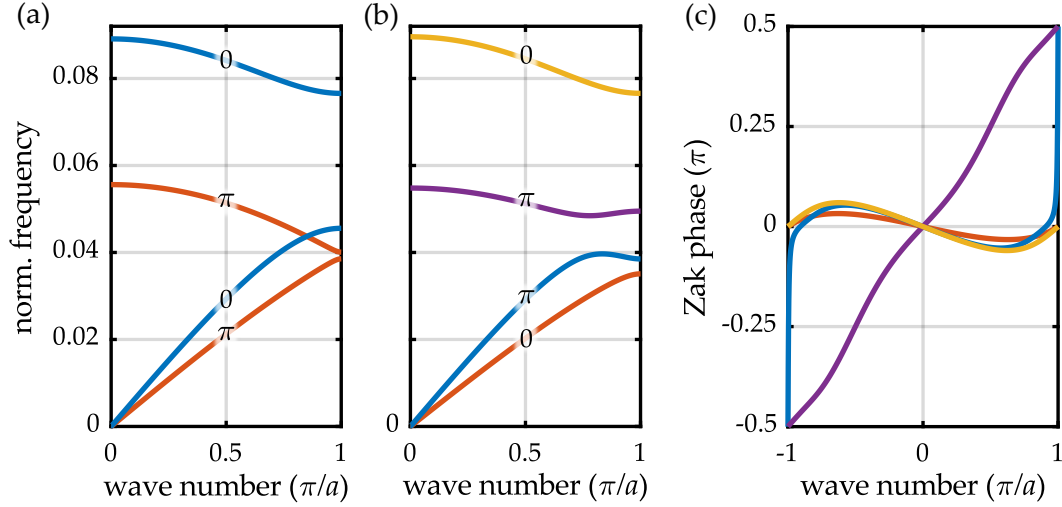
Figure 3.4: Band structures and Zak phase evolution of two (a) uncoupled SSH models ($B_1 = B_2 = 0$), accounting for longitudinal (blue) and rotational (orange) modes. (b) By chirally coupling the two subsystems, the modes mix and a band gap opens up via an avoided crossing between the second and third band. (c) The Zak phases γ_n of the four bands are all quantized, with the second and third band, and thus also the induced band gap, being nontrivial. The coupling constants that generate the band structure in normalized frequencies are $\tilde{D}_1 = D_1 a^2/m = 0.1157\,\text{Nm/kg}$, $\tilde{D}_2 = 0.354\tilde{D}_1$, $\tilde{A}_1 = A_1 a^2/j = 0.0293\,\text{Nm/kg}$, $\tilde{A}_2 = 1.081\tilde{A}_1$, $\tilde{B}_1 = B_1 a^2/\sqrt{mj} = 0.0019\,\text{Nm/kg}$, and $\tilde{B}_2 = 6B_1$. Panel (a) and (b) adapted from [104] with permission. Panel (c) adapted from [137] (CC BY 4.0).

can be applied to evaluate the topological phase of individual bands. At the high-symmetry points at $k = 0$ and $k = \pi/a$, the eigenvectors can either be symmetric or antisymmetric upon action of $\hat{P}$.

3.3.2 Band Structure and Zak Phases

Panels (a) and (b) of Figure 3.4 show two exemplary band structures for the system of two SSH models in the absence and presence of chiral coupling. The chosen effective coupling constants resemble the behavior of the 3D chiral meta-material cells that will be designed in section 3.4. Without the chiral coupling, the longitudinal and rotational bands are independent. Each of the subsystems may be in its topologically trivial or nontrivial phase, depending on the ratio of the corresponding spring constants. It shall be noted once again, that the topological phase also depends on the unit cell convention shown in Figure 3.3, as explained in section 2.3.4. This will be considered later by setting the boundary conditions of the finite system.
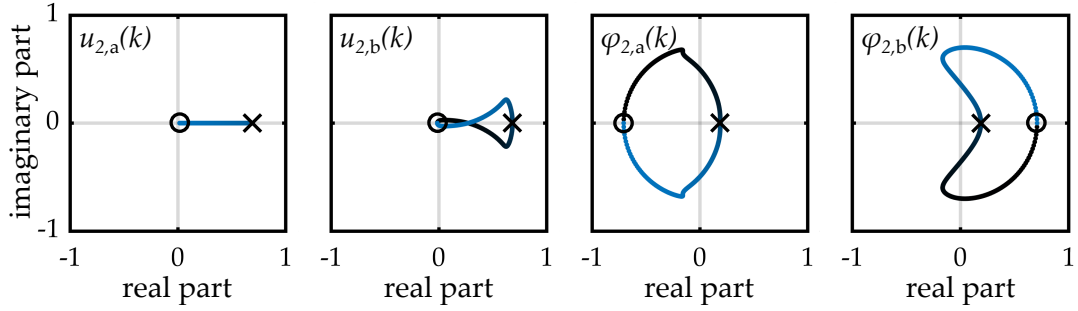
Figure 3.5: Contours of the four complex components of the second band's eigenvector. These components are used to calculate the Zak phase evolution across the first Brillouin zone from $k = -\pi/a$ (black) to $k = \pi/a$ (light blue). The first component is normalized to be real-valued. At $k = 0$ (black crosses), the longitudinal components dominate the band and the associated parity eigenvalue of the eigenvector is $p_0 = +1$. In contrast, the parity eigenvalue at $k = \pi/a$ (black circles) is $p_\pi = -1$, indicating a band inversion. There, the band has more rotational character. The second component winds closely around the origin, leading to a steep Zak phase evolution at the Brillouin zone boundaries, as show in Figure 3.4. Adapted from [137] (CC BY 4.0).

By switching on the chiral coupling, the longitudinal and rotational modes mix. As inherited from the uncoupled system, the first and third band are rotationally-dominated and the second and fourth band are longitudinally-dominated in the vicinity of $k=0$. Due to an avoided crossing, also called anticrossing, a band gap opens up between the lower and upper two bands. To check if this band gap is topologically nontrivial, we explicitly calculate the Zak phase evolution for the four bands via equation 2.32, as shown in Figure 3.4(c). Figure 3.5 exemplary shows the contours of the four complex components of the Bloch eigenvector that enter into the Zak phase calculation of the second band. Two of the four components show a winding around the origin as for vector $\mathbf{d}(k)$ for the SSH model. The nontriviality of the second band is indicated by a band inversion with parity values of $p_0 = +1$ and $p_\pi = -1$. We find that the Zak phases are quantized as long as the mirror symmetry is preserved via equal masses and moments of inertia. The topological index κ of the band gap, given by the Zak phases of the subset of the two bands below the gap, is determined via equation 2.35. Indeed, as the first band is trivial and the second band is nontrivial, the emerging band gap is topologically nontrivial with $\kappa = 1$. Hence, a finite version of the coupled SSH system can provide protected edge states.
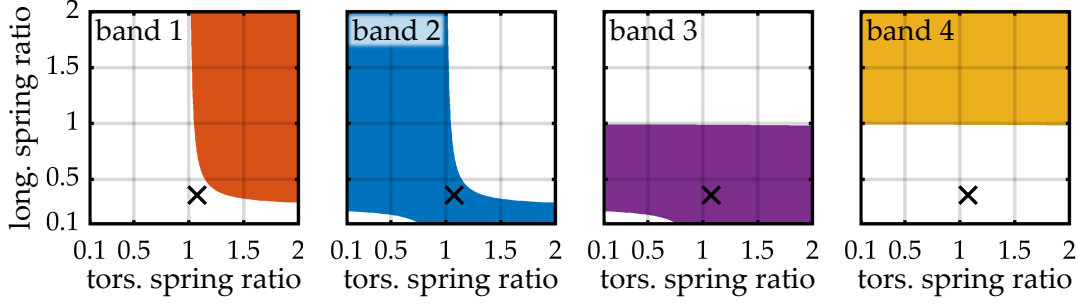
Figure 3.6: Topological phase diagrams of the four bands (cf. Fig. 3.4) for variation of the longitudinal and rotational spring constant ratios, D_2/D_1 and A_2/A_1, respectively. D_1 and A_1 are kept constant. The fourth band inherits its phase diagram mostly from the SSH mechanism and is nontrivial for $D_2 > D_1$. The other three bands are affected by the anticrossing, leading to complementary phase diagrams for the first two bands. This guarantees a nontrivial band gap over a large parameter regime. The crosses mark the effective coupling parameters used in Figure 3.4. Parts adapted from [104] with permission.

3.3.3 *Topological Phase Diagrams*

Before considering a finite system, it is worth to understand the mechanisms that determine the topological indices of the bands and the band gap. We sweep the longitudinal and rotational spring constants for a fixed chiral coupling to obtain a topological phase diagram for each band, as shown in Figure 3.6. Thereby, we use the band inversion along equation 2.34 as indicator to rapidly calculate the Zak phases of the individual bands for a large parameter set. As above, the topological index κ of the band gap itself is determined by the Zak phases of the two lower bands according to equation 2.35. Equal Zak phases of $\gamma_1 = \gamma_2 = 0$ or $\gamma_1 = \gamma_2 = \pi$ render the band gap trivial. For only one Zak phase equal to π, the band gap becomes topologically nontrivial.

The topological phase transition behavior turns out to be much more detailed as compared to the simple SSH model. The driving factor therefore is the anticrossing of the second and third band. As these bands do not cross anymore, they inherit each others parity values p_π at the Brillouin zone boundary. At the same time, the parity values p_π of the first and second band are related via the SSH mechanism, as both bands originally resulted from the acoustic and optical branch of the rotational SSH system. Combining both effects, either the first or the second band is nontrivial over a wide parameter range. This notable result means that this band gap has a topological index of $\kappa = 1$ and is always nontrivial in this range. Even a change of the unit cell convention would just flip which of the two lower bands is nontrivial. Thus, in strong contrast to the simple SSH model, the coupled SSH model is expected to exhibit protected edge states both when terminated

at sublattice site a or b. Only for very small longitudinal and rotational intercell coupling constants, the second and third band do not cross anymore and allow for a zero Zak phase of both lower bands, generating a trivial band gap.

3.3.4 Topologically Protected Edge Modes

Following the topological phase diagrams and the bulk-boundary correspondence, the emergence of protected edge states should be inevitable for the coupled SSH model. However, to verify the bulk-boundary correspondence for the simple SSH model in section 2.3.5, it was assumed that the springs of the finite system are attached to fixed ends on both sides. Having the application for a laser-beam scanner in mind (cf. Fig. 3.2), an open end of the metamaterial beam at the mirror's position is preferable. Only in that way the mirror is largely decoupled from its surrounding and can rotate freely.

Following this motivation, we consider a finite version of the chirally coupled SSH system, where the left end is fixed, e.g., to a piezoelectric transducer, and the right end is open with a larger mass m_r and a larger moment of inertia j_r due to the mirror. Then, the matrix equation for the real-space amplitudes read

$$\hat{Q}\mathbf{U}^{(z)} = \omega_z^2 \mathbf{U}^{(z)}, \text{ with}$$

$$\mathbf{U}^{(z)} = \left(\sqrt{m} u_{1,\mathrm{a}}^{(z)}, \sqrt{j} \varphi_{1,\mathrm{a}}^{(z)}, \sqrt{m} u_{1,\mathrm{b}}^{(z)} \sqrt{m} \varphi_{1,\mathrm{b}}^{(z)}, ..., \sqrt{m_\mathrm{r}} u_{N,\mathrm{a}}^{(z)}, \sqrt{j_\mathrm{r}} \varphi_{N,\mathrm{a}}^{(z)} \right)^T,$$

$$\hat{Q} = \begin{pmatrix} \tilde{D}_l & \tilde{B}_l & -\tilde{D}_1 & -\tilde{B}_1 & & 0 & 0 & 0 & 0 \\ \tilde{B}_l & \tilde{A}_l & -\tilde{B}_1 & -\tilde{A}_1 & \cdots & 0 & 0 & 0 & 0 \\ -\tilde{D}_1 & -\tilde{B}_1 & \tilde{D}_\mathrm{d} & \tilde{B}_\mathrm{d} & & 0 & 0 & 0 & 0 \\ -\tilde{B}_1 & -\tilde{A}_1 & \tilde{B}_\mathrm{d} & \tilde{A}_\mathrm{d} & & -\tilde{D}_1 & -\tilde{B}_1 & 0 & 0 \\ & \vdots & & \ddots & & -\tilde{B}_1 & -\tilde{A}_1 & 0 & 0 \\ 0 & 0 & 0 & -\tilde{D}_1 & -\tilde{B}_1 & \tilde{D}_\mathrm{d} & \tilde{B}_\mathrm{d} & -\tilde{D}_2 & -\tilde{B}_2 \\ 0 & 0 & 0 & -\tilde{B}_1 & -\tilde{A}_1 & \tilde{B}_\mathrm{d} & \tilde{A}_\mathrm{d} & -\tilde{B}_2 & -\tilde{A}_2 \\ 0 & 0 & 0 & 0 & 0 & -\tilde{D}_2 & -\tilde{B}_2 & \tilde{D}_\mathrm{r} & \tilde{B}_\mathrm{r} \\ 0 & 0 & 0 & 0 & 0 & -\tilde{B}_2 & -\tilde{A}_2 & \tilde{B}_\mathrm{r} & \tilde{A}_\mathrm{r} \end{pmatrix}. \tag{3.10}$$

Here, $\hat{Q}$ is the real space dynamical matrix, N the number of unit cells, and z the solution number. The rotational and longitudinal DOF in the vector $\mathbf{U}^{(z)}$ are arranged corresponding to their spatial order. The matrix elements on the block diagonal in the bulk (subscript d) and at the fixed left end (subscript l) are equal and given by

$$\tilde{D}_l = \tilde{D}_\mathrm{d} = \tilde{D}_1 + \tilde{D}_2, \quad \tilde{A}_l = \tilde{A}_\mathrm{d} = \tilde{A}_1 + \tilde{A}_2, \quad \text{and} \quad \tilde{B}_l = \tilde{B}_\mathrm{d} = \tilde{B}_1 + \tilde{B}_2. \tag{3.11}$$

At the right end, the coupling constants both on the block diagonals and block off-diagonals are scaled according to m_r and j_r, and the coupling to the next
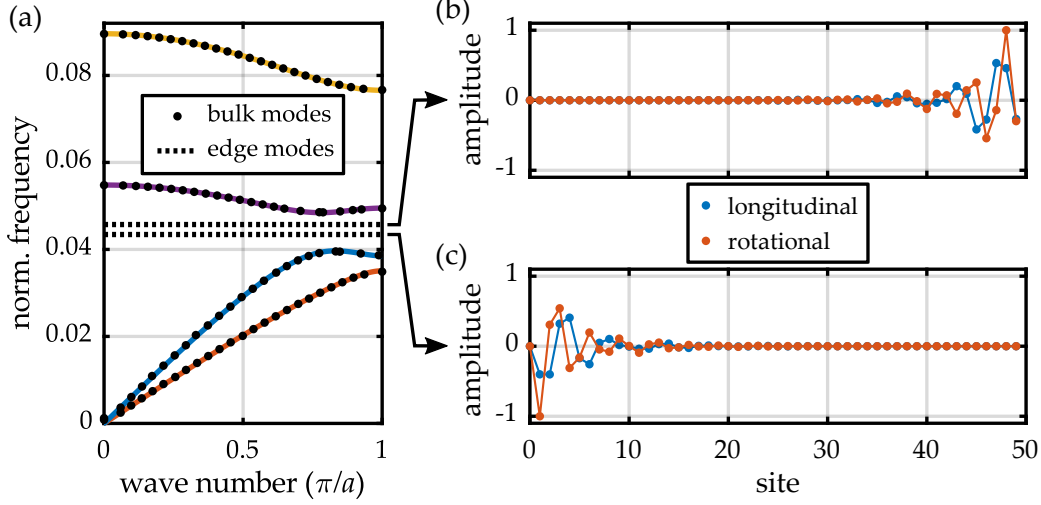
Figure 3.7: Finite coupled SSH system with fixed left end at site 0 and an open right end at site 49. To mimic an attached mirror, the right end has a larger mass and moment of inertia $m_r = 2m$ and $j_r = 2j$, respectively. (a) The eigenfrequencies of the system with their corresponding quasi wave numbers, calculated via spatial Fourier transformation, resemble the band structure of the infinite system. Two frequencies lie within the band gap, corresponding to localized modes at (b) the right end and (c) the left end. Adapted from [104] with permission.

element on the right is absent, such that

$$\tilde{D}_r = \frac{D_2 a^2}{m_r}, \quad \tilde{A}_r = \frac{A_2 a^2}{j_r}, \quad \text{and} \quad \tilde{B}_r = \frac{B_2 a^2}{\sqrt{m_r j_r}}. \tag{3.12}$$

Figure 3.7 shows the calculated eigenfrequencies of a such a finite system with 50 sites ($N = 25$). The system begins with a fixed sublattice site b (site 0) and ends with a loose sublattice site a (site 49), corresponding to the boundary terminations that will be chosen for the metamaterial beam in section 3.4 as well. Two edge modes with their frequencies inside the band gap emerge. The longitudinal and rotational amplitudes are clearly localized to the individual boundary. As inferred from the Zak phases and topological phase diagrams, the edge states emerge both for the termination by an a-site and by a b-site.

Edge Mode Robustness

The above results show that the edge modes seemingly emerge without further fine tuning when the bulk is equipped with the proper symmetries. After all, this is exactly the motivation for the design of a topological system. Still, the coupled SSH system is a topological crystalline insulator and the topological protection
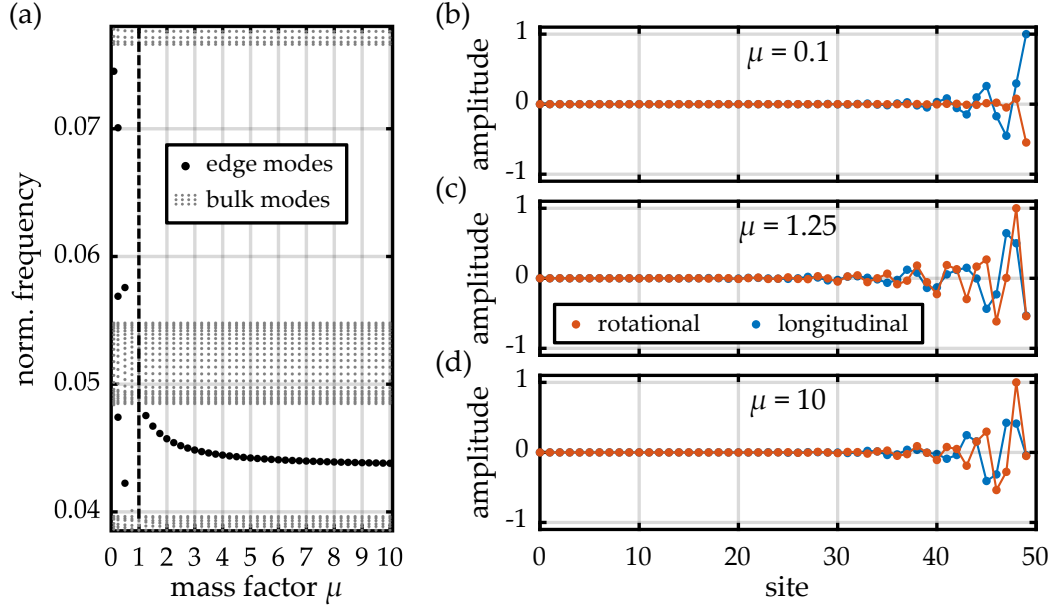
Figure 3.8: Robustness of the topologically protected edge modes under variation of the right end's mass and moment of inertia by a factor μ. (a) Eigenfrequencies of the bulk modes and detected edge modes in the spectral region of the two band gaps. For $\mu < 1$, the system has a quasi-open end. The bulk-boundary correspondence does not hold and localized modes appear only in the form of accidental defect modes, shown in (b). For a quasi-fixed end with $\mu > 1$, the edge mode is guaranteed and its frequency stabilizes toward the center of the band gap. (c) Approaching $\mu = 1$ (dashed black line), the amplitudes at the last site can be maximized in trade-off against a slightly increased penetration depth as compared to (d) for a larger factor μ.

relies on the preservation of spatial symmetries at the boundary, as indicated in section 2.2.5. A certain sensitivity of the edge modes toward different boundary conditions is already visible in Figure 3.7. For the two modes localized at the fixed end and at the open end with larger mass, the eigenfrequencies are not equal. This rises the question if there is a regime where the topological protection vanishes, such that the frequencies are pushed out of the band gap and localized modes are absent.

To study such effects, we change the boundary conditions in the finite system described by equation 3.10. The left boundary is switched from a fixed to an open end. Simultaneously, we vary the mass $m_{\mathrm{r}} = \mu m$ and moment of inertia $j_{\mathrm{r}} = \mu j$ of the last element on the right side by a factor μ. Figure 3.8 shows the effects on the eigenfrequencies and edge modes. The most significant change happens at the left boundary, where no edge state appears anymore. This indicates that the bulk-boundary correspondence is maximally violated. At the right boundary, the mass-factor sweep shows that the bulk-boundary correspondence does also not

hold true as long as $\mu < 1$. Localized defect modes might occur at the boundary, as shown in Figure 3.8(b). However, their eigenfrequencies are sensitive to small changes of the mass factor and can be easily pushed out of the band gap. For mass factors of $\mu > 1$, the situation is fundamentally different. There, the edge mode at the right boundary is guaranteed and its eigenfrequency converges toward the center of the first band gap when increasing μ. In this regime, the frequency and also the mode shape is remarkably stable. An 8-fold increase of the mass factor reduces the eigenfrequency by less than 9% and the effect on the rotational and longitudinal amplitudes is mostly limited to the last site, as shown in Figure 3.8(c) and (d). By increasing the mass, the boundary amplitudes are reduced. Apart from that, only the edge modes' penetration depth into the bulk changes slightly.

The observed effects are linked to the presence or absence of the mirror symmetry at the boundary. This can be verified by the real-space dynamical matrix $\hat{Q}$ in equation 3.10. In sections 2.3.1 and 3.3.1, it was shown that the presence of the mirror symmetry goes along with equal diagonal elements in the dynamical matrix. The block-diagonal elements at the fixed left end given in equation 3.11 are equal to the bulk block-diagonals, which perfectly preserves the spatial symmetry. For an open left end, however, the boundary coupling term, e.g., via $\tilde{D}_2$, vanishes:

$$\tilde{D}_l \to \tilde{D}_1, \quad \tilde{A}_l \to \tilde{A}_1, \quad \text{and} \quad \tilde{B}_l \to \tilde{B}_1. \tag{3.13}$$

Hence, the open end lifts the equivalence of the block-diagonal elements and thereby maximally violates the spatial symmetry, in the sense that the bulk-boundary correspondence breaks down and the topological protection vanishes completely.

The same holds true at the right boundary as long as the mass factor is small, i.e., $\mu \ll 1$. Then, the boundary element can move instantly and also resembles an open end. However, increasing the mass and moment of inertia at the right boundary can be understood as a transition from this symmetry-breaking open end to a symmetry-preserving fixed end. In the limit of an infinitely large mass factor μ, the longitudinal and rotational amplitude of the last site is effectively fixed to zero, re-establishing a system with fixed end and intact bulk-boundary correspondence. Figure 3.10(a) shows that this holds as long as $\mu > 1$. Hence, an open end with an additional mass can be understood as a quasi-fixed end.

Altogether, putting a larger mass to an open end of the coupled SSH system, e.g., for the metamaterial beam in the form of a mirror, is not only allowed but crucial to establish the bulk-boundary principle by approximating the required spatial symmetry. In this regime, the added mass can be chosen to optimize for the desired edge amplitudes and the level of spectral and spatial isolation of the topologically protected mode.

3.3.5 Dissipation Effects

The calculations on the coupled SSH model in above sections have not included dissipation effects. As argued in section 2.4, damping can be taken into account by using complex spring constants, or more generally, complex coupling constants. To mimic viscous material damping, the imaginary parts added to each coupling constant are simply a fixed fraction of the corresponding real part. A calculation along equation 2.52 reveals the same result for the generalized Zak phases of the individual bands. Hence, as for the simple SSH model, the topological features of the coupled SSH model do not change within this description, such that the above discussion does not have to be repeated for the case of nonzero damping. Only for more general damping mechanisms, represented by imaginary parts which do not scale equally for all coupling constants, the system can change significantly. This was investigated in the scope of the bachelor's thesis of Steven Kraus. The band structure, generalized Zak phases, and eigenvector contours are shown in appendix A.6 for an exemplary non-Hermitian version of the coupled SSH model. While such systems will not be further discussed in the course this work, it is notable that the quantization of the generalized Zak phases and thereby the distinction between the topological phases stays preserved for such a more general damping. In section 3.4.3, material damping will be included in the FEM calculations on the metamaterial beam to properly describe the resonant behavior of the protected edge modes.

3.4 CHIRAL METAMATERIAL BEAM

While the coupled Su-Schrieffer-Heeger model itself can be understood as an interesting toy model that realizes a specific topological class in mechanics, we will now use it as an effective model to design a device that converts longitudinal to rotational oscillations, i.e., the resonant laser-beam scanner already presented in Figure 3.2. This means that we have to translate the mass-spring model back to a suitable 3D structure. For the design, we model the structure's constituent material as a linear elastic Cauchy continuum with a given Young's modulus E and Poisson's ratio ν and use frequency-domain FEM calculations according to section 2.5. To decouple the discussion from scaling effects due to material and global size of the structure (via its lattice constant a), and for comparison with the coupled mass-spring model, we use the normalized frequencies $\tilde{f} = fa/c_1$. Here, c_1 is the phase velocity of a longitudinal wave in the bulk material, as introduced in equation 2.60. The corresponding frequencies of an actual structure with a given size and material can be inferred from the normalized ones when required for the experiments in chapter 5.
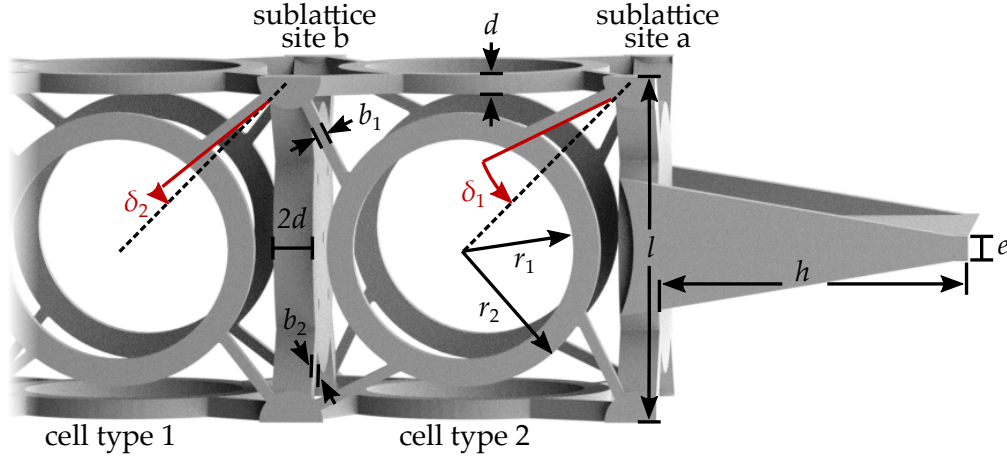
Figure 3.9: Close-up view of the metamaterial beam with two distinct chiral cube cell types and the mirror at the finite beam's end. The two vertical plates correspond to the two different sublattice sites a and b of the coupled mass-spring model (cf. Fig. 3.3). The beam is terminated with a cube cell of type 2. The geometrical dimensions in units of the cell size l are $d = 0.057l$, $b_1 = 0.032l$, $b_2 = 0.096l$, $r_1 = 0.319l$, $r_2 = 0.395l$, $h = 0.9l$, and $e = 0.090l$. The angles measured with respect to the corresponding cube cell face diagonal are $\delta_1 = 19.1°$ and $\delta_2 = 6.7°$ for the two distinct cells. The unit cell length (lattice constant) is $a = 2l$. The parameters are the result of the theoretical design process [104] and a marginal adjustment corresponding to the finally fabricated structures, shown in the next chapter. Adapted from [137] (CC BY 4.0).

The concept of a chiral cube cell with its push-to-twist mechanism and the construction of diatomic metamaterial beam have already been shown in Figures 3.1 and 3.3. From the coupled SSH model, we know that the chiral coupling together with a diatomic basis induces a band gap which is topologically nontrivial over a large parameter range, as long as an effective mirror symmetry is present. A finite version of the system then produces protected edge states in the regime of a quasi-fixed end. Apart from these restrictions, the metamaterial beam can be designed freely, e.g., to obtain a large band gap, to adjust the spatial and spectral isolation of the edge mode, and to optimize the enhancement of the edge mode's rotational amplitude with respect to the longitudinal excitation at the other end. In the following, I will first comment on the design aspects and results for the band structure and Zak phases. Therefore, an infinitely periodic version of the metamaterial beam is considered. Second, I will discuss the topologically protected twist edge resonances of a corresponding finite metamaterial beam. The relevant geometrical dimensions for both the bulk and boundary design of the final metamaterial beam are shown in Figure 3.9.

3.4.1 Infinitely Periodic Metamaterial Beam

As introduced in section 2.5.3, the band structure of an infinitely periodic metamaterial beam is obtained via FEM calculations of the unit cell with Floquet-Bloch periodic boundary conditions for the left and right face (cf. Fig. 3.3(a)). The metamaterial beam has to fulfill the symmetry criteria of the coupled SSH model and should exhibit a large band gap. Therefore, the underlying chiral cell geometry, the cell alternation principle, and also the shear-wave bands play an important role. In what follows, I will briefly explain these aspects.

Chiral Cell Geometry

The push-to-twist mechanism does not necessarily require the rather complex ring geometry as introduced by Tobias Frenzel *et al.* [15]. In fact, simpler chiral cube cell designs have been proposed in other publications [138, 139] and shown to exhibit even stronger chiral effects on elastic waves, i.e., in terms of their acoustical activity [132]. A uniaxial version of such a simple cube cell is constructed by connecting two plates by four beams, e.g., along the face diagonals, as shown in appendix A.7. However, such a structure is less interconnected and less compact as compared to the ring design. As a consequence, the band structure of a 1D-periodic stack of such cells contains a large amount of local resonances at low frequencies. As indicated in section 2.5.3, such local resonances can couple to the fundamental mixed longitudinal-rotational bands in an unintended and undefined way and thereby render the description in terms of an effective coupled SSH model and distinct topological phases invalid.

As a consequence, the metamaterial beam design is based on the ring-geometry cell. In general, the fundamental rotational and longitudinal bands can be reduced in frequency by increasing the size of the two solid plates or by decreasing the effective stiffness of the ring geometry. The masses and stiffness are adapted via the plate thickness d and beam thickness b_1 such that the frequencies of the lower longitudinal and rotational bands are as large as possible without reaching the spectral regime of higher-order backfoldings or local resonances.

Cell Alternation

The key design principle for the topological metamaterial beam is the alternation of neighboring cells to effectively implement the diatomic basis of the coupled SSH model. Thereby, the required symmetries have to be preserved. For a solid structure, the mirror symmetry of equation 3.8, established by equal masses and moments of inertia at the two sublattice sites, translates into an effective mirror symmetry of the mass distribution within the unit cell. Notably, the mirror symmetry acts on the effective 1D system, such that it is not necessarily lifted

due to the chirality of the stacked 3D cube cells. However, in contrast to the mass-spring model, the required change of the effective spring constants of a single-material structure can only be achieved by a change in its mass distribution. Thus, the aim is to induce a significant change in the effective spring constants of two distinct cells by a subtle change in their mass distribution. Here, the geometrical parameters of choice are the angles δ_1 and δ_2 (cf. Fig. 3.9), which largely influence both the effective longitudinal spring constants and the chiral coupling constants of the individual cells. The effective mirror symmetry of the mass distribution stays preserved for $\delta_1 \neq \delta_2$ in good approximation. In the final configuration, the angles δ_1 and δ_2 are chosen such that the band gap width above the second longitudinal-rotational band is maximized while keeping a pronounced push-to-twist coupling.

Shear-Wave Bands

As stated in section 3.1.1, the shear (transverse) modes are decoupled from the mixed longitudinal-torsional modes and hence are not immediately relevant in the design procedure. Still, for the desired spectral isolation of the protected edge modes, the metamaterial beam should have a band gap for all mode types. As the shear modes are also subject to the diatomic design, protected shear edge modes can arise due to the SSH mechanism. By design, both the acoustic and optical shear bands are pushed below the topologically nontrivial band gap. Potential shear edge modes thereby arise in the shear-mode band gap at much lower frequencies and do not interfere with the twist edge modes.

Effective Coupling Constants

After finalizing the design of the infinitely periodic chiral metamaterial beam, the system can be reduced back again to a coupled SSH model with structure-specific effective coupling constants. In section 3.3 these effective coupling constants have already been used (cf. Fig. 3.4). The normalized constants $\tilde{D}_{1(2)}$ and $\tilde{A}_{1(2)}$ of the two metamaterial cell types are determined in good approximation from additional band structure calculations. In these calculations, a periodic beam composed of only one of the two cell types is constrained once to longitudinal and once to lateral displacements only. This effectively decouples the longitudinal and torsional modes. The associated normalized effective coupling constants of each cell type can then be read off from the slopes of the fundamental bands emerging from the Brillouin zone center, e.g., corresponding to $\sqrt{D_1/m}$ and $\sqrt{A_1/j}$ for cell type 1. In this way, the effective masses m and effective moments of inertia j are automatically included in the calculations. The chiral coupling constants $\tilde{B}_{1(2)}$ can be inferred via equation 3.2 for the push-to-twist mechanism in the static case, as shown in Figure 3.1. The resulting effective coupling constants are
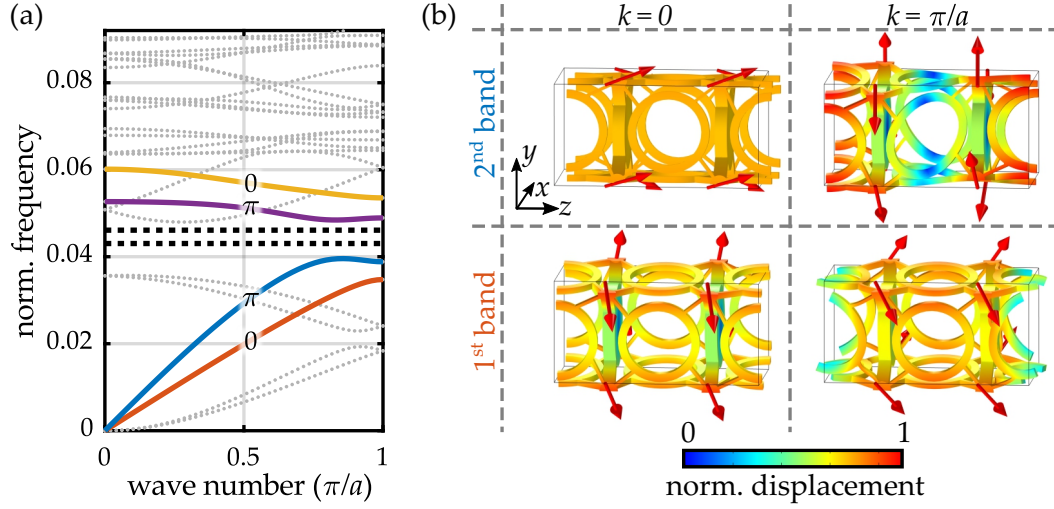
Figure 3.10: Band structure and eigenmodes of the designed metamaterial beam. (a) The four colored bands resemble the result of the coupled SSH model (cf. Fig. 3.4). The light-gray dotted bands are decoupled shear bands (lowest four bands), higher-order backfoldings, and local resonances (above the band gap). Only the upmost longitudinal band (yellow) is influenced by local resonances. The Zak phases of the two relevant bands (orange and blue) indicate a topologically nontrivial band gap with a relative band-gap width of 20%. The emerging edge modes' eigenfrequencies of a finite metamaterial beam with 7 cube cells (cf. Fig. 3.2) are indicated by the dashed black lines. (b) The Zak phases are determined via the parity eigenvalues of the Bloch displacement fields at $k = 0$ and π/a. Exemplary, the displacements at the two plates corresponding to the two sublattice sites are shown by red arrows. While the modes of the first band are symmetric with $p_0 = p_\pi = +1$, the second band shows a band inversion with $p_0 = +1$ and an antisymmetric mode shape at the Brillouin zone boundary, i.e., $p_\pi = -1$. This renders the band and the band gap above topologically nontrivial. Both the band inversion and the change from a longitudinal to rotational character along the second band agree with the results of the coupled SSH model (cf. Fig. 3.5). Adapted from [104] with permission.

additionally fine-tuned such that the band structure of the coupled SSH model is in best possible agreement with the one of the metamaterial beam.

3.4.2 Band Structure and Zak Phases

Figure 3.10(a) shows the calculated band structure for the metamaterial beam following the above design aspects. The Zak phases of the individual bands are inferred from the parity eigenvalues and the associated band inversion at the high-symmetry points in k-space, as discussed in section 2.3.3 and 3.3.1. The (anti-)symmetry under exchange of the two discrete sublattice sites transfers to

an effective (anti-)symmetry of the rotational and longitudinal displacements of the two plates, as shown in Figure 3.10(b). Both the band structure and Zak phases resemble the results of the coupled SSH mass-spring model when using the effective coupling parameters as listed below Figure 3.4. In accordance, the system has a 1D topologically nontrivial band gap that is expected to produce protected edge modes for a finite metamaterial beam. The relative band-gap width, i.e., the ratio of the band-gap width to its center frequency, is as large as 20%.

3.4.3 *Topologically Protected Twist Edge Resonance*

In Figure 3.10(a), the eigenfrequencies of two protected edge states are already indicated for a finite metamaterial beam design with 7 cells (cf. Fig. 3.2). To use the structure as a resonant mechanical laser-beam scanner, the edge mode localized to the mirror side has to exhibit a significant enhancement of the rotational (twist) amplitude with respect to the longitudinal excitation at the opposite side.

To verify this, we impose a time-harmonic longitudinal excitation with fixed amplitude in the frequency-domain FEM calculations and evaluate the resulting azimuthal displacement at the corners of the plate supporting the mirror. By sweeping the excitation frequency, we obtain the twist response spectrum across the band gap, as shown in Figure 3.11. To illustrate the effect of damping as introduced in section 2.5.2, the results are shown for three different complex dynamical Young's moduli $E = E'(1 + i/Q)$, corresponding to different quality factors Q. Indeed, the topologically protected twist mode is localized at the mirror end of the finite beam and can provide a conversion from longitudinal to rotational motion with a significant amplitude enhancement, if the quality factor is large enough. For a quality factor of $Q = 2000$, the amplitude enhancement is approximately 37.

Apart from the material quality factor, the twist enhancement also depends on the termination of the metamaterial beam and its length, i.e., the number of chiral cube cells it consists of. Additionally, so-called anchor losses can play a role. As explained in the following, this has been taken into account in the design process of the finite beam.

Beam Termination

The metamaterial beam's open end can be altered in regard to two main aspects. The first aspect is the variation of the mirror size and hence the effective mass and moment of inertia at the last site. As already indicated by the finite coupled SSH model (cf. Figure 3.8), an increase of this terminating mass primarily increases the spectral isolation of the edge resonance with respect to bulk modes at higher frequencies. However, at the same time the amplitudes at the last site decrease.
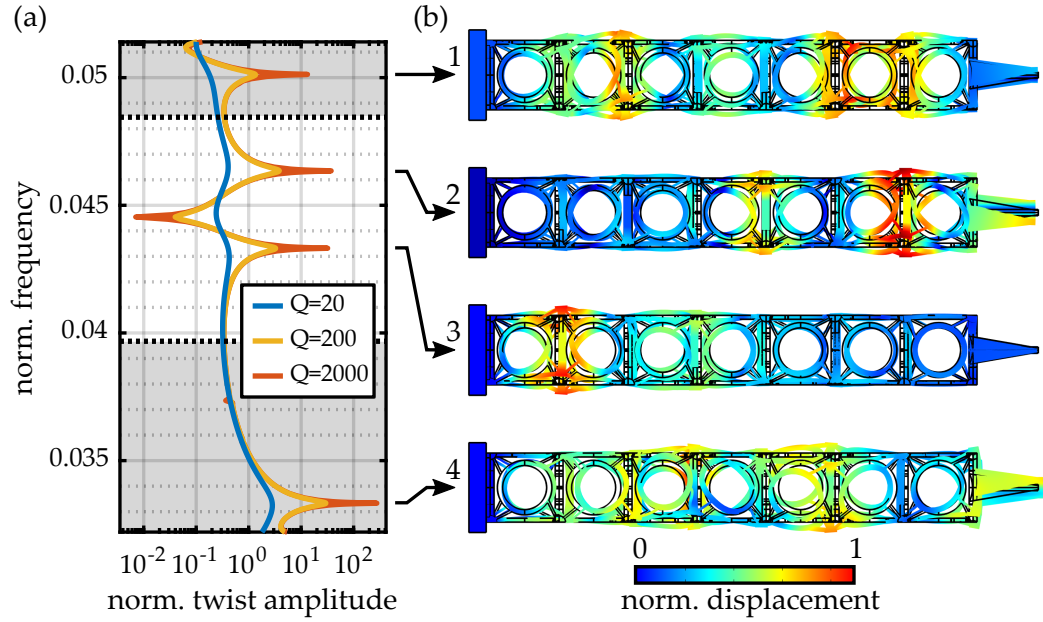
Figure 3.11: Twist resonances of the finite metamaterial beam. (a) Logarithmic twist response spectrum of the beam at frequencies around the band gap (white region). The calculated azimuthal displacements at the mirror plate's corners are normalized to the longitudinal excitation at the other end. Four resonances can be observed. (b) Resonances 1 and 4 are associated to bulk modes at the band edges. The other two are the protected edge modes. The displacement fields are individually scaled up for clarity. Resonance 2 is the desired mode with a large twist amplitude localized at the mirror position. Its azimuthal amplitude enhancement increases approximately linear with larger material quality factors Q, from around 0.37 for $Q = 20$, to 37 for $Q = 2000$.

For the chosen mirror size and its additional lateral support structure as shown in detail in Figure 3.9, the top-edge resonance shows a sufficient isolation from neighboring resonances while maintaining a significant rotational amplitude at the last site. If required, a lighter mirror providing a larger rotational amplitude could be chosen in exchange for less spectral isolation.

The second aspect is the cell type used to terminate the metamaterial beam. The investigations on the coupled SSH model in sections 3.3.1 and 3.3.4 have shown that edge modes emerge in both possible configurations. Still, FEM calculations reveal that the edge modes have a different characteristic. The termination with cell type 2 (cf. Fig. 3.9) results in an edge mode which is clearly dominated by a rotational amplitude. In contrast, a termination with cell type 1 leads to a longitudinally-dominated edge mode, as shown exemplary in Figure 3.12(b). There, the attached mirror does barely rotate. The different edge-mode characteristic can be understood in terms of the coupled SSH model. While the 1D band
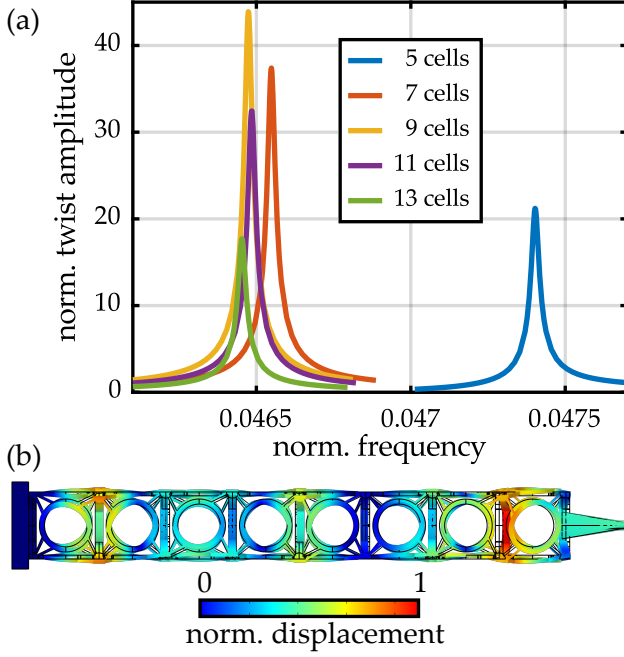
(a)

(b)

norm. displacement

Figure 3.12: (a) Twist resonances for different metamaterial beam lengths, assuming a quality factor of $Q = 2000$. For 5 cells, the resonance is shifted due to the residual influence of the boundary at the opposite side. The normalized twist amplitude is maximum for 9 cells and decreases for longer beams. (b) Edge mode for 8 cells. By the termination with cell type 1 instead of cell type 2, the edge mode at the right end is longitudinally-dominated and hence not suitable for a conversion to a rotational oscillation. Additionally, the mode is coupled to the edge mode at the opposite end.

gap is topologically nontrivial in any case, the topological phases of the two bands below the gap switches between the two configurations. As these bands a have different mode characteristic, it is plausible that also the associated edge mode characteristic is different.

Beam Length

The metamaterial beam length determines the coupling strength of the twist edge mode to the excitation at the opposite end and thereby also the maximally achievable rotational amplitude at the mirror plate. Within the damped harmonic oscillator model along equation 2.42, this is captured via the force coupling term $|\tilde{F}|$. This term is influenced by the spatial overlap of the edge mode profile with the longitudinal excitation. As shown in Figure 3.7(b), the longitudinal component of the edge mode and hence also the coupling strength changes from site to site. In Figure 3.12(a), the edge mode resonance curve for 7 cells is compared to results for beam lengths of 5 to 13 chiral cube cells. An exemplary material quality factor of $Q = 2000$ is chosen. Only uneven numbers of cells corresponding to terminations with cell type 2 are considered. As described above, undesired longitudinally-dominated edge modes emerge otherwise. For 5 cells, the obtained twist enhancement is approximately 21. Additionally, the mode's resonance frequency is strongly shifted as compared to longer metamaterial beams, indicating a significant influence of the fixed end on the opposite side. The largest enhancement of 44 is observed for 9 cells, followed by the already determined

enhancement of 37 for 7 cells. As a trade-off between a large twist enhancement factor and a compact design, the length of 7 cells has been preferred to 9 cells. For beams with more than 9 cells, the amplitude enhancement decreases again. This is a result of the nonzero material damping. It effectively decreases the coupling term $|\tilde{F}|$, as the longitudinal excitation gets more and more attenuated across the beam.

Anchor Losses

A remaining design aspect that has not been covered in the above considerations are anchor or support losses [140]. This damping mechanism cannot be captured via the material's quality factor. It describes the dissipation of energy via the anchoring of the structure to a bottom plate, which will be the piezoelectric transducer in the experiments. A precise quantitative calculation of anchor losses requires an exact modeling of the samples fixation to its anchoring [141] and is beyond the scope of this thesis. A simple approximation can be given by FEM calculations in which the metamaterial beam is placed on a large bottom plate, as shown in Figure 3.13. For a given eigenmode of the metamaterial beam, it is assumed that all the elastic energy that is located in the bottom plate will be dissipated [140]. Following equation 2.44, the anchor-loss quality factor Q_{anc} is hence defined as the ratio of the elastic energy stored within the metamaterial beam to the energy located in the bottom plate, i.e., $Q_{\mathrm{anc}} = 2\pi\, E_{\mathrm{beam}}/E_{\mathrm{bottom}}$. In the limit of an infinite beam length, the edge mode does not dissipate any energy to its anchoring at the opposite end, such that the anchor loss is zero. Hence, the anchor-loss quality factor of the edge resonance becomes infinitely large and will only be limited by other damping mechanisms, such as material damping. For a metamaterial beam consisting of 7 chiral cells, the approximate anchor-loss quality factor of the desired twist edge mode is as large as $Q_{anc} \approx 270\,000$. For comparison, Figure 3.13 also shows that the approximate anchor losses for the edge mode localized at the bottom plate result in a quality factor of only $Q_{anc} \approx 6400$. The overall quality factor that includes all damping mechanisms will hence be reduced according to equation 2.45. This underlines that the spatial isolation of the twist edge mode is indeed obligatory when working toward large quality factors.

3.4.4 Metamaterial Size

In the following chapters, I will show how to fabricate the designed metamaterial structure out of fused silica to obtain resonances with quality factors exceeding $Q = 2000$. To realize a converter for longitudinal to rotational motion or a proof-of-principle laser-beam scanner that operates at high frequency, it is crucial to

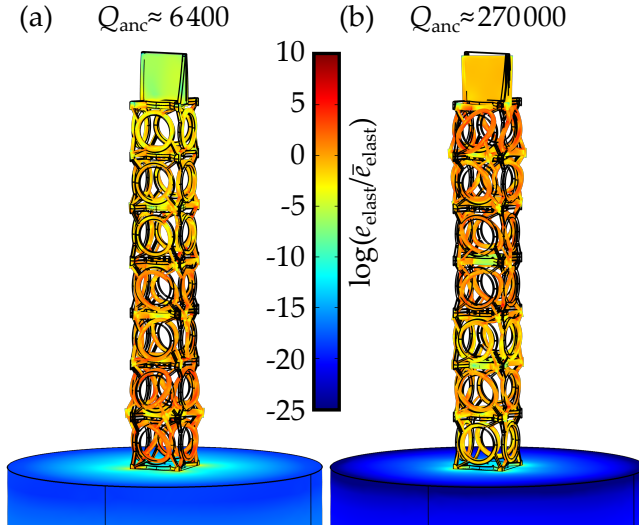(a) $Q_{anc} \approx 6400$ (b) $Q_{anc} \approx 270\,000$

Figure 3.13: Anchor losses for (a) the bottom-end and (b) the top-end edge mode. The color bar indicates the local logarithmic elastic energy density e_{elast} normalized to the average energy density $\bar{e}_{elast}$ within the structure. For the bottom-edge mode, a much larger fraction of the total energy is located in the bottom plate. Assuming dissipation of this fraction results in a much smaller anchor-loss quality factor of $Q_{anc} \approx 6400$ as compared to the spatially isolated top-edge mode with $Q_{anc} \approx 270000$.

scale the overall structure to an appropriate size. We take fused-silica glass as a highly stiff constituent material with a Young's modulus of $E_{silica} = 70.8\,\text{GPa}$ (see section 5.3.2), a mass density of $\rho_{silica} = 2.2\,\text{g/cm}^3$, and a Poisson's ratio of $\nu_{silica} = 0.17$ [142, 143]. Exemplary, we require an operation frequency of 270 kHz. With the normalized frequency $\tilde{f} \approx 0.046$ of the topologically protected twist edge resonance (cf. Fig. 3.11) and equation 2.60, we arrive at a metamaterial cube cell with a total size of $l = a/2 \approx 500\,\mu\text{m}$ and structure elements as small as 16 µm in width (cf. Fig. 3.9). This sets the requirements for the fabrication process in the next chapter.

3.5 SUMMARY

In this chapter, I have shown how a 1D topologically nontrivial band gap can be obtained for a mechanical metamaterial beam composed of 3D chiral cells. By the combination of topology and chirality it is thereby possible to introduce twist edge modes that can convert a small longitudinal excitation into a large rotational motion. With a mirror attached, the designed structure can operate as a resonant mechanical laser-beam scanner.

The topology of the metamaterial beam has first been investigated by mimicking the chiral cube cells with their push-to-twist coupling by a mass-spring model with longitudinal and rotational degrees of freedom. For alternating cube cells, the resulting diatomic mass-spring model corresponds to two coupled mechanical Su-Schrieffer-Heeger models. I have shown that the Zak phases of an infinitely periodic system are quantized in the presence of the formal bosonic time-reversal symmetry and an additional mirror symmetry with respect to the two sublattice sites. In contrast to the simple SSH model, the study of the topological phase

diagrams of the coupled SSH model has revealed that the emerging band gap is guaranteed to be topologically nontrivial over a large parameter range, independently of the chosen site of termination for a finite system. However, as the topological phases rely on a spatial symmetry, the bulk-boundary correspondence does not hold anymore if the boundary conditions do not preserve this symmetry. I have shown that the mirror symmetry is violated in the limit of an open end. The prerequisite for the appearance of topologically protected edge states is a fixed end, which can be also approximated by an open end with additional mass at the boundary site. Thus, I have drawn the conclusion, that adding a mirror to a chiral topological metamaterial beam has not a perturbing but a stabilizing effect on the emerging twist edge mode.

Apart from the requirements derived from the mass-spring model, the design objective for the bulk of the metamaterial beam has been the formation of a large 1D band gap for all mode types. I have shown that the band structure and Zak phases resemble the results of the mass-spring model when using the effective coupling constants of the designed metamaterial. As proof-of-principle, I have presented finite metamaterial beam with a mirror plate at its end. With the evidence of the emerging protected twist edge mode with its frequency inside of the band gap, I have reached the main goal of this chapter. The robustness of the edge mode offers freedom in the design when working toward a functional resonant laser-beam scanner. To arrive at a chiral topological metamaterial beam that operates with edge modes at frequencies as large as 270 kHz, an absolute metamaterial cell size of 500 μm is required. The optimal beam length, as well as the size and mass of the mirror depend on the required spatial and spectral isolation of the edge resonance. The provided amplitude enhancement and quality factor is determined by the coupling strength of the mode to the longitudinal excitation and the losses that will be present in a real world application, e.g., due to viscoelastic material damping and anchor losses. It should be noted that it is not within the scope of this work to design a final device with a rotational enhancement globally optimized with respect to all possible influences in an experiment. To do so, the contributions of anchor and material losses, air damping, and the mirror size and shape, would have to be fine-tuned in extensive parameter studies. Additionally, the metamaterial beam is not optimized toward an application as completely functional resonant laser beam-scanner. A structure design refined in this regard will be presented in chapter 6.

4

3D Glass Microstructures

In this chapter, I will show how to fabricate 3D microstructures out of glass via microcasting of a fused-silica nanocomposite. After a short introduction to existing fabrication techniques, I will give an overview of the process that was developed and used within the course of my work. In the subsequent sections, I will explain the individual process steps in detail. These steps include the usage of the fused-silica nanocomposite as base material, standard 3D laser printing to fabricate polymeric casts, and the novel helium-assisted microcasting approach, followed by a thermal treatment of the 3D microstructures. I will conclude the chapter by discussing the capability and limits of the presented fabrication process both for my work and beyond.

The fabrication approach has been described in short previously [137]. Martin Wegener proposed to utilize a glass nanocomposite. The idea for the helium-assisted microcasting approach has emerged from a discussion in our research group. Based on this, I have developed and optimized the process and fabricated the 3D glass microstructures.
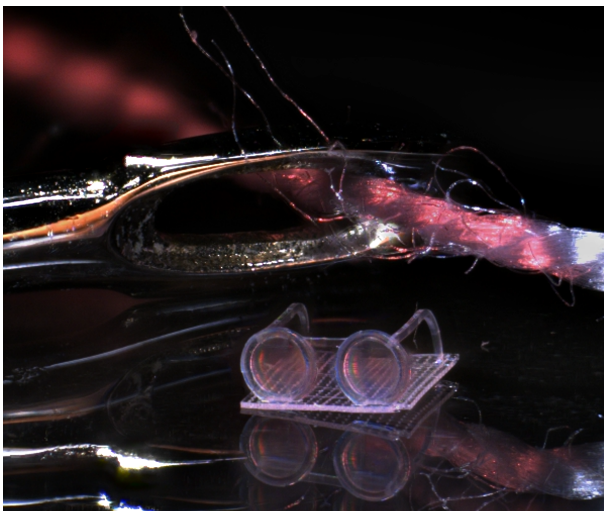

Figure 4.1: Micro-glasses made of glass. This exemplary structure in front of the eye of a needle was fabricated via the helium-assisted microcasting approach which has been developed within the course of my work.

4.1 Bringing Glass into Shape

A major goal in the course of my work has been to fabricate the chiral topological metamaterial beam designed in the last chapter. As pointed out already, the metamaterial must be fabricated out of a highly stiff material with small viscous material damping. Only in this way, it can provide the desired resonant conversion from a longitudinal to a rotational motion. Additionally, we require a structure with an overall cell size of 500 µm and elements as small as 16 µm to push its topological resonances to frequencies of around 270 kHz. Hence, we are looking for a fabrication technique that can provide complex 3D structures with feature sizes in the micrometer regime.

The probably most capable technique for this purpose is 3D laser lithography, also called direct laser writing or two-photon 3D laser printing [144, 145]. However, to this date, the technique is only standardized and highly optimized for the fabrication of polymeric structures. As I will show in chapter 5, polymer has a relatively low stiffness and exhibits pronounced material damping. Therefore, we are in need of an alternative fabrication process that is suitable for the fabrication of 3D structures of more promising constituent materials, such as metals, ceramics, or glasses. Materials of these three classes usually have a high stiffness. Especially metals and glasses are known for their outstanding mechanical properties. Additionally, these materials are also interesting in terms of their electrical, thermal, or chemical properties. As a consequence, 3D (micro-)fabrication of all these materials is an active field of research [146–148]. Thereby, the focus is on additive manufacturing, as techniques like graving or milling are commonly more limited with respect to the 3D shapes and feature sizes that can be achieved [149].

One approach is the direct deposition of the pure material, e.g., via fused filament fabrication or selective melting and sintering of powder. While this is in principle possible for metals and glasses, the quality, resolution, and achievable shapes for the resulting structures are limited [148, 150]. Thus, a more promising way to go are indirect deposition techniques. Thereby, it is the aim to formulate inks, sol-gel mixtures, or nanocomposites, also called slurries, that contain a large amount of the desired material, or precursors thereof. Such slurries facilitate the material deposition and are formulated to be suitable for various additive manufacturing techniques. In particular, it is possible to formulate photoresists which can be used for stereolithography, digital light processing, and also 3D laser printing. By these techniques, 3D micro- and nanostructures were successfully fabricated out of metal [151, 152], ceramics [153–155], and glass [156–160] in recent years.

A major downside of the indirect deposition approach is the thermal post-treatment of the resulting structures. It is required to transform the slurry into the desired target material. Depending on the material and slurry, the thermal treatment serves to evaporate solvents, remove binder materials, and pyrolyze or sinter the sample to a solid structure. Due to the loss and consolidation of material within the process, the 3D structures shrink and thus are prone to develop deformations or even cracks. While the latter can be reduced by properly adjusting the slurry composition and the temperature treatment, a certain overall shrinkage of the structure is unavoidable. As it directly determines the percentage of shrinkage, the fraction of the target material, also called the solid load of the slurry, should be as large as possible, while keeping the slurry applicable.

In the course of my work, we use a highly developed commercial glass slurry that was shown to be suitable for the fabrication of 3D structures via carving, molding, and micro-stereolithography [161–163]. A decisive feature of the slurry is that the fabricated structures maintain their quality during thermal treatment and their shrinkage is moderate. Notably, even two-photon 3D laser printing was shown with a similar slurry [159]. However, in the current state it is not clear if this technique can produce a complex high-quality 3D structure such as the chiral topological metamaterial beam presented in the last chapter. In contrast to 3D glass microstructures realized so far, the metamaterial beam unifies several critical geometrical features. It has small structure elements, which are contrasted by a more than two orders of magnitude larger overall size, and its function depends on subtle structural differences. Additionally, the delicate metamaterial beam has overhanging parts and a high aspect ratio in terms of its footprint and height. In fact, even the fabrication of polymeric chiral cube cells via two-photon 3D laser printing is not trivial and requires a sophisticated printing strategy [15, 17].

In what follows, I will show how to use the commercial glass slurry and two-photon 3D laser printing of polymer microstructures to arrive at complex 3D glass microstructures. To bring these two aspects together, I have developed a novel fabrication process, the so-called helium-assisted microcasting. Figure 4.2 shows a schematic overview of the complete fabrication procedure. In the first step, a polymeric shell of the target 3D microstructure is printed via two-photon 3D laser printing. This shell serves as a cast for the glass slurry. In the second step, the cast is evacuated, filled with helium gas and a droplet of glass slurry is applied to an inlet of the otherwise sealed cast. Subsequently, the sample is exposed to air under ambient conditions. As the helium escapes through the shell, the viscous glass slurry gets sucked throughout the whole microcast. After the filling process is completed, the slurry is cured with ultraviolet (UV) light. Finally, both the polymer cast and the polymeric binder in the slurry are thermally debound in a tube furnace and the sample is sintered to a solid 3D glass structure at temperatures up to $1225^\circ C$.
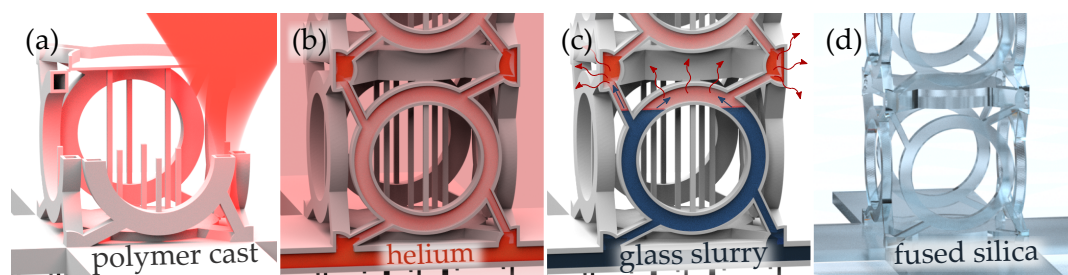
Figure 4.2: Schematic process steps for the fabrication of 3D glass microstructures via helium-assisted microcasting. (a) A polymeric cast for the targeted structure is fabricated by two-photon 3D laser printing. (b) The cast is evacuated and filled with helium. After applying a droplet of glass slurry to an inlet, the structure is exposed to ambient conditions again. (c) As the helium escapes through the shell, the slurry is sucked into the cast. When the cast is completely filled, the slurry is UV-cured. (d) By thermal treatment with temperatures up to 1225°C, the polymer cast and the polymeric binder are thermally debound and the shaped glass slurry is sintered to a solid 3D glass microstructure. Adapted from [137] (CC BY 4.0).

4.2 3D LASER PRINTING

The process starts by fabricating polymeric microcasts of the targeted 3D structure. As already motivated above, we use two-photon 3D laser printing for this purpose. Thereby, solid polymer structures are 3D printed by focusing a femtosecond-pulsed laser beam into a liquid and optically transparent photoresist [144, 145, 164]. The photoresist usually consists of a monomer mixture and a photoinitiator, i.e., photosensitive molecules. In the focus of the laser beam, the photoinitiator molecules are excited via two-photon absorption and form radicals. These radicals initiate a polymerization and cross-linking of the monomers, leading to the formation of solid polymer networks. The volume element that is solidified using only one focus position is commonly called the voxel (volume pixel). By scanning the laser focus through the photoresist, almost arbitrary 3D polymer structures can be obtained.

4.2.1 Setup

In this work, the commercial 3D-laser-printing system Photonic Professional GT (Nanoscribe GmbH) is used. As shown in Figure 4.3, the system is based on a microscope in inverted operation. It uses a 80 fs-pulsed frequency-doubled erbium-doped fiber laser with a wavelength of 780 nm. The photoresist is applied to a glass substrate which is fixed to a sample holder. The microscope's objective lens focuses the laser beam inside the photoresist. By two galvanometer mirrors, the
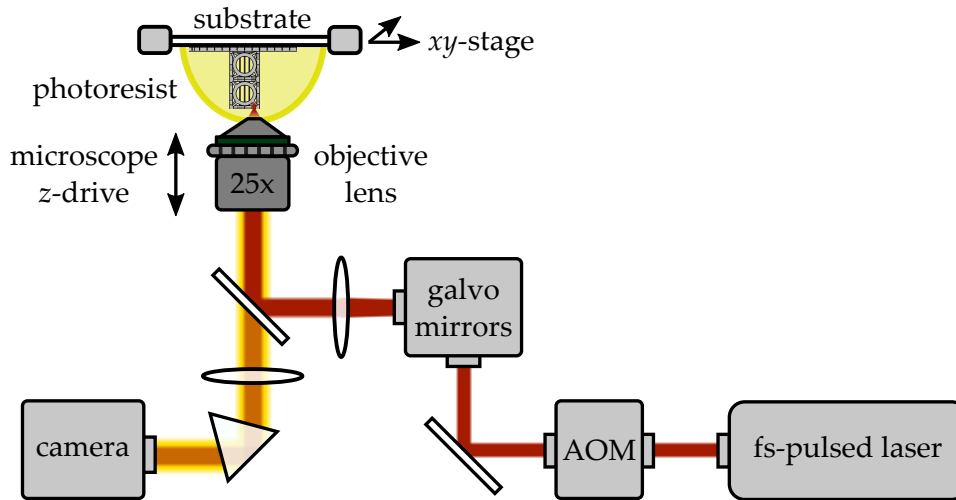
Figure 4.3: Schematic setup of a two-photon 3D laser printer. In the inverse microscope configuration, the beam of a femtosecond-pulsed laser is focused into a photoresist by a microscope objective lens. Via two galvanometer (galvo) mirrors, the laser focus can be scanned rapidly in lateral direction. Axial displacements are accomplished by the microscope's z-drive. Large lateral shifts are possible by moving the sample holder via an xy-stage. The laser power is controlled by an acousto-optic modulator (AOM). The printing process can be observed in-situ in transmission- or reflection-illumination via an installed camera.

laser beam can be scanned rapidly within planes parallel to the substrate. In the axial direction, the laser focus position is varied by the z-drive of the microscope. For large shifts in the substrate plane, the sample holder can additionally be moved via an xy-stage. To control the laser power and thus the local exposure of the photoresist, the laser beam can be deflected by an acousto-optic modulator.

The choice of photoresist and objective lens mostly depends on the overall dimensions, the minimum feature size, and the surface quality of the aimed-at 3D structure. Given the 3D structure size has been targeted in the beginning of this section with an overall size of several millimeters and structure elements of a few micrometers, the usage of the commercial photoresist IP-S (Nanoscribe) together with a 25× microscope objective lens (numerical aperture 0.8, Zeiss) suits best. The structures are printed in dip-in mode, meaning that the objective lens is dipped directly into the photoresist [165]. This lifts height restrictions in the printing process and allows for the fabrication of structures with an overall height of several millimeters. The structures are printed onto indium tin oxide-coated soda-lime glass substrates (Nanoscribe). To promote adhesion of the printed polymer, the substrates are silanized in a vacuum desiccator using 3-(trimethoxysilyl)propyl methacrylate prior to use.

4.2.2 *Two-Photon Absorption and the Proximity Effect*

Before discussing the final microcast design and the printing parameters, I will shortly discuss a mechanism that limits the capabilities of two-photon 3D laser printing, namely the proximity effect [166].

In principle, the achievable resolution and feature size in 3D laser printing is governed by the two-photon absorption process [145]. Via two-photon absorption, the exposure dose required to locally polymerize the photoresist depends quadratically on the intensity of the laser light. In can be shown conceptually that only such a nonlinearity allows to laser-print truly 3D structures [167, 168]. In practice, the process is much more complicated and involves not only the accumulated dose as a result of the scanned laser focus but also diffusion processes within the photoresist [169]. The main antagonists of the generated photoinitiator radicals are oxygen molecules. As known from the Schwarzschild effect, oxygen quenches excited photoinitiator molecules [170]. Also, it inhibits the polymerization reaction [166]. To a certain degree, this is a welcome phenomena in 3D laser printing, as it confines the solidified voxel upon exposure to a finite size. However, as the laser is scanned rapidly through the photoresist, oxygen can be locally depleted, such that undesired polymerization can occur in the vicinity of the laser focus. This mechanism is called proximity effect. By this effect, structural elements of the printed 3D structure which are close to each other, i.e., for the photoresist IP-S in the range of a few micrometers, might not be printed as designed. This is of tremendous importance for the 3D laser printing in this work. The overall fabrication process depends crucially on shell-like structures with small channels. These channels are required to be free from any polymerized material. Otherwise, the helium-assisted infilling procedure will not work. To reduce the proximity effect and avoid structural defects, it is advisable to minimize the dose that is deposited by the laser, both locally and globally. This is one of the main objectives for the microcast design and printing process presented in the following section.

4.2.3 *Microcast Design*

Figure 4.4 shows close-up views of the 3D printed polymeric microcast for the targeted 3D chiral metamaterial beam. An overview of the structure with the additional elements required for the cast process can be found in Figure 4.8(a). To end up with a glass cube cell size of around $l = 500\,\mu\text{m}$, the shrinkage of the slurry, as determined in section 4.5, has to be precompensated. Therefore, the cube cell size of the initial cast has to be as large as $667\,\mu\text{m}$. The microcast is designed via the computer-aided design (CAD) module of COMSOL Multiphysics and subsequently imported as STL-files to the software Describe (Nanoscribe). There,
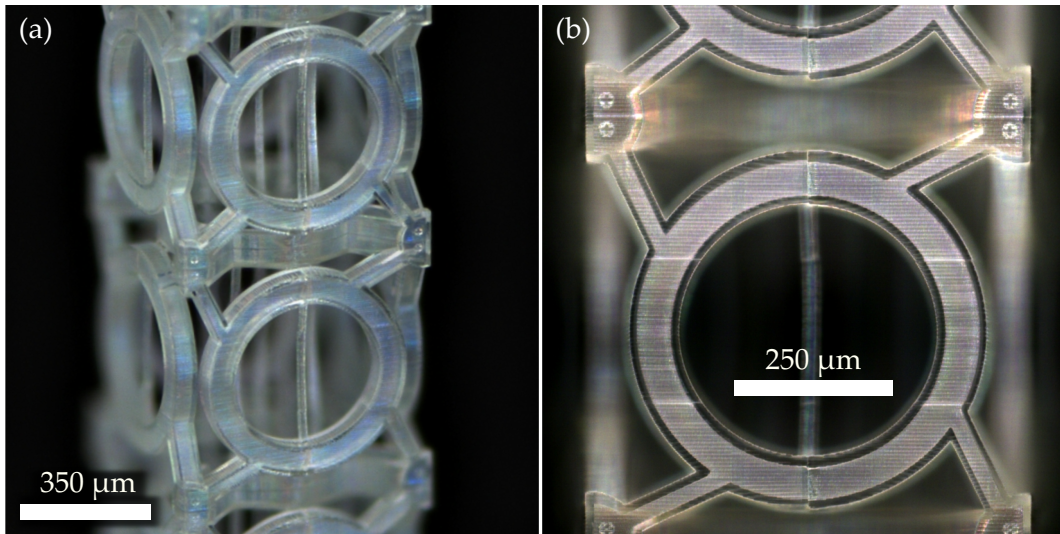
Figure 4.4: Optical microscopy images of 3D laser printed polymer microcast. (a) The shells for the individual chiral cube cells of the metamaterial beam have additional support posts, e.g., within the rings and in the interior of the cell. Thereby, the cast is stabilized. (b) The shell thickness at the thin beams is as small as possible to reduce the proximity effect and avoid blocked channels. For the measurements, small marker crosses are added at the cubes' corners.

the machine code of the actual printing process is generated according to the desired 3D structure and printing parameters. In the simplest case, the microcast would just be a polymer block with channels corresponding to the targeted 3D structure. To minimize the dose deposited in the photoresist and the proximity effect, the cast is reduced to a thin shell only. The shell's thickness is 11 μm, which is just enough to guarantee that the cast is completely sealed except for the glass slurry inlet. Support posts with a footprint of $19\times19\,\mu m^2$ are added to stabilize the fragile structure. Additionally, the posts help to fix overhanging elements during the printing process, such as parts of the rings and the thick horizontal plates. For the experiments in chapter 5, small marker crosses are added at the corners of each cube cell.

The finest features and also the most critical elements of the structure are the slender beams which connect the rings to the edges of the corresponding cube cell, as shown in Figure 4.4(b). As explained in the previous chapter, the angles of these beams are responsible for the required subtle difference between the two distinct chiral cube cells. Thereby, also the emergence of the 1D topological band gap and the protected edge states depends on these structural features. Additionally, the width of the beams determines the effective stiffness of the cells. At the same time, the interior of the shell is extremely prone to undesired polymerization, as the distance between adjacent polymer walls is the smallest at these positions. As a consequence, the thickness of the shell at the beams is further reduced to 7.7 μm.

73

Voxel Correction

To achieve a good agreement between the designed and printed 3D structure, the size of the printing voxel has to be taken into account. For the printing configuration and standard printing parameters, the voxel size is expected to be around 1.5 µm in axial direction and around 0.5 µm in lateral direction. By simply scanning the laser across regions that should be polymerized, the finite voxel size will lead to a microcast shell which is slightly thicker as designed. In turn, the final glass structure will be too thin. Thereby, the discrepancy between design and result depends on the orientation and shape of the individual element to be printed. Thus, this effect has to be compensated by correcting the structure design according to the observed geometrical dimensions of previously fabricated samples. Especially for the slender beams with their distinct angles, the nominal channel width has to be different in order to produce beams of the same size in the end.

4.2.4 *Printing Parameters*

In addition to the slender design of the microcast shell, the proximity effect has to be further reduced by adjusting the printing parameters. The most important parameters in the conventional printing mode are the laser power, the scan speed, the lateral hatching distance of neighboring scan lines within a plane, and the axial slicing distance between neighboring scanned planes. Due to the axial elongation of the voxel, the slicing distance is usually larger as the hatching distance. To obtain polymer structures with smooth surfaces and strong cross-linking, the printing parameters are commonly chosen such that the hatching and slicing distance are well below the voxel size and the deposited dose is well above the minimum dose required to solidify the photoresist, i.e., the polymerization threshold. However, this is equivalent to a certain overexposure of the photoresist and thus amplifies the proximity effect. As a consequence, the microcasts are fabricated with a large hatching and slicing distance of 0.5 µm and 1.5 µm, respectively. Furthermore, the laser power at the back-focal plane of the microscope objective lens is set to 36.25 mW. For the chosen scan speed of 14 cm/s, this is just slightly above the polymerization threshold. To improve the bonding between neighboring polymer layers and to speed up the printing, the hatching direction is alternated within the individual planes and rotated by 90° from layer to layer. With the above printing parameters, a complete cast including additional elements for the helium-assisted microcasting can be fabricated within five hours. Figure 4.5 shows scanning-electron micrographs of the printed microcast. It verifies that the printing parameters have been pushed to their extremes, such that the exposure dose is just large enough to generate a solid shell but leaves isolated voxel lines at the surface.
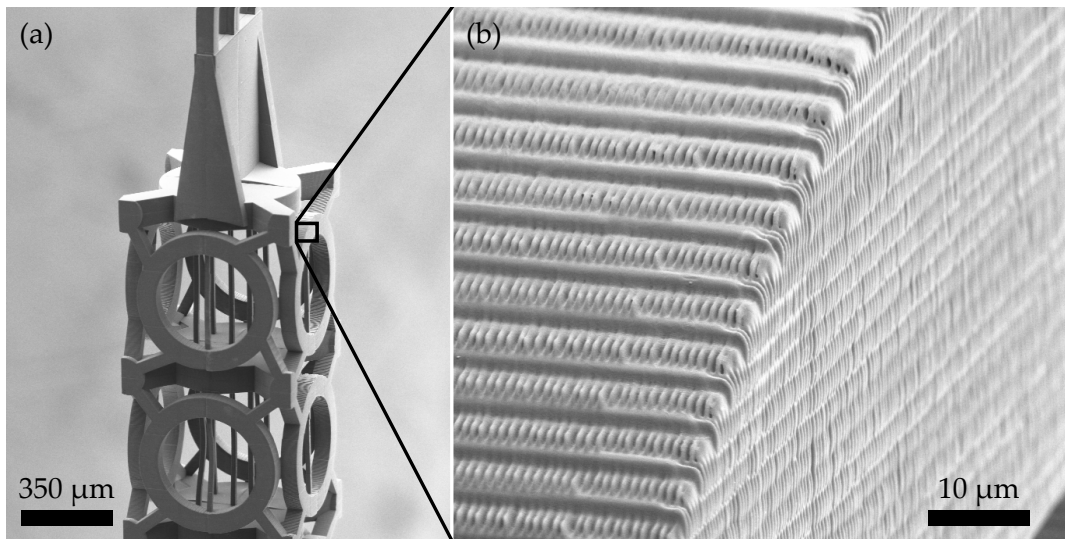
Figure 4.5: Scanning electron microscope (SEM) images of the 3D laser printed polymer microcast. (a) Perspective view onto the two upmost cube cells and the mirror plate's shell. (b) Close-up view of the shell. Due to the large hatching and slicing distances and the low laser power, the individual voxel lines are visible on the shell's surface. The surface quality of the final 3D glass microstructure is essentially limited by this roughness of the cast (cf. Fig. 4.9).

During the development process, which is described in the next section, the polymer structures shrink by a few percent due to the low exposure dose and the associated low cross-linking. This becomes relevant, if the laser power and thus the cross-linking is inhomogeneous across the scanned field. Then, the resulting inhomogeneous shrinkage can distort the microcast. To minimize such inhomogeneities and distortions, the scan field is adjusted with respect to the objective lens aperture via an offset of the galvanometer mirrors. For the chosen objective lens, the available scan field has a size of around $400 \times 400 \, \mu m^2$. As the lateral sample size exceeds this footprint, the structure is separated into blocks of $347 \times 347 \, \mu m^2$ which get stiched together during the printing process. The height of these blocks is $227 \, \mu m$, which is a third of the cube cell size and well below the objective lens' free working distance of $380 \, \mu m$. The block positions are chosen such that the critical structural elements, i.e., the channels for the slender beams, are free of stitching edges.

4.2.5 Sample Development

After the printing process is complete, the remaining liquid photoresist is removed from the cross-linked 3D polymer structure in a development step. For this purpose, the samples are immersed in a solvent. Due to the high aspect ratio of

the microcast channels, it has to be taken care of a sufficient development time. The samples are developed for two hours in propylene glycol methyl ether acetate ($\geq$ 99%, Carl Roth) and for another 24 hours in acetone (ROTISOLV, $\geq$ 99.9%, Carl Roth). Afterward, the samples are dried in air. High-purity acetone was used to avoid the formation of any residuals in microcast channels during the evaporation of the solvent. To promote the development process, the microcasts can be immersed in upright position, with the slurry inlet hole at the bottom end. Stirring and gentle heating can further speed up the dissolution of the liquid photoresist.

In the course of this work, the samples were examined under an optical microscope during the evaporation of the solvent. Thereby, the quality and functionality of the printed cast was observed for further optimization. Bubbles which form in the cast's interior indicate holes in the shell. On the other hand, hindered evaporation indicates blocked channels, e.g., due to undesired polymer membranes resulting from a too pronounced proximity effect. Both observations disqualify a sample for further usage in the helium-assisted microcasting process.

4.3   Fused-Silica Nanocomposite

For the fabrication of the 3D glass structures, the two commercial fused-silica glass slurries (L40 and L50, Glassomer) are used. The main results [137] shown in chapter 5 are based on structures using Glassomer L40. Glassomer L50 was first commercially available in the final phase of my work and has only been used for the structures and experiments shown in chapter 6. The use of glass slurry L50 is advantageous, as it has a lower viscosity and a higher solid load as compared to L40. Thus, L50 further facilitates the helium-assisted infilling process and reduces shrinkage of the fabricated structures. Both slurries are expected to provide comparable structures in terms of the mechanical properties of the resulting glass. The formulation of prototype versions of the commercial products can be found in references [161] and [162]. The four main ingredients of the slurries are the monomer hydroxyethylmethacrylate, the solvent phenoxyethanol, a diacrylate as cross linker, and amorphous silica nanoparticles. Additionally, a photoinitiator is added to obtain a UV-curable mixture. The percentages of the individual ingredients are optimized to obtain a free-flowing slurry with high solid load. The dynamic viscosity of slurry is L40 around 2 Pa s [171], which is perceived as viscous as honey or syrup. The thermal treatment of UV-cured slurry is described in section 4.5. By measuring the weight of a droplet of slurry before and after thermal debinding, solid loads of $54.9 \pm 0.5\%$ and $66.5 \pm 0.4\%$ for slurry L40 and L50, respectively, are obtained. Figure 4.6 shows an SEM image of a droplet of the thermally debound slurry L40. The silica nanoparticles have a diameter of approximately 100 nm.
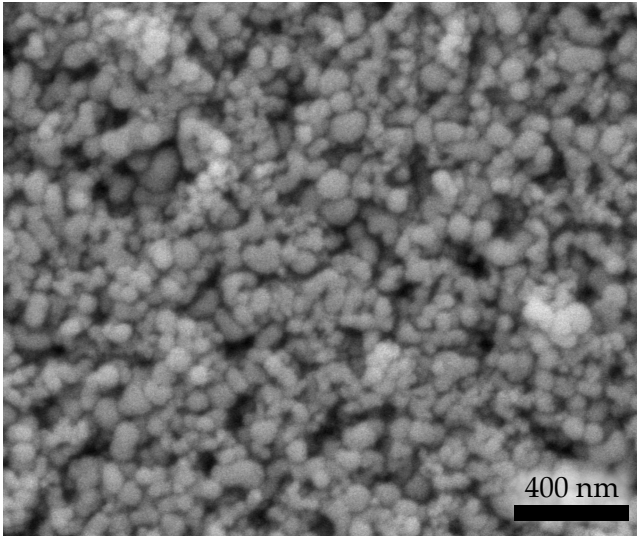
Figure 4.6: Scanning electron micrograph of the surface of droplet of glass slurry L40 after thermal debinding at 600°C. Only the amorphous silica nanoparticles are left. They have a diameter of around 100 nm and are packed densely. For Glassomer L50, a larger particle size is observed.

400 nm

4.4 HELIUM-ASSISTED MICROCASTING

For well-defined 3D glass microstructures, it is not an option to simply pour slurry into a patterned mold or over a 3D laser printed polymer structure, as it was done previously to fabricate optical lens arrays and glass microfluidic channels [161]. Thus, the key challenge is to fill the viscous glass slurry into the 3D microcasts in a controlled and reliable manner. To do so, I developed the helium-assisted microcasting process. In this process, we make use of the different permeability of polymer membranes for air and helium gas [172]. For air and carbon dioxide, this was used previously in experiments on mechanical metamaterials with negative effective compressibility [173].

In a first step, the developed microcast samples are put into a small plastic box which is sealed with parafilm. A small hole is pierced into the film. Then, the samples are evacuated in a desiccator using a membrane pump. To remove humidity, the samples can be kept in the evacuated desiccator for half an hour. Subsequently, the desiccator is flushed with helium gas (ALPHAGAZ 1 He, 99.999%, Air Liquide). After repeating the evacuation and helium flushing three times, the sample box is taken out of the desiccator and put under a binocular microscope. To maintain the helium environment, the sample box is flushed with a constant flow of helium gas (around 0.5 l/min) via an inlet nozzle. The setup is shown in Figure 4.7. The glass slurry is filled into a syringe with a 0.5×20 mm cannula. While observed under the binocular microscope, the cannula is pierced through the parafilm and a droplet of slurry is applied to the inlet funnel of the microcast, as shown in Figure 4.8(a). Thereby, the microcast's inlet is sealed by the slurry. Afterward, the sample box is immediately opened such that the cast is exposed to air. The helium starts to diffuse through the cast's polymer shell and the created vacuum sucks the glass slurry into the channels, as shown in

Figure 4.7: Setup for the helium-assisted microcasting. The microcasts are kept in the sample box which is flushed with helium via an inlet nozzle. Via a syringe, slurry droplets are applied to the microcasts. The process is observed with a binocular microscope and conducted under yellow-light illumination to avoid curing of the glass slurry.
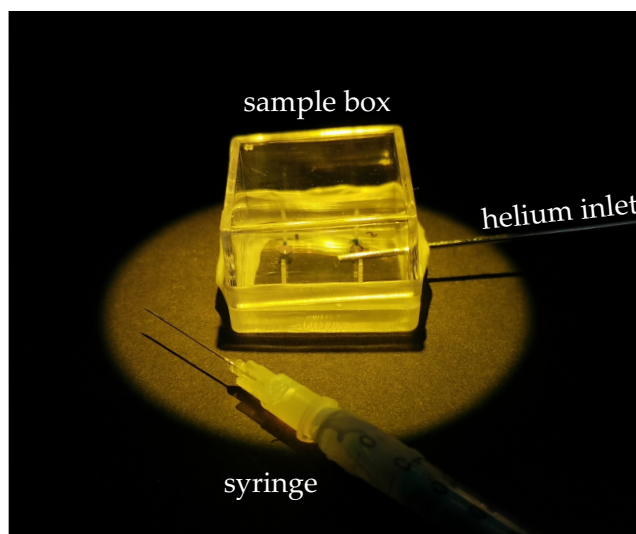
panels (b) to (d) of Figure 4.8. After around half an hour, the microcast is filled completely and the glass slurry can be UV-cured. Therefore, a light-emitting diode (WEPUV3-S2, Winger Electronics) with a peak emission at a wavelength of 400 nm and a radiometric power of around 1.2 W is used. The samples are placed in a distance of less than 5 cm to the LED.

As verified by the 3D metamaterial beam structure, the helium-assisted microcasting process works for complex branched structures. Any gas inclusions that form in the channels due to the influx of slurry from different sides will eventually vanish when the helium escapes. Also structures with dead ends, such as the micro tuning forks discussed in section 5.3, can be filled reliably. Only for long filling times of half an hour and more, the result can be deteriorated by bubbles that remain in the microcast. The bubbles are associated to air that diffuses into the sealed casts, or solvent that evaporates from the slurry. As roughly approximated by the equation of Hagen-Poiseuille [174], the time required to fill a channel of given length increases quadratically upon reduction of the channel's width. Thus, structures with high aspect ratios are the most critical. To avoid remaining bubbles in the metamaterial beam's microcast with channel lengths of more than 4 mm and widths down to around 20 µm, a buffer volume is added at the top (cf. Fig. 4.8(a)). The buffer volume adds additional drag during the filling procedure and retains potential bubbles. It can be clipped off with pliers after the UV-curing.
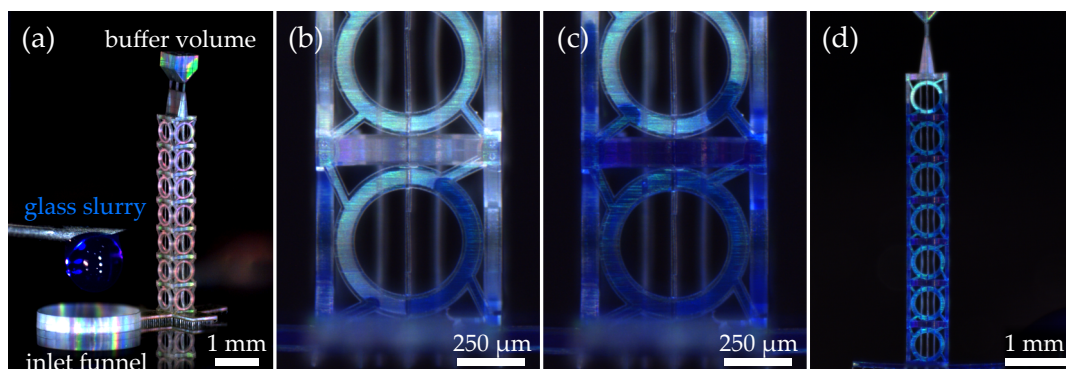
Figure 4.8: Optical micrographs taken during the helium-assisted microcasting process. (a) While kept in a helium environment, the glass slurry is filled into the inlet funnel of the microcast. The slurry is gradually sucked into the cast, as shown (b) after 60 s, and (c) after 150 s. (d) Almost the complete cast is filled after 20 min. The buffer volume at the top in (a) helps to avoid the formation of bubbles in the relevant parts of the cast. The glass slurry has been colored with a blue dye (Disperse Blue 134, Sigma-Aldrich) for illustration purposes. Adapted from [137] (CC BY 4.0).

4.5 THERMAL DEBINDING AND SINTERING

For the thermal treatment, the UV-cured samples are transferred to sapphire substrates and placed in an alumina crucible. The treatment is carried out in a tube furnace (STF15/180, Carbolite Gero) along the lines of previous work [163]. The steps are shown in Table 4.1. First, the thermal debinding with temperatures of up to 600°C is conducted in air under ambient conditions. In this step, the polymer cast and the slurry's polymeric binder and solvent are removed. Afterward, ceramic insulation plugs are carefully inserted into both ends of the tube furnace. The furnace is sealed with vacuum flanges and connected to a turbomolecular pump connected via a gas nozzle. Then, the sintering is conducted under vacuum ($< 10^{-3}$mbar) at temperatures up to 1225°C. It should be noted that the sintering results are sensitive to changes in the range of $\pm 10°$C in the maximum temperature. Therefore, the calibration of the tube furnace's temperature sensor should be checked occasionally. In the thermally debound state, the 3D microstructures are fragile and should not be exposed to any mechanical vibrations or shocks. Only by the sintering process, the samples become mechanically stable. The SEM images of a fracture surface in Figure 4.9 verify that the thermal treatment is sufficient to sinter the delicate 3D microstructures. The fused-silica nanoparticles in the structure's interior are consolidated to bulk fused-silica glass, such that the surface is smooth and homogeneous. In contrast, the fracture surface of a thermally debound sample is grainy and consists of individual nanoparticles, as expected

(a) sintered

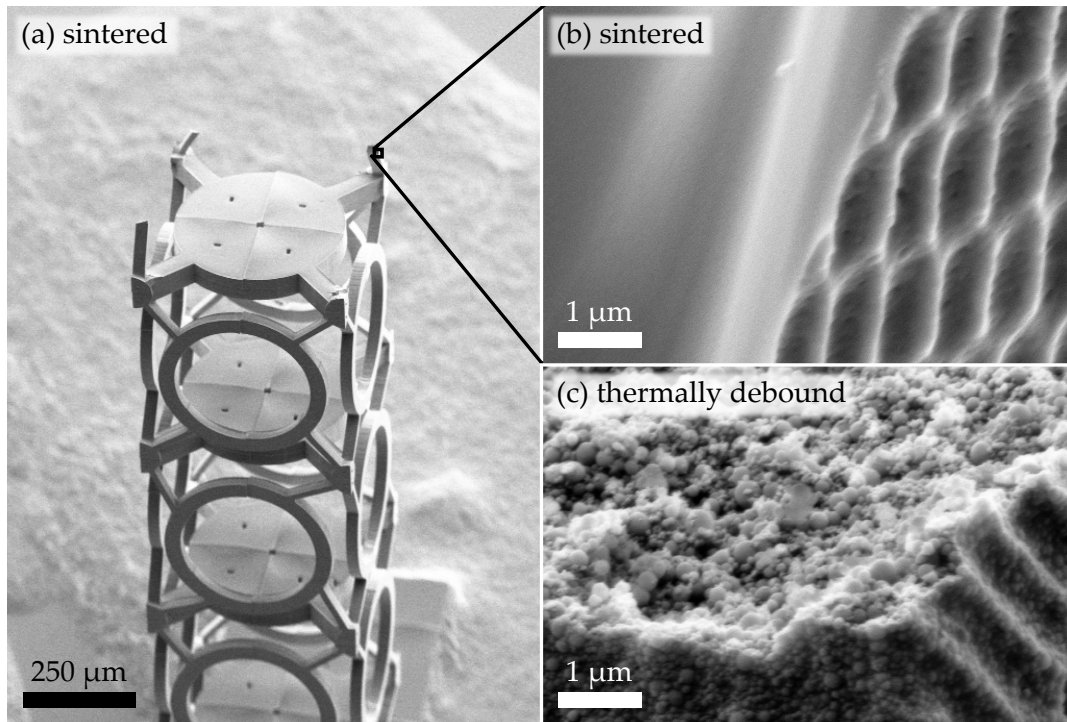(b) sintered

1 μm

(c) thermally debound

1 μm

250 μm

Figure 4.9: Scanning electron micrographs of the metamaterial beam. (a) The sintered beam was intentionally broken to check the sintering result. (b) The fracture surface (left part of the image) of a broken beam looks smooth and homogeneous. At the outer boundary of the beam (right part), the structure is rippled due to the microcast's surface (cf. Fig. 4.5). (c) In contrast, the individual silica nanoparticles are still visible on the fracture surface (upper part of the image) of a sample that was only thermally debound at 600°C.

	heating rate (K/min)	target temperature (°C)	dwell time (min)
thermal debinding (air)	0.5	150	120
	0.5	320	240
	0.5	600	120
	-3	25	-
sintering (vacuum)	3	800	90
	3	1225	10
	-3	25	-

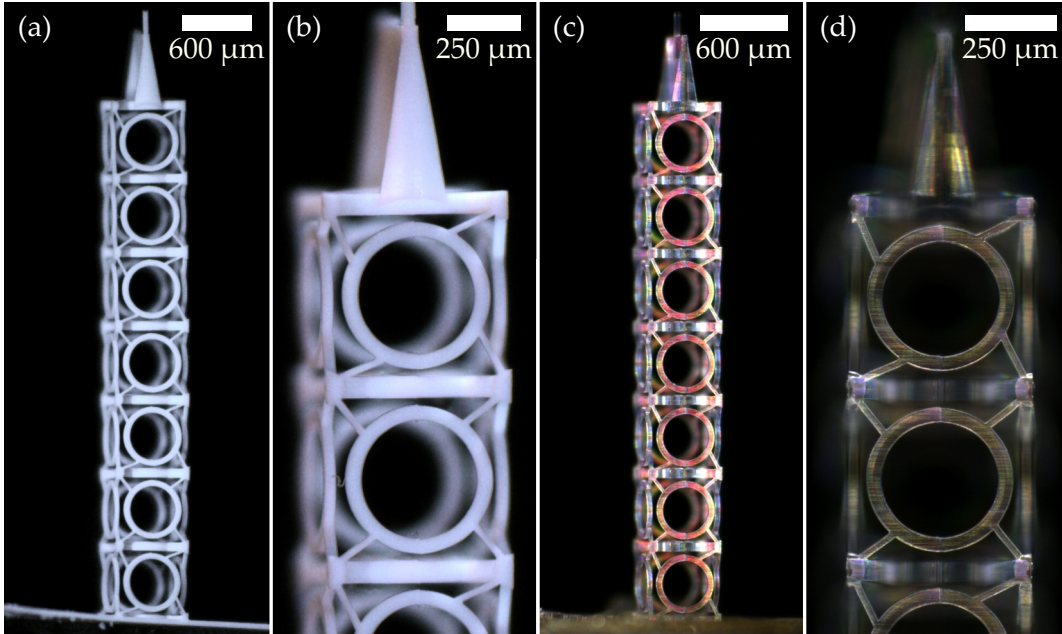Table 4.1: Process steps of the thermal treatment, along the lines of previous work [163].

Figure 4.10: Optical micrographs of metamaterial beams under ring-light illumination (a)(b) after thermal debinding and (c)(d) after sintering of the samples. The structures are in excellent agreement with the original design (cf. Fig. 3.9). By sintering, the material changes from porous and opaque to solid and transparent. The bright and colored appearance in (c) is due to the rippled surface, causing scattering, refraction, and interference of light. Panel (c) and (d) adapted from [137] (CC BY 4.0).

from the glass slurry (cf. Fig. 4.6). In accordance, the thermally debound samples are opaque and strongly scatter light, while the final sintered fused-silica samples are transparent, as shown in Figure 4.10. The sintered samples only scatter some light at the rippled surfaces which are a result of the coarse polymeric microcast (cf. Fig. 4.9). In this work, we only want to make use of the mechanical properties of the glass structures, as characterized in section 5.3. The surface quality is not expected to have a dominant effect on the bulk glass properties and is thus not of great interest in the following. The relative linear shrinkage of the samples from nominal cast size to the finally sintered samples is 22% for glass slurry L40.

As shown in Figures 4.10 (c) and (d), the resulting fused-silica 3D metamaterial beams are in excellent agreement with the original design (cf. Fig. 3.9). The final cube cell size is $l = 505\,\mu m$. The critical thin beams with a width of around $b_1 = 16\,\mu m$ and the corresponding angles are produced in high fidelity via the helium-assisted microcast approach. The observed maximum deviation in the width of nominally equivalent beams is $\pm 5\%$. The only major deformation that was occasionally observed was an overall bending of the metamaterial beam. This bending was linked to the influence of gravity during the sintering process. When

Figure 4.11: Thermal treatment of samples in upside-down position. During the thermal debinding and sintering process, the slurry reduces to bare silica nanoparticles. As they consolidate, the structure is prone to deformations. To avoid deformations due to gravity and thereby increase the yield of the process, the samples can be placed upside down in a slit between two sapphire substrates.
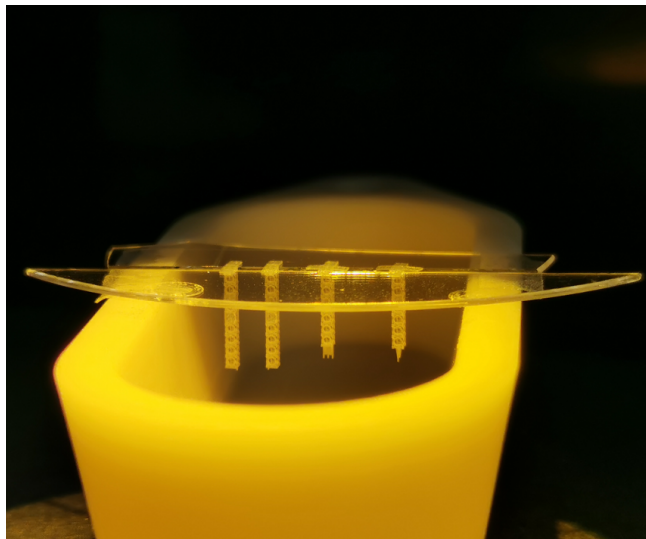
sintered in upright position, some samples showed the tendency to bend toward the side as imposed by gravity. While it is still possible to obtain excellent 3D structures, e.g., the ones shown in Figure 4.10, deformed samples are avoided best by thermally treating the samples upside down, as shown in Figure 4.11.

4.6 TOWARD DIFFERENT CONSTITUENT MATERIALS

Remarkably, none of the fabrication steps discussed above relies on the fact that we use a slurry that contains fused-silica glass particles. In fact, the helium-assisted microcast approach can be easily transferred to inks, sol-gel mixtures, and nanocomposites for other materials. Together with Maximilian Bojanowski, I conducted preliminary experiments on the fabrication of 3D structures out of the semiconductor indium tin oxide (ITO) and out of silver. Exemplary results after thermal treatment are shown in Figure 4.12. For the ITO structures, a self-mixed slurry with ITO nanoparticles was used. The silver structures are based on a commercial silver ink (Loctite ECI 1011 E&C, Henkel) for printed electronics and are prone to deformations. A main reason for this is that the silver ink does not contain curable monomers, such that the structure solidifies only by evaporation of solvent. An adapted ink mixture could resolve the issue. Especially the resulting ITO structures show the potential of the helium-assisted microcasting. The quality is partially comparable to that of the glass structures. At some positions, cracks and residuals of the slurry are visible. Both can be probably avoided by carefully adjusting the parameters of the thermal treatment.
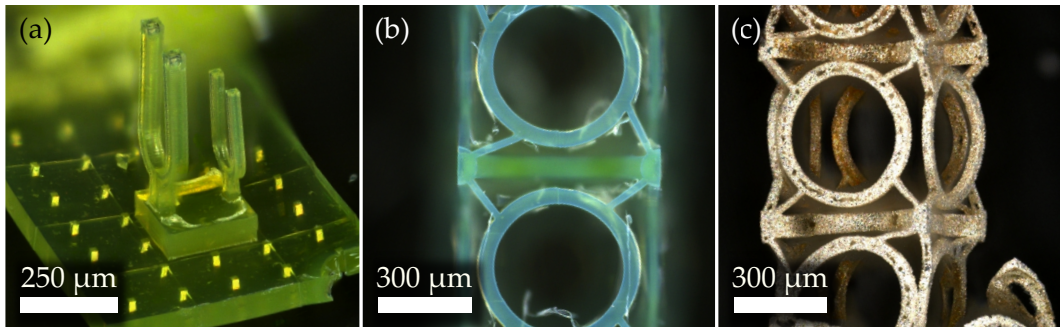
Figure 4.12: Optical micrographs of 3D microstructures of constituent materials other than fused-silica glass. Via the helium-assisted microcasting it is possible to fabricate exemplary (a) micro tuning forks or (b) 3D chiral metamaterial beams out of indium tin oxide. (c) Also 3D structures out of silver are possible.

4.7 SUMMARY AND DISCUSSION

For fused silica as constituent material, I have shown that two-photon 3D laser printing of polymeric casts combined with helium-assisted microcasting of a commercial glass slurry provides 3D microstructures with high fidelity. The quality of the final structures has been found to be mainly determined by the roughness of the fabricated microcast. Hence, the fabrication of smooth glass surfaces, e.g., for optical applications, requires further optimization. Achieving optically smooth surfaces has almost become standard in 3D laser printing [175, 176]. The challenge for the microcasts is to reach this high surface quality without triggering a too large proximity effect within the cast's channels.

In the presented 3D laser printing setup, the proximity effect also limits the minimal feature size of the final glass structures. Finer features should be possible by using a different objective lens and photoresist (e.g., IP-Dip or IP-L, Nanoscribe). However, thereby the printing times would increase significantly, such that this is only an option for samples smaller than the ones discussed above. Apart from the proximity effect, the outcome of the helium-assisted microcasting is limited by the viscosity of the slurry and the associated filling times. The presented buffer volume and the usage of Glassomer L50 ease this limitation to some extent. For structures with even more extreme aspect ratios than the ones presented, the filling time could be further reduced by applying a gradually increasing external pressure during the procedure.

The potential of the helium-assisted microcasting in terms of its transferability to other materials has been shown in the section above. In this sense, the approach is a promising alternative to direct two- or multi-photon 3D laser printing of nonpolymeric structures. The formulation of photoresists which are suitable for 3D laser printing is complex and specific for each target material [177]. For the microcasting, the optimization criteria of a slurry is mostly limited to its

viscosity and its stability and shrinkage during the thermal treatment. For 3D laser printing, a photoresist in addition has to be transparent and printable in a convenient manner, i.e., with a reasonable scan speed and laser power. For instance, an opaque slurry can be perfectly suitable for microcasting but is conceptually useless for 3D laser printing.

Apart from semiconducting and metallic constituent materials, such as ITO and silver, also ceramics can be fabricated from sol-gel mixtures or nanocomposites [155, 178, 179]. Thereby, complex piezoelectric or even superconducting 3D microstructures are in reach. Also, the helium-assisted microcasting could be used to infiltrate polymeric shell structures with liquid metal or ferromagnetic fluids [180, 181].

5

Ultrasound Experiments on Topological Resonances

In this chapter, I will show the experimental demonstration of the aimed-at topologically protected twist edge resonances for the fabricated 3D chiral fused-silica metamaterial beams. First, I will shortly introduce the experimental setup that is used to excite 3D microstructures at ultrasound frequencies and image the resulting mechanical oscillations. Second, I will show how the displacements at selected sample positions are determined via digital image cross-correlation. Subsequently, I will present the measured resonance curves of micro tuning forks and the derived material properties and mechanical quality factors of polymer and fused silica. I will shortly discuss different damping mechanisms in the experiment. Afterward, I will show the experimental results for the chiral topological fused-silica metamaterial beams. Thereby, both the mechanical response spectrum of the structure and the emerging twist edge resonances will be characterized. At the end of the chapter, I will summarize and discuss the overall experimental results.

The key experimental results have already been published previously [137]. I have conducted all measurements and the data analysis. Martin Wegener has had an advisory role. Contributions of Tobias Frenzel and Erik Jung are specified in the corresponding sections.

5.1 Experimental Setup

In the experiments, we want to verify the existence of the topologically protected twist edge modes in chiral 3D glass metamaterial beams, designed and fabricated as shown in the last two chapters. From the metamaterial cell size of $l = 505\,\mu\mathrm{m}$ and the expected stiffness of fused silica, one arrives at a resonance frequency of the edge modes of around $270\,\mathrm{kHz}$. The experimental setup shown in Figure 5.1
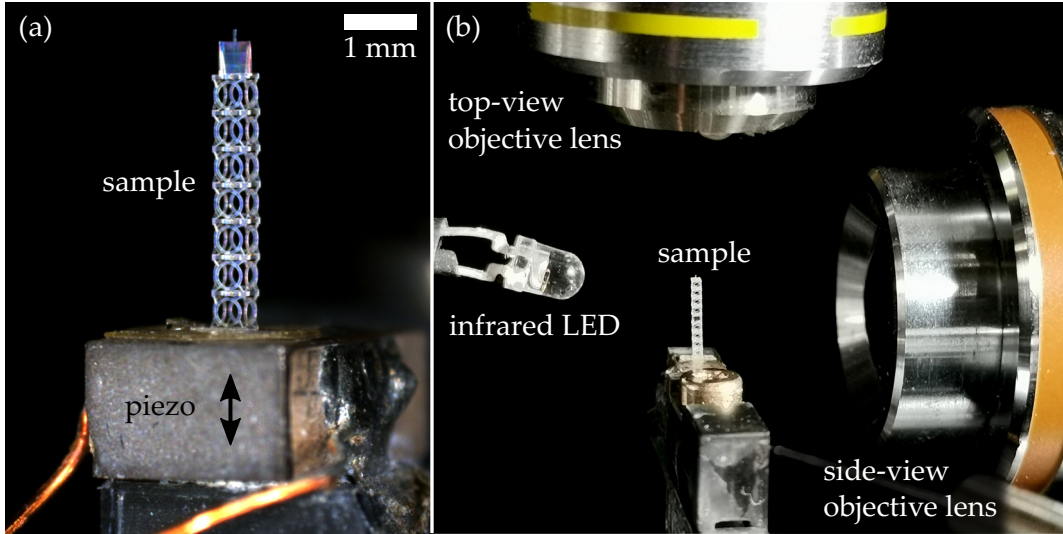
Figure 5.1: Experimental setup. (a) The sample is glued onto a piezoelectric actuator (piezo). The piezo is contacted with stranded copper wire at the sides and provides a vertical actuation (black arrows) when driven with a sinusoidal voltage. (b) The sample is imaged from the top and side via two optical microscopes. To extract slow-motion videos, an infrared LED provides a stroboscopic illumination. The setup was built by Tobias Frenzel [16, 17].

is capable of providing both the actuation and the imaging of 3D microstructures at such frequencies. The system was built by Tobias Frenzel and used in previous work to show acoustical activity in chiral mechanical metamaterials [16, 17]. It combines an optical-microscopy setup with a stroboscopic illumination of the excited samples, which effectively results in the acquisition of slow-motion videos.

The samples are glued (UHU Plast Special, UHU) onto a piezoelectric actuator ($2 \times 3 \times 5 \, mm^3$ PICMA Chip Actuator, Physik Instrumente) in upright position. Via a frequency generator (33612A, Keysight) and a voltage amplifier (A 1230-01 linear amplifier, Hubert), a sinusoidal voltage is applied to the piezoelectric actuator, such that a time-harmonic axial motion is imposed at the bottom of the sample. The actuation is synchronized to the stroboscopic illumination provided by two infrared light-emitting diodes (VSLY 3850 LED, 850 nm center wavelength, Vishay). The LEDs are driven with periodic rectangular pulses with a duty cycle of 1.5%. The short duty cycle assures that the images are not blurred due to the sample's motion. The beat frequency between actuation and illumination is set to 1 Hz. The microstructures are imaged in top-view and side-view via two microscope objective lenses (Epiplan $10 \times / 0.20$, Zeiss, and Epiplan Neofluar $2.5 \times / 0.075$, Zeiss) and corresponding tube lenses (focal length 150 mm, AC254-150-A-ML, Thorlabs). A higher magnification (Plan L $25 \times / 0.40$, Leitz Wetzlar) is used to also detect the motion of the piezoelectric actuator with amplitudes in the range of only a few nanometers. Digital optical images are acquired by two

complementary metal-oxide semiconductor (CMOS) cameras (BFLY-PGE-50S5M-C and BFLY-PGE31S4M-C, FLIR Systems), each set to a frame rate of 20 frames/s. This means that a sample which is actuated with a frequency of 270 kHz undergoes 13500 oscillations between two subsequent images of an acquired slow-motion video. To reduce drifts due to air flow, temperature variations, and mechanical vibrations during the image acquisition, the setup is placed on an optical table and can be covered by a housing.

Frequency Sweeps

In order to detect and characterize mechanical resonances, it is necessary to sweep the excitation frequency while imaging the response of the microstructures. The setup's frequency generator is connected to a personal computer and controlled via a home-written software (Matlab). Thereby, it is possible to change the excitation frequency step-wise across the interval of interest. For the frequency sweeps in this work, images are acquired for a time of 3 s for each frequency step. For the given beat frequency and frame rate this corresponds to 60 sampling points over 3 oscillations of the induced time-harmonic motion. Before each acquisition, the system is driven for one second to accommodate to the frequency change.

5.2 DIGITAL IMAGE CROSS-CORRELATION

To extract the microstructures' motion upon excitation from the acquired videos, we use digital image cross-correlation [182–184]. This method was used previously to detect local displacement vectors in mechanical metamaterials [126, 165, 173, 185] and is based on an open-access Matlab software package [186]. The analysis starts with two digital images $I_1(x, y)$ and $I_2(x, y)$, with pixelated coordinates $x = n_x p$ and $y = n_y p$. Here, p is the pixel size in the object plane and n_x and n_y are integers. To track a potential displacement (u_x, u_y) of an element of interest between the two images, one evaluates the 2D cross-correlation function

$$C(\Delta x, \Delta y) = \int_{\text{ROI}} I_1(x, y) \, I_2(x + \Delta x, y + \Delta y) \, \mathrm{d}x \mathrm{d}y. \tag{5.1}$$

Thereby, the integral is performed only over a small region of interest (ROI) which contains the element that will be tracked, as shown in Figure 5.2. Additionally, the cross-correlation is normalized to the average brightness level of the input images to make the procedure insensitive to potential changes in the illumination. The shift $(\Delta x, \Delta y) = (\Delta n_x p, \Delta n_y p)$ for which the cross-correlation is maximized provides the element's displacement with an accuracy limited by the pixel size. However, for the experiments we rely on imaging a large field of
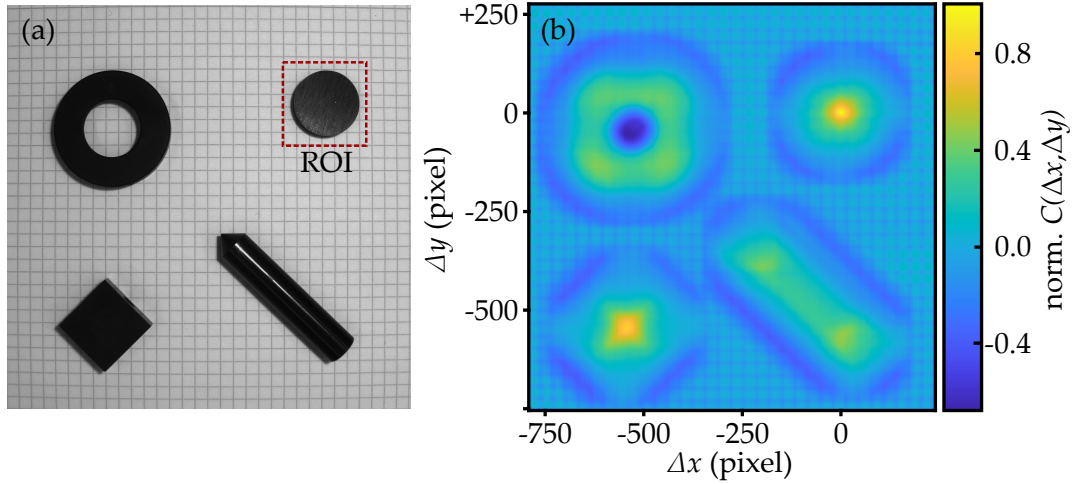
Figure 5.2: Exemplary digital image cross-correlation for simple geometrical objects. (a) To track a potential displacement of the black disk, one defines a region of interest (ROI) that contains the object. (b) In the original image, the normalized cross-correlation has its maximum for a zero shift $(\Delta x, \Delta y) = (0, 0)$. When the object moves, this maximum is shifted to different pixel coordinates in subsequent images.

view, corresponding to small magnifications and large pixel sizes. For the $2.5\times$ objective lens in the setup as described above, the pixel size is around $p = 1.5\,\mu m$. To extract displacements with subpixel accuracy, the cross-correlation function is fitted by a 2D parabola over the 3×3 pixels around the maximum, as shown in Figure 5.3. The position of the 2D parabola's maximum corresponds to the displacement vector (u_x, u_y) of the region of interest between the two images I_1 and I_2. By conducting this analysis for a complete image series and multiple regions of interest, we obtain the time-dependent displacements for characteristic points of a given sample.

Notably, the accuracy of the described cross-correlation analysis is not limited by the resolution of the tracked objects and the images themselves but rather by the signal-to-noise ratio. Thus, with a sufficient image quality, accuracies down to $1/100$ of the pixel size are possible [126]. Together with Tobias Frenzel, I showed that the error on the measured displacements can be pushed even below one Ångström by tracking 8×8 ROI on a footprint of $40\times40\,\mu m^2$ at frame rates of 80 frames/s using a white-light illumination [187].
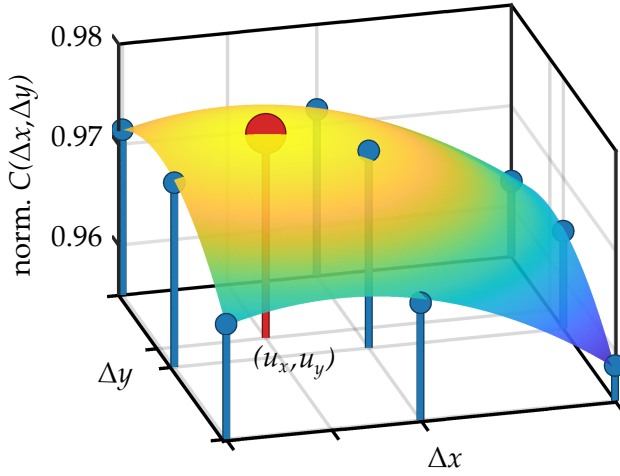
Figure 5.3: Digital image cross-correlation with subpixel accuracy. The normalized cross-correlation $C(\Delta x, \Delta y)$ is fitted by a 2D parabola (colored plane) for the 3×3 pixels (blue bars and circles) around its maximum. Due to noise and pixelation of the images, the maximum of the cross-correlation is slightly smaller than unity. The coordinates (u_x, u_y) where the 2D parabola has its maximum (red bar and circle) correspond to the subpixel-accuracy displacement vector.

5.3 MICRO TUNING FORKS

Before characterizing fused-silica 3D chiral topological metamaterial beams, we use the experimental setup and the image cross-correlation analysis to retrieve the mechanical properties of fused silica at ultrasound frequencies. A corresponding analysis is conducted for polymer. Thereby, we can reveal the benefit of fused silica structures, fabricated along the lines of chapter 4, as compared to typical 3D laser-printed polymer structures. The approach was established together with Eric Jung in the course of his bachelor's thesis. There, we retrieved the mechanical material parameters of polymer in the context of experiments on the acoustical activity of chiral metamaterials [17].

For the material analysis, we measure the resonance curves of micro tuning forks. By comparing the resonance frequencies to corresponding finite-element method (FEM) calculations, we obtain the Young's modulus of the tuning fork's constituent material. Moreover, we can characterize the material damping and the associated quality factor from the resonance width according to the damped harmonic oscillator model in section 2.4.1.

Tuning forks offer several advantages in terms of a characterization of their constituent material. First, the forks have a simple geometry which allows for a high fidelity both in the fabrication process and in the FEM calculations. Second, the tuning forks can be actuated in their fundamental antisymmetric mode where the two prongs oscillate in counterphase. The excitation of this mode can be accomplished by an axial motion on the bottom, thus in the same way as required
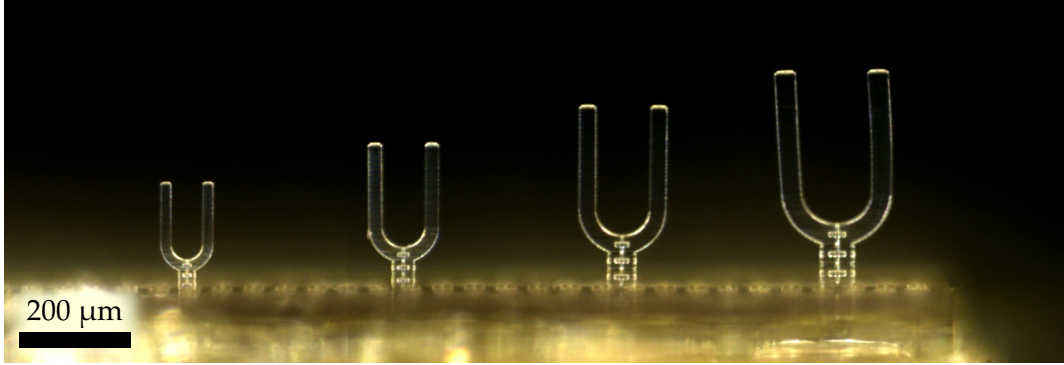
Figure 5.4: Optical micrograph of polymer micro tuning forks. Via 3D laser printing, four tuning forks of different sizes were fabricated to investigate the material damping of polymer at different frequencies. The handle and the top faces of the two prongs of each tuning fork are marked with crosses to track displacements.

for the 3D chiral metamaterial beams. In the antisymmetric mode, both anchor losses due to mechanical vibrations of the fork's handle and acoustic radiation losses via the oscillating prongs are minimized [140]. Both loss effects would add up to the material damping and thereby reduce the quality factor according to equation 2.45. A third advantage lies in the measurement of the prongs' displacement. As the tips of both prongs can be tracked simultaneously, drifts between the sample and the imaging setup during the acquisition cancel out when splitting the measured displacements into its symmetric and antisymmetric components.

5.3.1 Mechanical Properties of Polymer Structures

Polymer tuning forks are fabricated via two-photon 3D laser printing, using the same configuration as introduced in section 4.2. We use standard printing parameters with a hatching distance of 0.3 µm, a slicing distance of 0.5 µm, and a nominal laser power of 22.5 mW. The tuning forks were fabricated in four different sizes, as shown in Figure 5.4. The resonance curve of the fundamental antisymmetric mode is measured for each of the tuning forks. Thereby, the displacement amplitude at the tips is normalized to the excitation amplitude at the fork's handle. By tracking both motions simultaneously in the side-view, the phase lag between the time-harmonic excitation and the resonating tips is determined as well. The results are shown in Figure 5.5(b) and (c). The resonances are clearly visible both in the amplitudes and phase lags. The quality factors are extracted by least-squares fits of the resonance curves according to the damped harmonic oscillator model in equation 2.42. In the considered frequency interval, similar quality factors of around $Q = 21 \pm 1$ are observed. For the topological
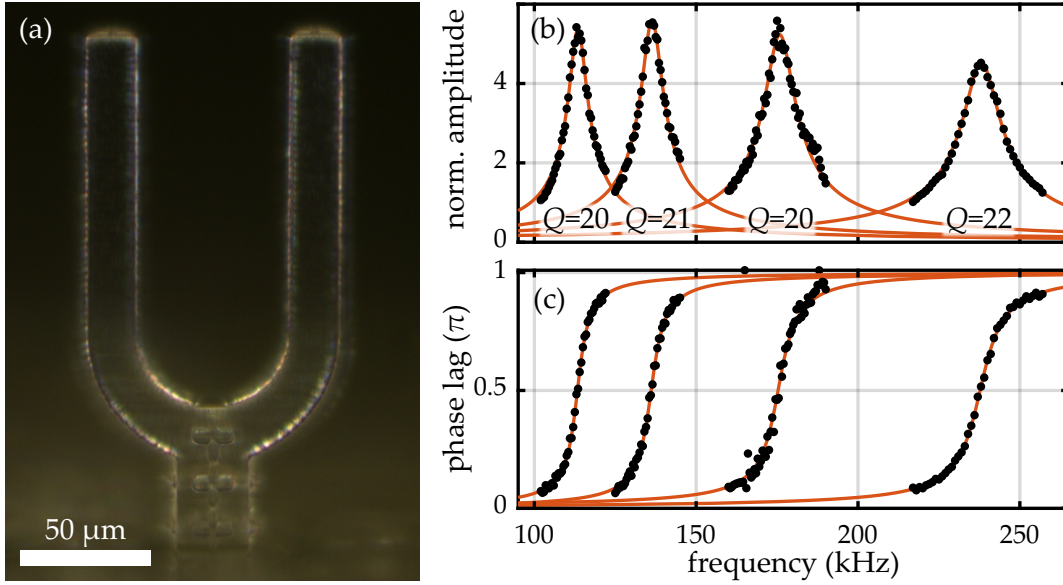
Figure 5.5: (a) Close-up view of the smallest polymer tuning fork (cf. Fig 5.4). (b) Resonance curves (black dots) of the four polymer tuning forks of different size. The least-squares fits (orange lines) result in quality factors between $Q = 20$ and $Q = 22$. For all tuning forks, the amplitude enhancement is below 6. (c) The measured frequency-dependent phase lags (black dots) between excitation and tip displacement are as expected for a damped harmonic oscillator around its resonance. Panel (a) adapted from [137] (CC BY 4.0).

twist edge mode of the chiral metamaterial beam we aim at a resonance frequency of around 250 kHz. The smallest polymer tuning fork, shown in Figure 5.5(a), has its resonance at a frequency of around 240 kHz. Using a mass density of $\rho_{poly} = 1.15\,g/cm^3$ and a Poisson's ratio of $\nu_{poly} = 0.4$ in corresponding FEM calculations of the tuning fork [17], we obtain a complex dynamical Young's modulus of $E_{poly} = 4.90\,(\pm 0.12)\,GPa + i\,0.22\,(\pm 0.01)\,GPa$ for polymer. The systematic error is derived from an estimated uncertainty of $\pm 0.5\,\mu m$ on the measured width of U-shaped element that connects the two prongs. Similar material parameters were obtained for the polymer SU8 at frequencies up to 20 kHz [188].

The small quality factor of only $Q = 22$ rules out polymer as a constituent material for a resonant converter from longitudinal to rotational oscillations, as discussed in section 3.4.3. The measured amplitude enhancement between excitation and displacement of the tuning fork's tips is only slightly larger than four. For the topological mode converter the enhancement factor would be expected to be even below one (cf. Fig. 3.11). Hence, in the desired frequency regime, the viscous damping of polymer is too pronounced to obtain any resonant enhancement. As already indicated in chapter 4, the route to larger quality factors is to fabricate 3D microstructures out of other materials, i.e., out of fused-silica glass.
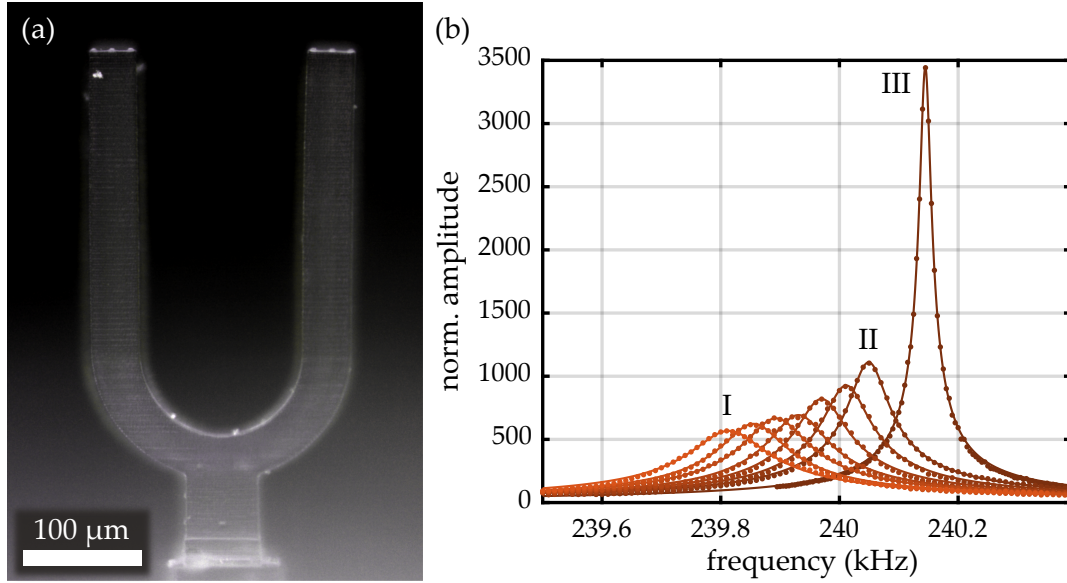
Figure 5.6: (a) Optical micrograph of a fused-silica tuning fork fabricated via helium-assisted microcasting. (b) Associated resonance curves measured at 3 to 0 bar above ambient pressure (I to II) in steps of 0.5 bar, and under vacuum (III). When reducing the pressure, the quality factor increases from $Q = 1882$ (I) to $Q = 3582$ (II), indicating that air damping governs the quality factor. Under vacuum (< 1 mbar), the quality factor is as large as $Q = 12450$. Adapted from [137] (CC BY 4.0).

5.3.2 Mechanical Properties of Fused-Silica Structures

The characterization of fused silica as a constituent material for 3D microstructures goes along the same line as for polymer. Fused-silica tuning forks are fabricated via the helium-assisted microcast approach presented in chapter 4. The tuning fork shown in Figure 5.6(a) has been designed to have the same geometry and resonance frequency as the polymer tuning fork in Figure 5.5(a). As shown in Figure 5.6(b), the fork exhibits a quality factor of $Q = 3582$ at ambient conditions. Thus, in comparison to the polymer tuning forks, the quality factor is increased by more than two orders of magnitude. Similarly, the amplitude enhancement increases to above 1000. In fact, the measured quality factor is not limited due to the viscous material damping of fused silica but due to air damping. This becomes obvious from tuning fork resonance measurements at different pressure levels, as shown in Figure 5.6(b). For these measurements, the tuning forks were imaged from the top through the window of a pressure chamber that was used in previous work [173, 185]. The resulting quality factors show a clear dependence on the air pressure, ranging from $Q = 1882$ at 3 bar above ambient pressure to $Q = 12450$ in vacuum (< 1 mbar). There, the amplitude enhancement at the resonance frequency exceeds 3000. Hence, the measurements confirm
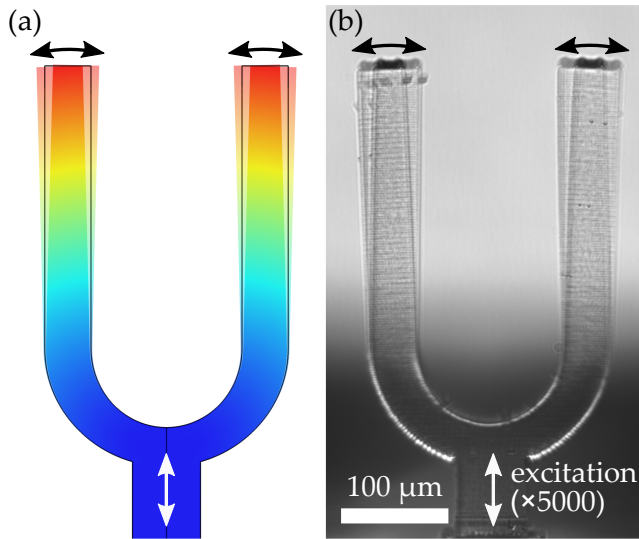
Figure 5.7: Fused-silica tuning fork oscillating in the fundamental anti-symmetric mode (a) in FEM calculations and (b) in the acquired images. To illustrate the oscillation (black arrows), the two images with the extremal displacements of the prongs are overlayed. The excitation amplitude of 7 nm at the bottom (white arrows, scaled up by a factor of 5000) is more than three orders of magnitude smaller and hence not visible as displacement. Panel (b) adapted from [137] (CC BY 4.0).

that the limitations due to material damping are lifted when using fused-silica microstructures.

By comparing the resonance frequency to corresponding FEM calculations of the tuning fork, we arrive at dynamical Young's modulus of fused silica of $E_{\mathrm{silica}} = 70.8\,(\pm 2.7)\,\mathrm{GPa}$ at frequencies around 240 kHz. A mass density of $\rho_{\mathrm{silica}} = 2.2\,\mathrm{g/cm^3}$ and a Poisson's ratio of $\nu_{\mathrm{silica}} = 0.17$ is assumed [142, 143]. Again, the systematic error is derived from the estimated accuracy of the measured geometrical dimensions. The dynamical Young's modulus is in good agreement with the value of $E = 72.9\,\mathrm{GPa}$ for bulk fused-silica glass [143]. This means that the fabricated fused silica has a stiffness which is almost a factor of 15 larger as compared to polymer. Following equation 2.24, the resonance frequencies of fused-silica samples are three times higher as for a polymer structure of the same size.

In all of the above measurements, the excitation was tuned such that the prong displacements stayed well below 1 μm. This ensures that the strains and stresses occurring in the microstructures are small enough to justify the linear-elastic description of the material. Thereby, the associated FEM calculation can be assumed to be valid and damage to the microstructures is avoided. To still visualize the large enhancement factors obtained for the fused-silica tuning forks, the image acquisition was exemplarily conducted for larger excitation amplitudes, as shown in Figure 5.7. The large displacement of the prongs is clearly visible for an excitation amplitude of only 7 nm. In fact, the fused-silica tuning forks fracture for even larger excitation amplitudes.
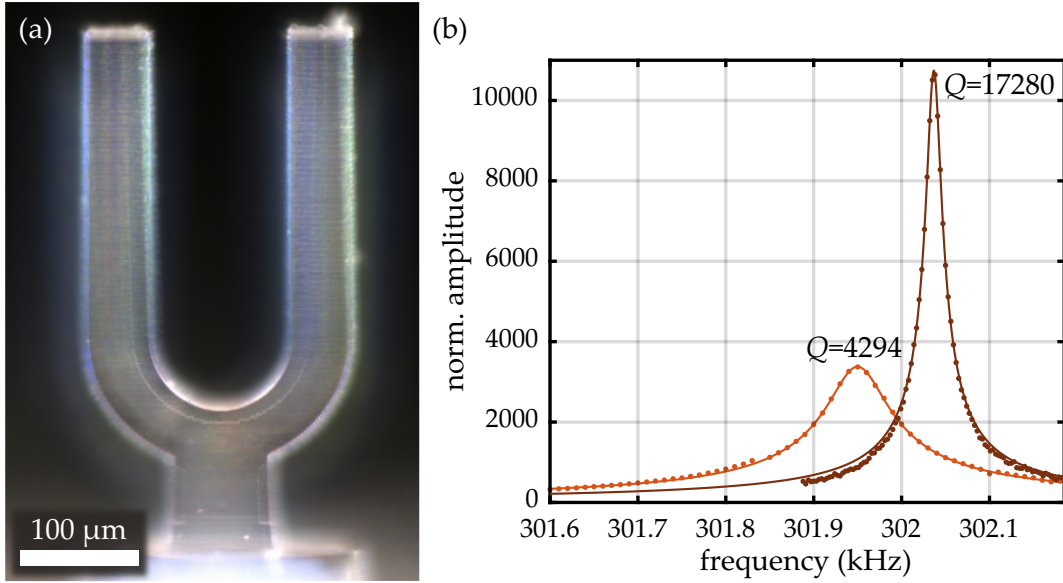
93

Figure 5.8: (a) Optical micrograph of a fused-silica tuning fork with thicker prongs. (b) The resonance curves at ambient conditions and under vacuum correspond to quality factors of $Q = 4294$ and $Q = 17280$, respectively. Comparison with Figure 5.6 shows that the quality factor is geometry-dependent due to damping mechanisms such as anchor losses. Adapted from [137] (CC BY 4.0).

5.3.3 Damping Mechanisms

As shown above, air damping limits the quality factor at ambient conditions, such that it is not possible to isolate the contribution of the viscous material damping of fused silica. In vacuum, the damping decreases significantly. However, the overall quality factor is still assumed to be a combination of different damping mechanisms according to equation 2.45. For pure viscous material damping, the quality factor is independent of the tuning fork's geometry. In contrast, other damping mechanisms scale with the overall size of the tuning fork or the aspect ratio of its prongs [140]. Such a behavior is also found for the fabricated fused-silica tuning forks. As shown in Figure 5.8, a higher quality factor of 17280 in vacuum is observed for a tuning fork with thicker prongs. The relevant scale-dependent damping mechanism may potentially be anchor loss [140, 141], which has been briefly discussed in terms of the metamaterial beam design in section 3.4.3. Also, residual air damping at pressures below 1 mbar and minor asymmetries between the tuning fork prongs may play a role. However, it is not within the scope of this work to isolate the various potential damping contributions for the fabricated microstructures. In this sense, it is not possible to assign a quality factor to fused silica which accounts only for the viscous material damping. Nevertheless,
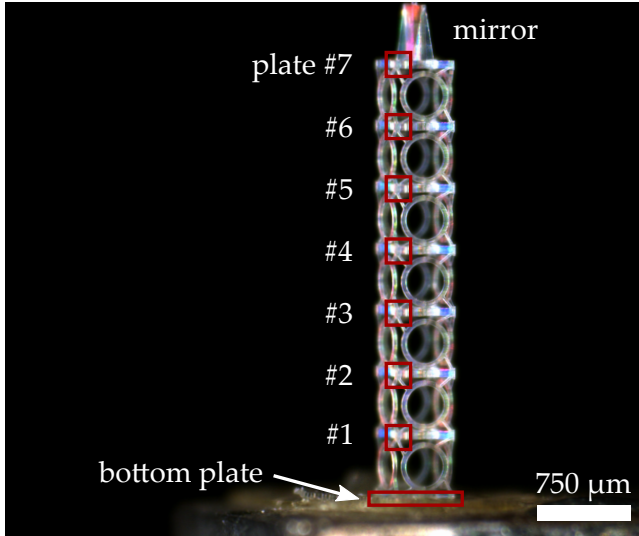
Figure 5.9: Tracking the motion of a 3D chiral metamaterial beam. The displacement vectors upon actuation are evaluated in side-view at the corners of the seven horizontal plates (small red boxes). For normalization, the axial displacement at the bottom plate is determined in a separate measurement by averaging over multiple ROI. The top with the added mirror plate is additionally imaged in top-view to verify the rotational character of the induced motion.

we use the complex dynamical Young's modulus in FEM calculations of fused-silica samples to account for all damping contributions of an individual structure. From the highest measured quality factor (cf. Fig. 5.8), we can at least give an upper limit for the imaginary part of the complex dynamical Young's modulus of $E''_{\text{silica}} < 4.1(\pm0.2)\,\text{MPa}$ at frequencies of around $300\,\text{kHz}$.

5.4 Topological Twist Edge Resonances

Given the promising results of the fused-silica micro tuning forks, we want to measure the resonant behavior of 3D chiral topological metamaterial beams. Having the application of a resonant mechanical laser-beam scanner in mind, it is not practicable to actuate the samples in a vacuum chamber. Hence, we conduct the measurements at ambient conditions and accept the limitations due to air damping. In Figure 5.1, the microstructure was already shown as mounted in the experimental setup. The expected resonance frequencies are calculated from the cube cell size of $l = 505\,\mu\text{m}$ of the fabricated metamaterial structure, the normalized frequencies following the design in section 3.4, and the material parameters of fused silica as derived above. To detect the metamaterial beam's motion, we track the displacements at the corner of each of its horizontal plates in side-view, as shown in Figure 5.9. Potential drifts between the sample and the imaging setup are removed from the measurements by subtracting the base line from the tracked oscillations. The vertical component of the displacement vector corresponds to a longitudinal (axial) motion and the horizontal component corresponds to a transverse or a rotational (azimuthal) motion. To distinguish between transverse and rotational motion, the sample is additionally imaged from the top. All displacements are normalized to the excitation by determining the
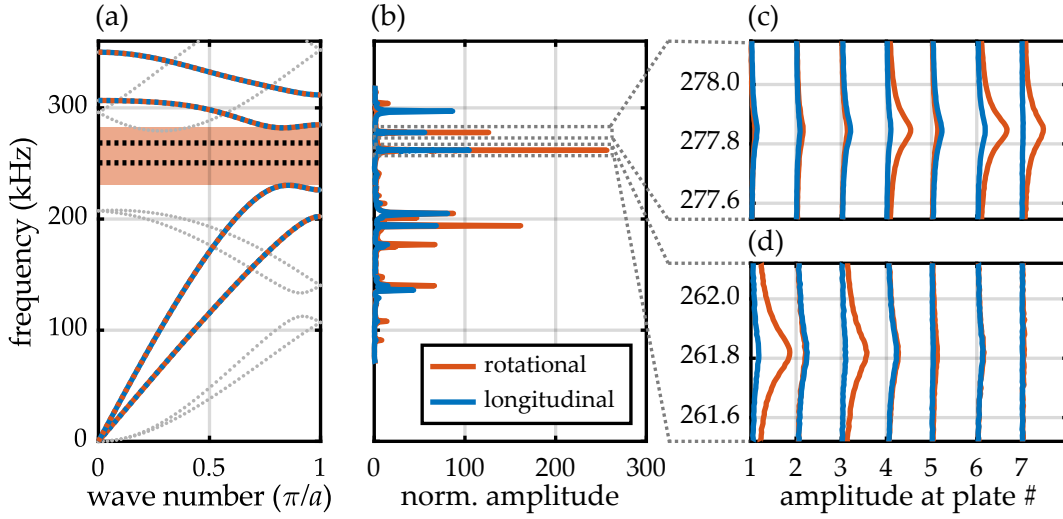
Figure 5.10: (a) Calculated band structure of an infinite metamaterial beam with the two edge modes (dashed black lines) within the 1D topological band gap (light-red region). The frequencies are obtained by scaling the normalized frequencies (cf. Fig. 3.10) according to the structure size and the determined dynamical Young's modulus of fused silica. (b) Measured mechanical response spectrum of the finite 3D chiral metamaterial beam, averaged over the seven horizontal plates and decomposed into its rotational (azimuthal) and longitudinal component. Bulk modes and two pronounced resonances with frequencies inside of the band gap region are visible. The response of the individual plates shows the localization of the edge modes (c) at the top edge (plate #7) and (d) at the bottom edge (plate #1). The amplitudes in (c) are scaled by a factor of 2 with respect to those in (d) for illustration purposes. Adapted from [137] (CC BY 4.0).

frequency-dependent axial amplitude at the bottom plate of the sample in a separate measurement. Therefore, we use an objective lens with higher magnification (see section 5.1) and average the displacement over multiple ROI to increase the measurement accuracy [187].

5.4.1 Mechanical Response Spectrum

In a first frequency sweep, the sample is actuated at frequencies from 70 to 320 kHz in steps of $\Delta f = 1\,\text{kHz}$. The resulting mechanical response spectrum averaged over all horizontal plates of the microstructure is shown in Figure 5.10. For comparison, the band structure obtained via FEM calculations (see section 3.4) is also displayed. The spectrum reveals several resonances. While most of the resonances are associated to bulk modes, we find two resonances with its frequencies within the expected 1D topological band gap of a corresponding infinitely periodic meta-
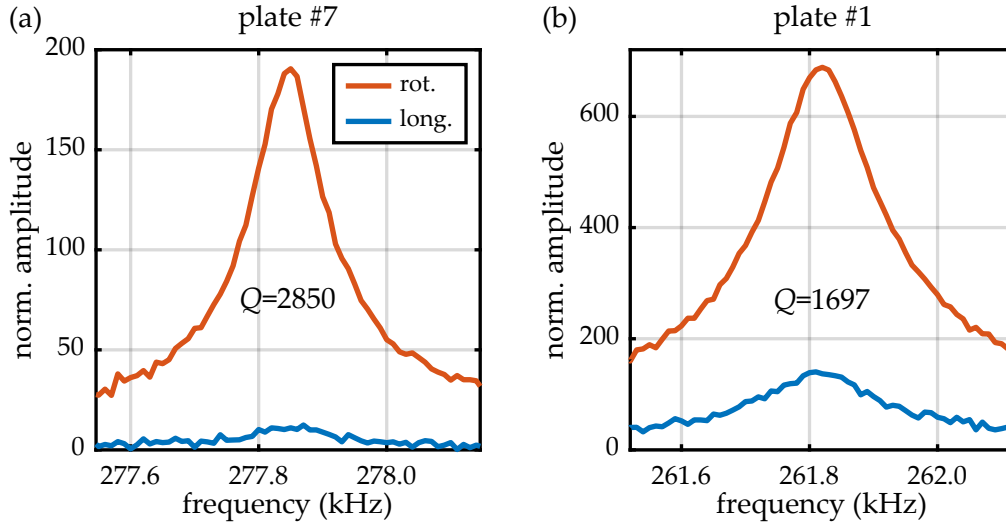
Figure 5.11: Close-up views of (a) the top-edge resonance at plate #7 and (b) the bottom-edge resonance at plate #1 (cf. Fig. 5.10). The top-edge resonance with a quality factor of $Q = 2850$ enhances the azimuthal displacement at the plate's corner by a factor of 190 with respect to the longitudinal excitation at the bottom. The bottom-edge resonance exhibits a larger enhancement but has a smaller quality factor of $Q = 1697$, probably due to anchor losses. Additionally, the amount of longitudinal motion is larger.

material beam. These two resonances are resolved in detail by a finer frequency sweep with a step size of $\Delta f = 0.01\,\text{kHz}$. We use a small excitation amplitude of around $1\,\text{nm}$ to induce displacements well below $1\,\mu\text{m}$. Thereby, we stay in the linear-elastic regime and avoid any damaging of the structure. Panels (c) and (d) of Figure 5.10 show the resulting response spectra for the individual microstructure plates. The resonance at around $277.8\,\text{kHz}$ is localized to the upper end of the microstructure. This clearly indicates the desired topologically protected edge mode at the mirror position. Similarly, the resonance at a slightly lower frequency of $261.8\,\text{kHz}$ is localized to the bottom end of the microstructure. This observation confirms the calculations for the coupled SSH model and the microstructure as presented in chapter 3.

The resonance curve of the top plate, shown in close-up view in Figure 5.11(a), is of particular interest for a potential laser-beam scanner application. The maximum amplitude enhancement from the axial excitation to the azimuthal displacement at the corner is 190. This allows for the desired resonant conversion from longitudinal to rotational motion. By a least-square fit, we obtain a quality factor of $Q = 2850$. Notably, the edge resonance localized at the bottom plate, shown in Figure 5.11(b), exhibits a lower quality factor of $Q = 1697$, but a larger amplitude enhancement of 690. Both effects are associated to the much stronger coupling of this edge mode

to the bottom plate and the piezoelectric transducer. As discussed in section 3.4.3, the strong coupling increases the amplitude enhancement while decreasing the quality factor due to anchor losses. Altogether, the overall beam length of seven cube cells proves to be suitable to obtain a large amplitude enhancement while still maintaining a high quality factor for the top edge resonance. This confirms the design principles presented in section 3.4.3.
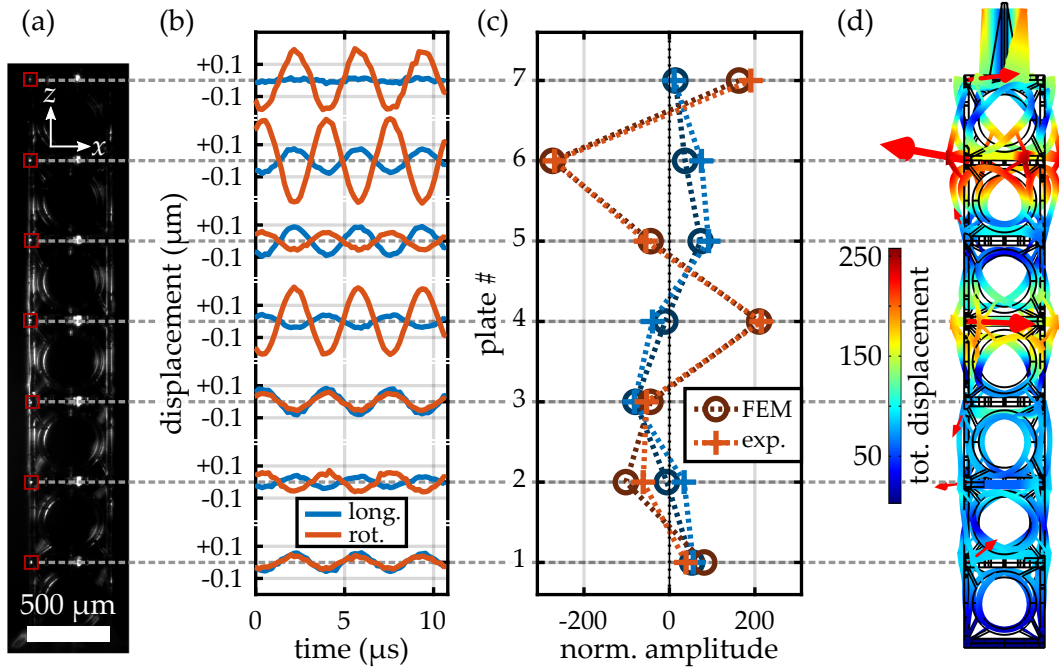

Figure 5.12: Mode characterization of the top-edge resonance. (a) Side-view optical microscopy image of the fused-silica metamaterial beam. The red boxes mark the ROI that were tracked via image cross-correlation. (b) Tracked longitudinal (blue) and rotational (orange) time-harmonic displacements of the individual plates at the resonance frequency of 277.85 kHz for an excitation amplitude of 1 nm at the bottom. The time scale corresponds to the real-time oscillation of the sample. (c) The derived normalized amplitudes (circles) agree well with those of corresponding FEM calculations (crosses), scaled by a global factor. Positive (negative) amplitudes correspond to an oscillation in phase (counterphase) with respect to the longitudinal component of plate #1. (d) The red arrows indicate the calculated normalized displacement vectors at the plate's corners. The normalized total displacement field is scaled up for clarity. Adapted from [137] (CC BY 4.0).
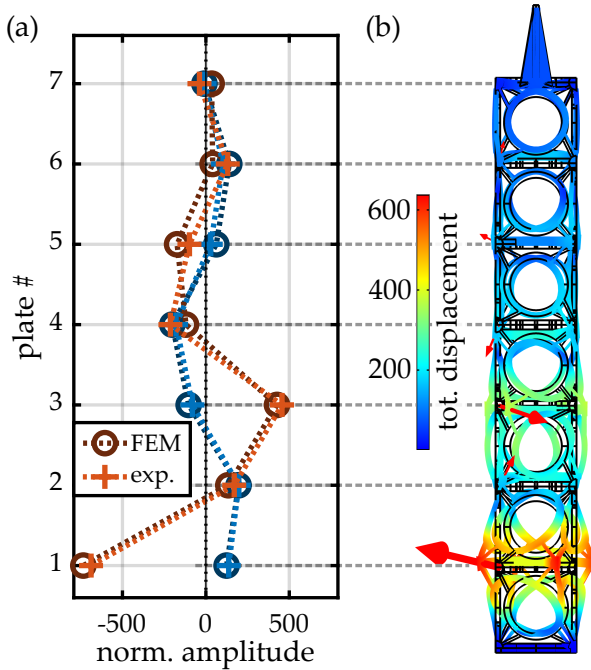
Figure 5.13: Mode characterization of the bottom-edge resonance at a frequency of 261.82 kHz. (a) As for the top-edge resonance (cf. Fig 5.12), the measured normalized longitudinal (blue) and azimuthal (orange) displacement amplitudes and phase relations of the individual plates (circles) are in good agreement with corresponding FEM calculations (crosses), scaled by a global factor. (b) The normalized total displacement field and the displacement vectors at the corners show the overall shape of the resonance and are scaled up for clarity. Adapted from [137] (CC BY 4.0).

5.4.2 *Mode Characterization*

To provide further evidence of the topologically protected edge resonances, we compare the longitudinal and rotational displacement amplitudes of the individual microstructure plates at the resonance frequency to corresponding FEM calculations. From the measured time-harmonic displacements, the phase lags between the plates can be derived as well. The results for the top-edge resonance are shown in Figure 5.12. As the resonances correspond to standing waves along the metamaterial beam, the individual plates oscillate either in phase or in counterphase. Both the measured amplitude ratios and phase relations are in good agreement with the FEM calculations. The same holds true for the bottom-edge resonance, as shown in Figure 5.13.

Only the absolute amplitudes values obtained from measurements and FEM calculations differ by a global factor. Notably, the measured amplitudes are larger than the calculated ones, i.e., by a factor of 1.5 for the bottom-edge resonance. The reason for this could not be tracked down in detail. It is clear that accounting for all damping mechanisms via a fixed imaginary part of complex dynamical Young's modulus is only an approximation. However, FEM calculations that explicitly include the individual, potentially nonlinear damping contributions, such as air damping, are computationally extremely expensive and beyond the scope of this work.
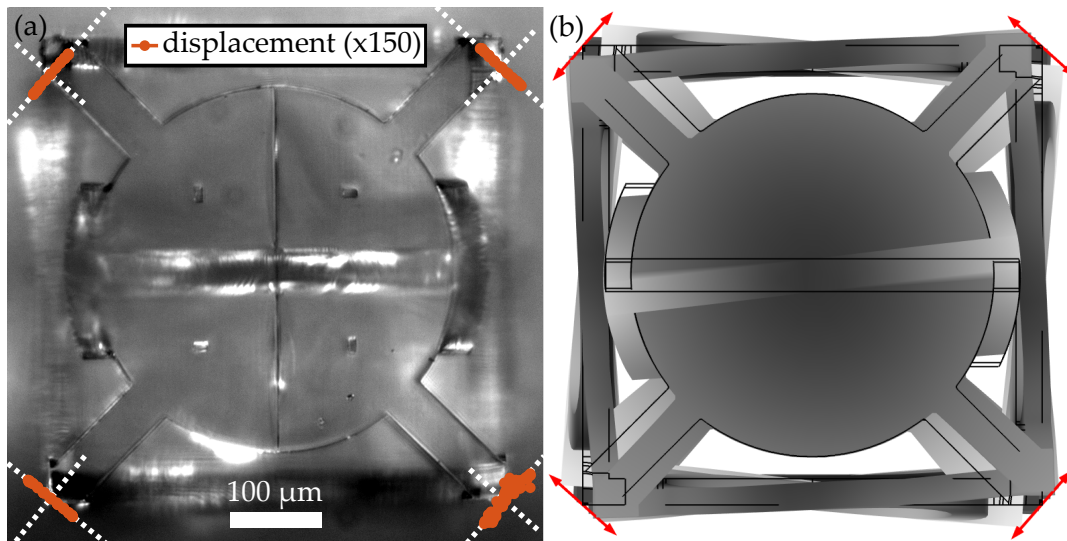
Figure 5.14: (a) Optical micrograph of the fused-silica metamaterial beam in top-view. At the top-edge resonance frequency of 277.85 kHz, the displacements of the four corners were tracked for a time span of three oscillations. The azimuthal motion is clearly visible and agrees with (b) corresponding FEM calculations (red arrows). Adapted from [137] (CC BY 4.0).

In the results presented so far, it was assumed that the horizontal displacements in the side-view images correspond to the projection of the plates' azimuthal motion. Despite the good agreement of the calculated and measured mode shapes, it is worth to check the sample's motion in top-view. The displacement of the top plate for the top-edge resonance is shown in Figure 5.14. The top plate with the mirror attached indeed performs the desired rotational oscillation. Each of the four corners is clearly displaced in azimuthal direction. Thus, the 3D metamaterial beam functions as a resonant converter from longitudinal to rotational motion.

5.5 SUMMARY AND DISCUSSION

In this chapter, I have shown the mechanical characterization of 3D microstructures at ultrasound frequencies. Using an optical-microscopy setup with stroboscopic illumination and subsequent digital image cross-correlation, it has been possible to track the samples' motion from acquired slow-motion videos.

The benefit of fused-silica glass as constituent material compared to polymer has been demonstrated by measuring the resonance curves of micro tuning forks. At frequencies of around 240 kHz, a dynamic Young's modulus of $E_{\mathrm{poly}} = 4.90\,(\pm 0.12)\,\mathrm{GPa}$ and a quality factor of $Q = 22$ have been obtained for polymer. In contrast, the fused-silica material results in a much higher stiffness with $E_{\mathrm{silica}} = 70.8\,(\pm 2.7)\,\mathrm{GPa}$ and the corresponding tuning-fork resonances exhibit quality factors of more than $Q = 17000$ under vacuum. Furthermore, I have shown that the quality factors of fused-silica structures at ambient conditions are limited by air damping. Still, the quality factors are more than two orders of magnitude larger as compared to the polymer tuning forks at the same conditions.

The measurements on the 3D chiral topological fused-silica metamaterial beam have verified the existence of the aimed-at topological twist edge resonances at both ends of the beam. The frequencies of around 262 kHz and 278 kHz of the two localized resonances are within the expected band gap of a corresponding infinite metamaterial structure. A top-edge resonance's quality factor of $Q = 2850$ has been obtained at ambient conditions. The associated enhancement from longitudinal excitation to rotational (azimuthal) oscillation at the top is almost 200. The potential application of a 3D chiral metamaterial beam as a resonant mechanical laser-beam scanner will be discussed in the next chapter.

Altogether, the characterization of the emerging edge resonances and the comparison to corresponding FEM calculation confirms both the metamaterial beam design procedure of chapter 3 and the high quality of the fused-silica 3D structures fabricated along the lines of chapter 4. Also, the good agreement between calculated and measured absolute frequencies validates the derived dynamical Young's modulus of fused-silica. The only significant discrepancy between measurement and FEM calculation are the absolute values of the displacement amplitudes. More sophisticated FEM calculations would be necessary to account explicitly for the individual damping mechanisms, especially for air damping. Thereby, the residual discrepancy could be explained and eliminated. However, such FEM calculations are computationally extremely expensive and beyond the scope of this thesis.

While a pronounced amplitude enhancement has been obtained for all fused-silica microstructures, the achievable maximum absolute amplitudes could not be investigated systematically. The used actuation amplitudes are far below the limits of the experimental setup. The driving voltage of 0.1 V corresponding to around 1 nm actuation amplitude at a frequency of 250 kHz could be increased by

at least a factor of 80 without damaging the piezoelectric transducer. However, the large induced strains and stresses within the structure would lead to failure and damage to the microstructures. A qualitative estimation for the feasible maximum displacements has been given by the fused-silica micro tuning fork experiments. There, the displacement of the tuning fork's tips has been in the order of the prongs' width.

For the smaller actuation amplitudes that have been used otherwise, i.e., for the frequency sweeps, the microstructures showed a good long-time stability. During the whole characterization procedure, the 3D chiral metamaterial beams have been actuated for a time span of around one hour, corresponding to more than a hundred million oscillations. Within this time, no changes have been observed in the mechanical response and the associated resonance frequencies. This indicates that a long-term actuation of the fabricated fused-silica 3D microstructures is possible.

6

Toward a Functional Laser-Beam Scanner

The 3D fused-silica metamaterial beam presented in the last chapters can be understood as a proof of principle to generate robust edge resonances that convert longitudinal to rotational oscillations. Of course, a resonant mechanical laser-beam scanner which functions in practice requires a more careful design. As stated earlier, it is not within the scope of this work to engineer a ready-to-use device. Still, I will briefly discuss an alternative 3D structure that is refined with respect to its application, as shown in Figure 6.1. Also, I will show experiments on such a structure and discuss its performance.
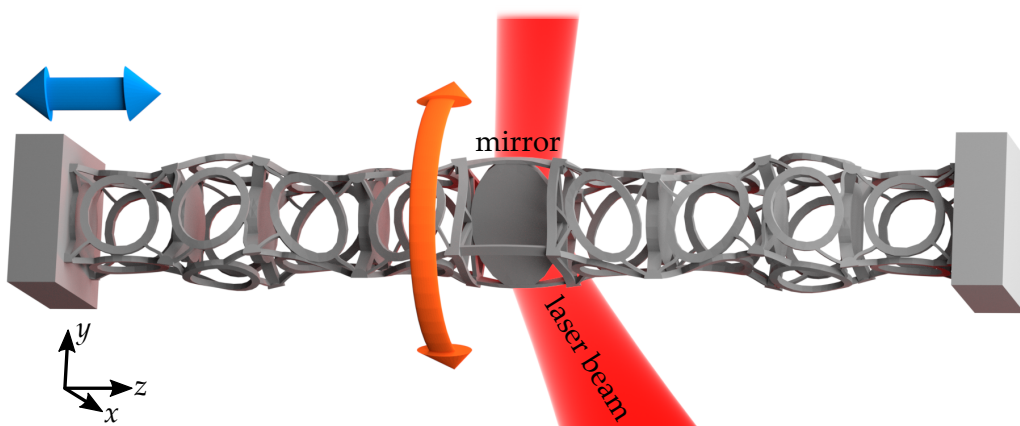

Figure 6.1: Refined design with a two-sided support to reduce mirror warping. The elliptical mirror is optimized for an angle of incidence of 45° of the laser beam. The structure can be excited longitudinally at one end (blue arrow), while the opposite end is kept fixed.

Figure 6.2: FEM calculations on mirror warping. The color indicates the modulus of the structure's local angle of rotation around the z-axis. (a) Design with one-sided support. In resonant operation, the mirror plate warps significantly, as shown by the inhomogeneous coloring. For an exemplary rotation angle amplitude of $\theta_{\mathrm{mech}} = 10°$ averaged over the mirror plate, the local rotation varies by more than $\pm 2°$. (b) Refined design with two-sided support. The variation is reduced to less than $\pm 0.5°$. In contrast to (a), the warping can conceptually be reduced further by engineering additional support structures.
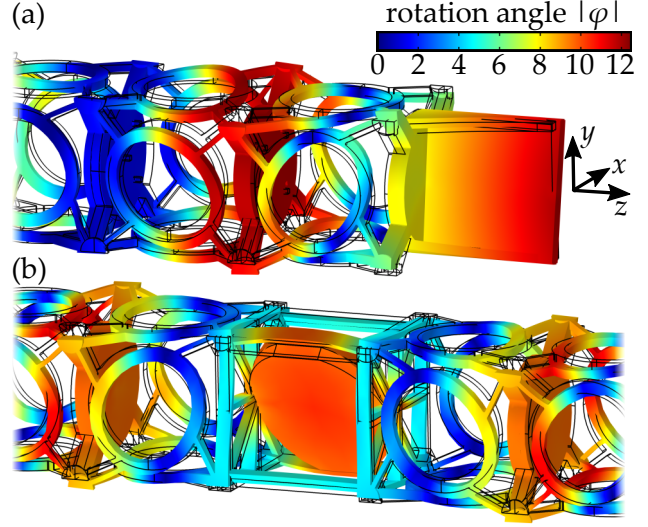
6.1 REQUIREMENTS

The design objective for a high-frequency resonant laser-beam scanner is to scan a laser spot across as many points in space as possible in a given time. This objective is captured in the figure of merit [189]

$$\mathrm{FoM} = D_{\mathrm{mirror}} \cdot f_{\mathrm{res}} \cdot \theta_{\mathrm{opt}}, \tag{6.1}$$

with the mirror diameter D_{mirror}, the frequency f_{res} in resonant operation, and the full optical scan angle θ_{opt}. In reflection mode, this angle corresponds to four times the mechanical rotation angle amplitude θ_{mech} of the mirror plate. To maintain a diffraction-limited laser spot, the maximum mirror deformation δ_{surf} has to be small compared to laser's wavelength λ, i.e., $\delta_{\mathrm{surf}} < \lambda/10$. High-performing resonant 1D micro-electronic-mechanical-system (MEMS) scanners usually reach figures of merit from 500 to around 3000 mm kHz ° [189]. As the frequencies of a metamaterial beam's eigenmodes scale inversely proportional to is global size, the first two factors in equation 6.1 stay constant upon an overall scaling of the structure. One way to increase the operation frequency and thus the FoM is to realize the metamaterial structure out of a highly stiff material. This objective has been fulfilled by using fused-silica as constituent material. In terms of the design, the main challenge for a high-frequency laser-beam scanner is to minimize deformations and warping of the mirror surface upon rotation, while keeping the optical scan angle θ_{opt} as large as possible. As illustrated in Figure 6.2(a), the mirror plane will not undergo a uniform rotation for the metamaterial beam
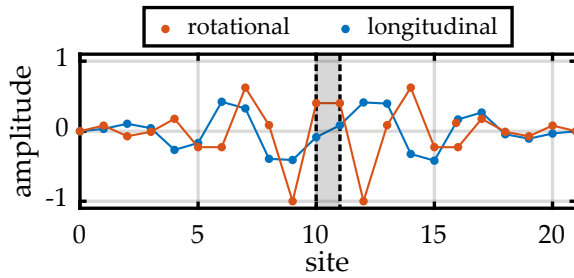
Figure 6.3: Coupled mass-spring model for the two-sided support design, exemplary for 20 sites and both ends fixed. The mode exhibits the desired symmetric rotation at the two sides of the mirror (dashed black lines).

discussed in the last chapters. In contrast, it exhibits a systematic torsion along the z-axis which deforms the mirror. This torsion is a result of the one-sided support of the mirror combined with its own inertia. When the mirror's bottom plate is driven time-harmonically, the mirror's top will always exhibit a phase lag when operating in a resonant mode. As the mirror itself has a finite stiffness, it will unavoidably warp to a certain extent.
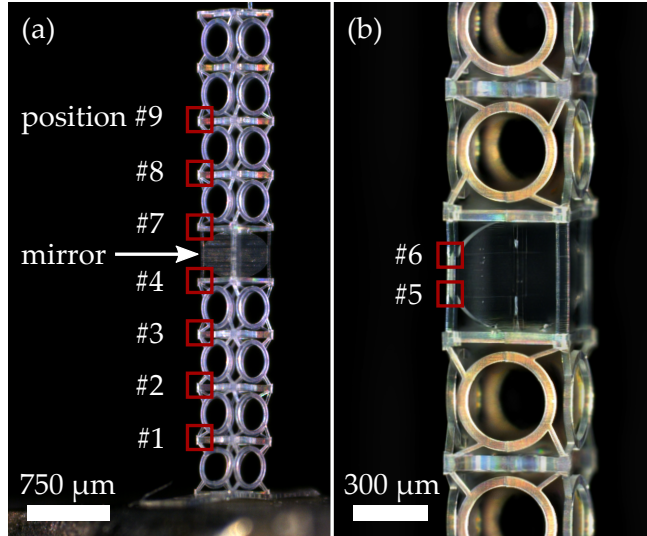
6.2 Two-Sided Mirror-Support Design

Figure 6.2(b) illustrates that the warping can be reduced by supporting the mirror symmetrically on both sides. This design principle was worked out together with Steven Kraus within the scope of his bachelor's thesis. To obtain a symmetric rotational mode, the metamaterial beam structure is mirrored with respect to the center of the mirror plate. Thereby, the chirality of the cells situated right from the mirror is flipped as compared to those situated on the left side. A related design was also used for static twist experiments on chiral metamaterials [15].

Mass-Spring Model

The two-sided support design is described by an adapted version of the finite coupled SSH model as in equation 3.10. The chirality flip of half of the cells corresponds to a sign inversion of the associated chiral coupling constants. The mirror is taken into account by a larger mass and moment of inertia, $m_c = 1.5m$ and $j_c = 1.5j$, of its two support plates. The effective coupling constants of the cell itself are set to $D_c = 2D_1$, $A_c = A_1$, and $B_c = 0$. Notably, the arising symmetric rotational mode, shown in Figure 6.3 must not be understood as a boundary mode between two domains of different topological phase, as the beams on both sides of the mirror are in the same topological phase. In fact, the mode is a symmetric superposition of two coupled edge modes emerging at the quasi-fixed ends imposed by the center-mirror.

Figure 6.4: Optical micrographs of a fused-silica metamaterial beam with two-sided support of the mirror plate. (a) The sample's motion is tracked at the corners of horizontal plates and (b) at two additional positions at the elliptical mirror plate (without reflective coating). Due to the large aspect ratio of the microstructure, the two upmost plates cannot be tracked.

Metamaterial Beam

In addition to the two-sided support design, the mirror shape is optimized to increase its effective diameter while reducing its weight. By the elliptical shape, the mirror's projection is circular when illuminated under an angle of $45°$. Hence, in operation, the laser-beam enters at one face of the cube cell and is reflected under $90°$, superimposed by a time-harmonic deflection with a full scan angle of θ_{opt}. In analogy to section 3.4.3, the beam length is optimized with respect to the rotational amplitude enhancement in the presence of damping. Notably, for the resulting configuration with only four cube cells on each side of the mirror, the spatial decoupling of the mirror with respect to its surrounding is not given anymore. Nevertheless, the design still guarantees a certain robustness of the rotational mode and its eigenfrequency with respect to variations of the mirror cell.

6.3 Ultrasound Experiments

A fused-silica 3D microstructure following the above design is shown in Figure 6.4 with the relevant positions to be tracked. The structure was fabricated via helium-assisted microcasting using Glassomer L50 and thermally treated in upside-down position (cf. Fig 4.11).

To demonstrate the operation principle, it is sufficient to excite the 3D microstructure as before without fixing the upper end. The measured time-harmonic longitudinal and rotational displacements at the desired resonance are shown in Figure 6.5. The resonance exhibits the aimed-at symmetric rotation of the mirror support at both sides.
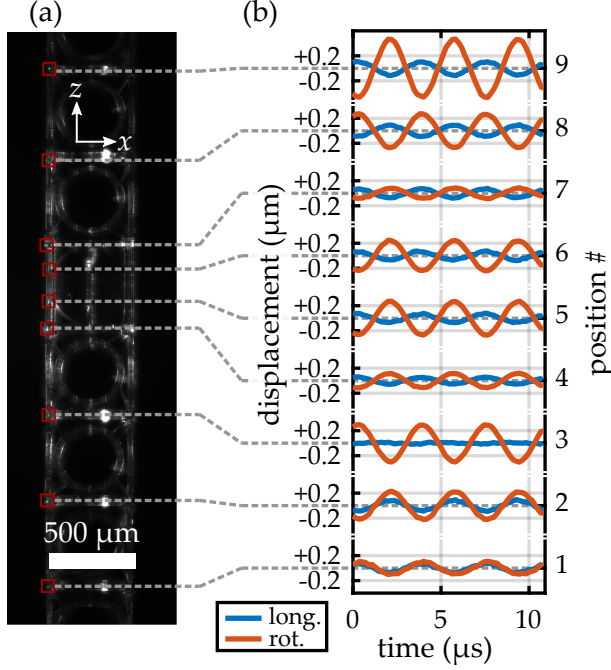
Figure 6.5: (a) Optical micrograph of the structure with two-sided support as acquired in the experimental setup. The tracked ROI are marked by the small red boxes. (b) Measured longitudinal and rotational displacements at the resonance frequency of around 275 kHz. The rotational motion at the mirror support (positions #4 and #7) and the mirror itself (positions #5 and #6) is symmetric, confirming the design objective.

6.4 SCANNING PERFORMANCE AND DISCUSSION

From the figures of merit of up to around FoM $= 3000 \, \text{mm} \, \text{kHz}^\circ$ reported for resonant mechanical 1D laser-beam scanners [189], we can estimate the performance of the realized refined 3D chiral metamaterial beam. To reach this large FoM according to equation 6.1, the structure with its mirror diameter in projection of around $D_{\text{mirror}} = 0.5 \, \text{mm}$ and a resonance frequency of $f_{\text{res}} = 275 \, \text{kHz}$ would have to provide a mechanical rotation amplitude of $\theta_{\text{mech}} = \theta_{\text{opt}}/4 = 5.5°$. As for the metamaterial beams in the last chapter, the limit for the maximum amplitudes was not tested to avoid potential damage to the structures. The small azimuthal amplitudes of $0.2 \, \mu\text{m}$ shown in Figure 6.5 correspond to a mirror plate rotation of only $\theta_{\text{mech}} = 0.03°$. While the maximum displacements observed for fused-silica tuning forks (cf. Fig 5.7) look promising, large FoM are most probably out of reach for the current fused-silica metamaterial beam. Here, metal as constituent material could help to achieve larger deformations and thus larger rotation angles without structure damage.

A second issue that has not been discussed so far is the quality of the fabricated mirror plane. As a result of the microcast's surface quality (cf. Fig. 4.5), the mirror surface exhibits a roughness which is large as compared to the wavelength of visible light. This problem has to be overcome by adapting the 3D laser printing parameters while avoiding a too pronounced proximity effect. As an alternative route, the 3D microstructure could be designed with only a frame holder. A

suitable planar reflective plate could then be attached to the microstructure after the fabrication process.

The above discussion clearly shows that the engineering of a functional resonant mechanical laser-beam scanner requires further investigation. Still, the utilization of a 3D chiral microstructure with a protected twist edge mode can offer advantages over current design approaches. By to the fixation of the resonance frequency via the topological protection it is possible to maintain an operation at high frequencies even for large mirrors. Additionally, the opportunity to design 3D microstructures allows for advanced support architectures around the mirror plate. Thereby, the compensation of mirror warping could be addressed more thoroughly as compared to conventional 2D (planar) scanner designs [190].

7 Chapter 7
Conclusion and Outlook

In this thesis, I have implemented topological effects on the basis of 3D chiral mechanical metamaterials. Inspired by a topological prototype model, I have designed a metamaterial beam that exhibits topologically protected twist edge resonances. To validate my theoretical findings, I have successfully realized corresponding metamaterial microstructures out of fused-silica glass and characterized the emerging high quality-factor topological resonances via experiments at ultrasound frequencies.

In **chapter** 2, I have introduced the basics of topological band theory. The concepts of topological phases, topological invariants, and the bulk-boundary correspondence of topological insulators have been established. In this context, I have discussed the role of symmetry for the classification of topological phases. The Zak phase has been introduced as the relevant topological invariant for 1D periodic systems. In the following, I have focused on a diatomic 1D mass-spring model, i.e., the mechanical analog of the topological Su-Schrieffer-Heeger model. I have identified the model's symmetries required for the formation of distinct topological phases and I have shown the emergence of a topologically nontrivial band gap and associated protected edge modes. Thereby, the peculiar property of the Su-Schrieffer-Heeger, namely its dependence on the boundary termination, has been revealed. With regard to the design and realization of a topological metamaterial, I have discussed the influence of damping and recapitulated the basics of continuum mechanics.

The design route for a chiral topological metamaterial has described shown in **chapter** 3. After a short introduction on metamaterials in general, I have explained the working principle of a chiral cubic metamaterial cell, namely its push-to-twist mechanism. Subsequently, the aim of combining chirality and topology to create topologically protected twist edge modes has been formulated. It has been pointed out that such modes allow for a resonant conversion from longitudinal to rotational motion and thereby serve to realize a resonant mechanical laser-beam scanner. Therefore, a proof-of-principle design has been presented. A chiral

metamaterial beam can be actuated in axial direction at one end by a piezoelectric transducer. Thereby, it evanescently excites a twist edge resonance at the other end, leading to the rotation of an attached mirror.

The starting point for the design has been the diatomic Su-Schrieffer-Heeger model. By mapping a chiral metamaterial beam with alternating cube cells to an effective mass-spring model, I have derived a chirally coupled Su-Schrieffer-Heeger model for the system's longitudinal and rotational degrees of freedom. Along the lines of chapter 2, I have analyzed the symmetry and topological invariant of the coupled model. A quantized Zak phase and thereby also distinct topological phases have been found in the presence of formal bosonic time-reversal symmetry and an additional mirror symmetry. I have shown that a 1D topological band gap emerges for the coupled mass-spring model due to an avoided crossing of its bands. By the calculation of topological phase diagrams, it has been found that the topological nontriviality of the band gap is independent of the boundary termination within a large parameter regime. This is in strong contrast to the ordinary Su-Schrieffer-Heeger model. I have verified the existence of longitudinal-rotational edge modes by calculations on a finite coupled model. As a result of the dependence on a mirror symmetry, the bulk-boundary correspondence is only preserved in the limit of a quasi-fixed end of the mass-spring system. Thereby, I have concluded that adding mass to the end of a system, such as the mirror of a potential laser-beam scanner, even stabilizes the frequency and localization of the topological edge modes. This is the topological mode protection that I have made use of in the following.

Derived from the findings of the mass-spring model, I have presented the design of the aimed-at chiral topological metamaterial beam. The design challenges for the 3D structure have briefly discussed. Finally, the expected emergence of a 1D topological band gap and the associated protected twist edge modes has been confirmed by finite-element method calculations. I have shown that material quality factors of $Q = 2000$ and more are required to obtain a pronounced enhancement from a longitudinal excitation to a rotational motion at the metamaterial beam's opposite ends.

In **chapter** 4, I have introduced the process for the fabrication of 3D fused-silica glass microstructures. This process uses a commercial glass nanocomposite and two-photon 3D laser printing of polymeric microcasts. I have presented the novel helium-assisted microcasting approach that has been developed in the course of my work. By this approach, it is possible to fill the glass nanocomposite into the polymer casts in a controlled and reliable manner. On the basis of chiral metamaterial beams, it has been demonstrated that the overall fabrication process is suitable to fabricate complex and delicate 3D glass microstructures of high quality. I have shown scanning-electron-micrographs and optical micrographs of corresponding structures after thermal debinding and after final sintering. The

proximity effect has been identified as limiting factor in terms of the achievable feature size of the 3D structures. The surface roughness of the final fused-silica samples is determined by the quality of the 3D laser-printed polymer microcast. A decisive strength of the developed fabrication process is its transferability to other constituent materials. As proof of principle, 3D microstructures out of indium-tin-oxide and silver have been presented.

Chapter 5 comprises the experimental validation of the designed chiral metamaterial and its topological twist edge resonances. I have introduced the optical microscopy setup that uses a stroboscopic illumination at ultrasound frequencies to acquire slow motion videos of piezo-actuated microstructures. Via digital image cross-correlation, the displacement of the samples can be tracked at characteristic positions.

The material properties of fused silica and polymer have been characterized by the resonance curves of micro tuning forks. It has been found that fused silica has a dynamic Young's modulus of $E_{\mathrm{silica}} = 70.8\,(\pm 2.7)\,\mathrm{GPa}$ at frequencies of around $240\,\mathrm{kHz}$. This material stiffness is almost a factor of 15 larger as compared to 3D laser-printed polymer. Even more importantly, I showed that the mechanical quality factor of polymer tuning fork resonances is limited to values of $Q = 22$. In contrast, quality factors as large as $Q = 17000$ have been obtained for fused-silica tuning forks under vacuum. Pressure sweeps have revealed that air damping is the dominant loss mechanism, such that the quality factors are reduced to around $Q = 3000$ at ambient conditions. This value is still more than two orders of magnitude larger as for polymer samples and large enough to expect a pronounced resonant behavior of corresponding metamaterial beam edge modes.

Indeed, topologically protected twist edge resonances have been detected by the measurements on a fused-silica chiral metamaterial beam. The resonance frequencies of around $270\,\mathrm{kHz}$ lie within the expected topological band gap of an infinite beam and are localized to the two opposite ends. The twist edge resonance that makes the attached mirror plate rotate has shown a quality factor of $Q = 2850$ and an enhancement factor from longitudinal to rotational (azimuthal) motion of almost 200. Both the mode shape and resonance frequencies are in good agreement with corresponding finite-element method calculations. This confirms the high quality of the fabricated glass 3D microstructures.

An aspect that has not been investigated in detail is the contribution of specific loss mechanisms to the overall determined quality factors and absolute amplitudes. Apart from material and air damping, anchoring losses have been identified as potential cause for damping. However, a quantitative discussion of such effects has been beyond the scope of this work.

In **chapter** 6, I have given an brief outlook toward the realization of a functional mechanical laser-beam scanner. After discussing the requirements and a common figure of merit for such a device, I have presented a refined structure design and corresponding measurements of its actuation. I have concluded that much higher absolute rotation amplitudes are required for a performant laser-beam scanner, which potentially cause structure damage. However, the design and fabrication of 3D microstructures has also been identified as an opportunity for advanced laser-beam scanner designs.

OUTLOOK

The core achievement of this work has been the realization of topological resonances in fused silica metamaterials, eluding the material damping which is predominant in common 3D laser-printed polymer microstructures. While a lot of attention is still drawn to the design of mechanical metamaterials with exotic static properties [114], the presented results encourage to explore exceptional dynamic and resonant metamaterial mechanisms in depth as well. Interestingly, topological protection was realized in plenty of phononic systems [8]. However, in most cases the apparent advantages of such systems, such as the utilization of robust wave guides, are wiped out by dissipation losses. Here, high-stiffness and low-loss microstructures will help to exploit the potential of one-, two-, and three-dimensional topological systems. Following recent advances [191], the high quality factors could even bring quantum entanglement of (topological) mechanical resonances in 3D microstructures into reach. For this and other purposes, also the upcoming higher-order topological insulators are of major interest. In these systems, it is possible to induce and couple protected states localized at planes, edges, and points of a single platform. Notably, the extension of the Su-Schrieffer-Heeger model to higher dimensions is one possibility to design such higher-order topological insulators [43, 192].

In contrast to applications that rely on minimizing dissipation, the opening field of non-Hermitian topological systems can make use of damping mechanisms. The potential of such systems was not unveiled in the course of this thesis and should be elaborated in future work. The influence of damping on the topological phases offers the opportunity to design edge modes that are switched on or off in the presence or absence of damping. A corresponding structure could act as a transistor for elastic waves, that is a device that transmits a wave in the presence of damping, e.g., as exposed to air, but is without edge states and hence insulating otherwise.

The fabrication process involving the helium-assisted microcasting as developed within this work invites to investigate the potential of microstructures of materials other than polymer and fused silica. The transferability to materials such as semiconductors and metals paves the way to complex 3D microelectronic devices, such as compact 3D microactuators and microsensors, or 3D photodiode arrays. Via ceramics, also piezoelectric or even superconducting 3D metamaterials are in reach.

A

APPENDIX

A.1 CHERN NUMBER

In the integer quantum Hall effect, one has to consider the case of a 2D band structure with the Chern number as a topological invariant. In 2D, the reciprocal space can be represented by the surface of a torus to fulfill the periodicity condition for the two components of the wave vector $\mathbf{k}$. Equation 2.12 for the Berry phase can now be transformed from a contour integral to a surface integral via the Stokes theorem, obtaining the Berry flux

$$\phi_n^{\mathrm{B}} = \oiint_S F_n(\mathbf{k})\mathrm{d}\mathbf{S}, \tag{A.1}$$

where the so-called Berry curvature is the curl of the Berry connection, $F_n(\mathbf{k}) = \nabla_{\mathbf{k}} \times \mathbf{A}_n$, which is a pseudoscalar in 2D [34]. Here, the Berry flux is integrated over the whole reciprocal space, meaning the surface $\mathcal{S}$ is the closed surface of the Brillouin zone torus. Interestingly, this means that the associated loop $\mathcal{C}$ of the contour integral in equation 2.12 is contracted to a point and vanishes, which is not the case for the Zak phase in 1D [34]. Indeed, in the topologically trivial phase, the Berry flux of a 2D system has to be zero. However, in the nontrivial phase, the phase of the Bloch eigenstates are not orientable over the whole base space, as it is the case for the surface of the Möbius strip. Stokes theorem is not strictly applicable anymore and occurring phase vortices in the Berry curvature can lead to Berry fluxes discretized to integer multiples of 2π, where the integer is called the *Chern number* [31]. It was shown by Berry, that such phase vortices arise due to the virtual interaction of eigenstates of different bands of the band structure [32]. The bands exchange phase and thereby wind up in the sense of the Möbius strip.

A.2 Pauli Matrices

The identity matrix σ_0 and the Pauli matrices σ_x, σ_y, σ_z are given by

$$\sigma_0 = \begin{pmatrix} 1 & 0 \\ 0 & 1 \end{pmatrix}, \quad \sigma_x = \begin{pmatrix} 0 & 1 \\ 1 & 0 \end{pmatrix}, \quad \sigma_y = \begin{pmatrix} 0 & -i \\ i & 0 \end{pmatrix}, \quad \sigma_z = \begin{pmatrix} 1 & 0 \\ 0 & -1 \end{pmatrix}. \tag{A.2}$$

A.3 Zak Phase Calculation via Band Inversion

The following proof goes along the lines of personal notes of Jörg Schmalian [69]. It shows that the Zak phase of a band n is determined by the parity eigenvalues $p_0^{(n)}$ and $p_\pi^{(n)}$ at the two high symmetry points in the Brillouin zone. The proof holds true for systems obeying formal time-reversal symmetry $\hat{T}$ and an additional parity symmetry $\hat{P}$, as observed for both the SSH model in section 2.3 and the coupled SSH model in section 3.3.

We consider the phase factor $C_N^{(n)}$ obtained from the Zak phase γ_n for $N = 2\pi/\mathrm{d}k$ discretized wave numbers $k_i = -\pi + i\,\mathrm{d}k$, as in equation 2.14. We use a lattice constant of $a = 1$ for convenience and get

$$C_N^{(n)} = \mathrm{e}^{-i\gamma_n} = \prod_{k_i=-\pi}^{\pi-\mathrm{d}k} \langle u_n(k_i) | u_n(k_i + \mathrm{d}k) \rangle. \tag{A.3}$$

From equation 2.27 we know that parity operator $\hat{P}$ links eigenstates of wave numbers with opposite sign, such that we can write

$$|u_n(-k_i)\rangle = \mathrm{e}^{i\phi(k_i)} \hat{P} |u_n(k_i)\rangle, \tag{A.4}$$

where $\phi(k_i)$ is some wave-number-dependent phase [43]. Additionally, as stated in equation 2.33, $\hat{P}$ is an eigenoperator for the two states at the high symmetry points $k = 0$ and $k = \pi$. To make use of this, we decompose the product in equation A.3 into two parts containing only negative and only positive wave numbers, and the two factors containing the high symmetry points of the negative part:

$$
\begin{aligned}
C_N^{(n)} = {} & \langle u_n(\pi) | u_n(-\pi + \mathrm{d}k) \rangle \langle u_n(-\mathrm{d}k) | u_n(0) \rangle \\
& \cdot \prod_{k_i=-\pi+\mathrm{d}k}^{-2\mathrm{d}k} \langle u_n(k_i) | u_n(k_i + \mathrm{d}k) \rangle \cdot \prod_{k_i=0}^{\pi-\mathrm{d}k} \langle u_n(k_i) | u_n(k_i + \mathrm{d}k) \rangle.
\end{aligned}
\tag{A.5}
$$

In the first factor, we used that the eigenstate at $k = -\pi$ is equivalent to the one at $k = +\pi$. By equation A.4, all eigenstates at negative wave numbers can be

transformed to corresponding positive ones. For two neighboring states we get

$$
\begin{aligned}
\langle u_n(-k_i)|u_n(-k_i + \mathrm{d}k)\rangle &= \mathrm{e}^{-\mathrm{i}\phi(k_i)}\mathrm{e}^{\mathrm{i}\phi(k_i - \mathrm{d}k)}\,\langle u_n(k_i)|\hat{P}^2|u_n(k_i - \mathrm{d}k)\rangle \\
&= \mathrm{e}^{-\mathrm{i}\phi(k_i)}\mathrm{e}^{\mathrm{i}\phi(k_i - \mathrm{d}k)}\,\langle u_n(k_i)|u_n(k_i - \mathrm{d}k)\rangle, \qquad (\mathrm{A.6}) \\
&= \mathrm{e}^{-\mathrm{i}\phi(k_i)}\mathrm{e}^{\mathrm{i}\phi(k_i - \mathrm{d}k)}\,\langle u_n(k_{i-1} + \mathrm{d}k)|u_n(k_{i-1})\rangle,
\end{aligned}
$$

with $\hat{P}^2 = 1$. When plugging this into equation A.5, all phase factors of the eigenstates from $k = -\pi + \mathrm{d}k$ to $k = -\mathrm{d}k$ vanish, as each emerges once from a bra- and once from a ket-state and thus with opposite sign. At $k = \pi$ and $k = 0$, however, the states do not need to be transformed, such that we are left with two factors containing the parity operator $\hat{P}$:

$$
\begin{aligned}
C_N^{(n)} = &\langle u_n(\pi)|\hat{P}|u_n(\pi - \mathrm{d}k)\rangle\,\langle u_n(\mathrm{d}k)|\hat{P}|u_n(0)\rangle \\
&\cdot \prod_{k_i=\mathrm{d}k}^{\pi-2\mathrm{d}k}\langle u_n(k_i + \mathrm{d}k)|u_n(k_i)\rangle \cdot \prod_{k_i=0}^{\pi-\mathrm{d}k}\langle u_n(k_i)|u_n(k_i + \mathrm{d}k)\rangle.
\end{aligned} \qquad (\mathrm{A.7})
$$

Now the remaining two parity operators can be applied to the high symmetry states $\langle u_n(\pi)|$ and $|u_n(0)\rangle$, yielding the real-valued parity eigenvalues $p_\pi^{(n)}$ and $p_0^{(n)}$ according to equation 2.33. The residual factors can be condensed as

$$
C_N^{(n)} = p_\pi^{(n)} p_0^{(n)} \prod_{k_i=0}^{\pi-\mathrm{d}k}|\langle u_n(k_i)|u_n(k_i + \mathrm{d}k)\rangle|^2. \qquad (\mathrm{A.8})
$$

Assuming a fine discretization $\mathrm{d}k$, the terms containing the scalar products of neighboring eigenstates are all close to unity, such that their product will also converge to unity:

$$
C^{(n)} = \lim_{N\to\infty} C_N^{(n)} = p_\pi^{(n)} p_0^{(n)}. \qquad (\mathrm{A.9})
$$

Thus, the phase factor $C^{(n)}$ accumulated once across the first Brillouin zone is solely determined by the two parity eigenvalues which can both assume values of ± 1. For equal parity eigenvalues, the band n is topologically trivial with $C^{(n)} = 1$ and has a Zak phase of $\gamma_n = 0$ according to equation A.3. For different parity values, corresponding to a so-called band inversion, the phase factor is $C^{(n)} = -1$ and the associated Zak phase is $\gamma_n = \pi$. Thus, the Zak phase can be directly expressed in terms of the parity values:

$$
\gamma_n = \frac{\pi}{2}\left(1 - p_0^{(n)} p_\pi^{(n)}\right). \qquad (\mathrm{A.10})
$$

A.4 Phase Convention for Non-Hermitian Systems

To avoid a spoiled Zak phase in non-Hermitian systems with arbitrary imaginary parts of the coupling constants, the eigenvectors have to be normalized appropriately. As found by Steven Kraus, the raw numerical left and right eigenvectors, $\left\langle \mathbf{u}'_{n,\mathrm{L}} \right|$ and $\left| \mathbf{u}'_{n,\mathrm{R}} \right\rangle$, respectively, can be transformed as follows:

$$
\langle \mathbf{u}_{n,\mathrm{L}} | = \frac{\left\langle \mathbf{u}'_{n,\mathrm{L}} \right|}{\left\| \mathbf{u}'_{n,\mathrm{L}} \right\rangle \right\|} \cdot \frac{\mathrm{e}^{\frac{\mathrm{i}(-\varphi_\mathrm{L} + \varphi_\mathrm{R} + \varphi_\mathrm{LR})}{2}}}{\sqrt{\left| \left\langle \mathbf{u}'_{m,\mathrm{L}} \middle| \mathbf{u}'_{n,\mathrm{R}} \right\rangle \right|}} \quad ,
$$

$$
| \mathbf{u}_{n,\mathrm{R}} \rangle = \frac{\left| \mathbf{u}'_{n,\mathrm{R}} \right\rangle}{\left\| \mathbf{u}'_{n,\mathrm{R}} \right\rangle \right\|} \cdot \frac{\mathrm{e}^{\frac{\mathrm{i}(-\varphi_\mathrm{L} + \varphi_\mathrm{R} - \varphi_\mathrm{LR})}{2}}}{\sqrt{\left| \left\langle \mathbf{u}'_{m,\mathrm{L}} \middle| \mathbf{u}'_{n,\mathrm{R}} \right\rangle \right|}} \quad ,
$$

(A.11)

with the phase angles

$$
\varphi_\mathrm{LR} = \arg \left(\left\langle \mathbf{u}'_{m,\mathrm{L}} \middle| \mathbf{u}'_{n,\mathrm{R}} \right\rangle \right), \quad \varphi_\mathrm{L} = \arg \left(u'^{1}_{n,\mathrm{L}} \right), \quad \varphi_\mathrm{R} = \arg \left(u'^{1}_{n,\mathrm{R}} \right). \tag{A.12}
$$

Here, $u'^{1}_{n,\mathrm{L}}$ and $u'^{1}_{n,\mathrm{R}}$ are the first components of the raw eigenvectors in ket-notation.

A.5 Finite-Element Method Calculations

To provide an idea how a continuum mechanics problem can be transformed into a discretized version, the key steps of the finite-element method are shortly summarized along the lines of references [100] and [103].

For an exact solution, the equation of motion derived in section 2.5.1 has to be fulfilled at every point of the material body domain R. This condition can be eased by writing the equation for each component i of the displacement u_i in integral form:

$$
\int_R \left(\rho \frac{\partial^2 u_i}{\partial t^2} - \frac{\partial}{\partial r_j} \sigma_{ij} - f_i \right) \delta v_i \mathrm{d}V = 0. \tag{A.13}
$$

Of course, only requiring the complete integral to be zero instead of the integrand itself would be far off the actual problem to be solved. Thus, the integrands are multiplied by a test function δv_i, which can be chosen such that it samples the integral over small domains only. Equation A.13 is called the weak form of the problem. Using the equations of continuum mechanics 2.53 to 2.55 and partial integration, the weak form can be rewritten as

$$
\int_R \rho \frac{\partial^2 u_i}{\partial t^2} \delta v_i \mathrm{d}V + \int_R C_{ijkl} \frac{\partial u_k}{\partial r_i} \frac{\partial \delta v_i}{\partial r_j} \mathrm{d}V - \int_{\partial R} t_i \delta v_i \mathrm{d}S = 0, \tag{A.14}
$$

using Einstein summation convention. For simplicity, the body force field with its components f_i is assumed to be zero. Only forces per unit area t_i acting on the boundary ∂R are taken into account. In the context of mechanics, the above equation corresponds to the principle of virtual work, with the test function δv_i as virtual displacement [100]. As the test function should sample the integral over small domains only, we write both $\delta v_i(\mathbf{r})$ and the displacement field component $u_i(\mathbf{r})$ as a superposition of shape functions $\theta^a(\mathbf{r})$ for each node a,

$$u_i(\mathbf{r}) = \sum_a^N u_i^a \theta^a(\mathbf{r}), \quad \text{and} \quad \delta v_i(\mathbf{r}) = \sum_a^N \delta v_i^a \theta^a(\mathbf{r}). \tag{A.15}$$

Each shape function samples the above integral in its domain around node a and is zero at all other nodes $b \neq a$. In this way, the solution of the partial differential equation at a node a will be directly given by the factor u_i^a, and can be interpolated at some arbitrary point $\mathbf{r}$ between the nodes. Plugging ansatz A.15 into the weak form equation A.14 and require it to hold true for arbitrary δv_i results in

$$M_{ab} \ddot{u}_i^b + K_{aibk} u_k^b - F_i^a = 0, \tag{A.16}$$

$$\text{with} \quad M_{ab} = \int_R \rho \theta^a(\mathbf{r}) \theta^b(\mathbf{r}) \mathrm{d}V,$$

$$K_{aibk} = \int_R C_{ijkl} \frac{\partial \theta^a(\mathbf{r})}{\partial r_j} \frac{\partial \theta^b(\mathbf{r})}{\partial r_l} \mathrm{d}V, \tag{A.17}$$

$$\text{and} \quad F_i^a = \int_{\partial R} t_i \theta^a(\mathbf{r}) \mathrm{d}S.$$

Here, the components of the mass matrix M_{ab}, stiffness matrix K_{aibk}, and force vector F_i^a are known, as they all follow from the problem to be solved, given the defined node positions and shape functions. As the shape functions can be defined in a convenient manner, the partial differentials in equation A.17 can be solved easily. Comparison with section 2.3.5 shows that the resulting problem is similar to a 3D generalization of the finite 1D mass-spring model in the presence of boundary conditions. The mass matrix replaces the point masses and the stiffness matrix accounts for the coupling of the displacements components u_i^a at the individual nodes a. In the case of solid mechanics, only neighboring nodes are connected such that K_{aibk} will be a sparse matrix with only a few off-diagonal entries as in equation 2.38. Solving the whole finite-element problem thus comes down to solving the matrix equation A.16.
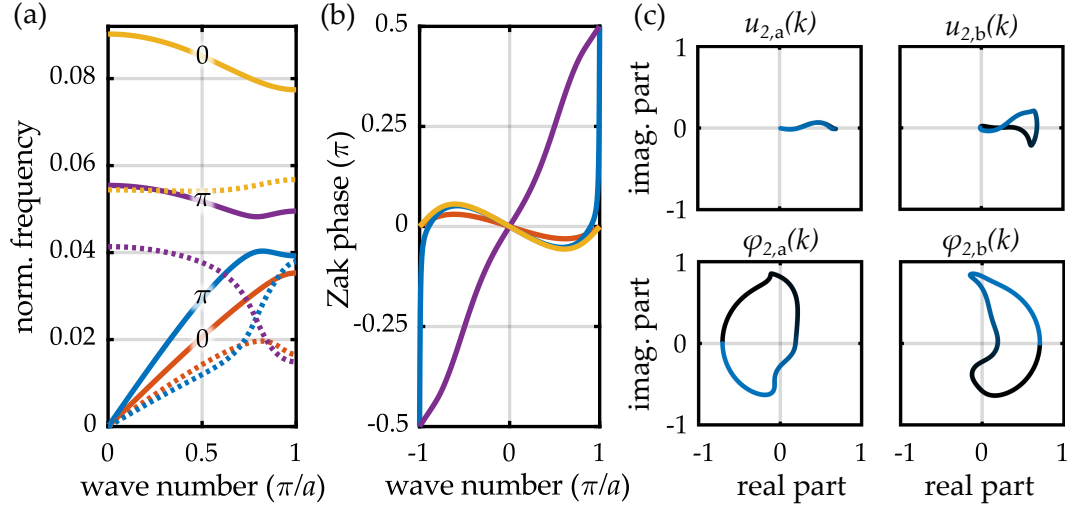
Figure A.1: Non-Hermitian coupled SSH model. The real valued coupling constants of the Hermitian SSH model (cf. Fig. 3.4) were changed to complex constants with arbitrary imaginary parts: $(1 + 0.3\mathrm{i})\tilde{D}_1$, $(1 + 0.1\mathrm{i})\tilde{D}_2$, $(1 + 0.4\mathrm{i})\tilde{A}_1$, $(1 + 0.2\mathrm{i})\tilde{A}_2$, $(1 + 0.05\mathrm{i})\tilde{B}_1$, and $(1 + 0.1\mathrm{i})\tilde{B}_2$. (a) The band structure shows the real parts (solid lines) and imaginary parts (dotted lines) of the bands' frequencies. The imaginary parts are scaled up by a factor of 5 for illustration purposes. The generalized Zak phases are indicated for each band. (b) Evolution of the Zak phase across the first Brillouin zone. As for the Hermitian model, the Zak phases are quantized. (c) Exemplary contours of the four right eigenvector components for the second band, from $k = -\pi$ (black) to $k = +\pi$ (light blue).

A.6 Non-Hermitian Coupled Su-Schrieffer-Heeger Model

The discussion on the band structure and Zak phases of the Hermitian coupled SSH model has been conducted in section 3.3.2. Figure A.1 shows corresponding results for a non-Hermitian version of this model with exemplary imaginary parts for each coupling constant. The generalized Zak phases of each band are calculated according to equation 2.52 using the eigenvector phase convention given in section A.4. The calculations show that the generalized Zak phases stay quantized in the non-Hermitian case. Thereby, also the distinct topological phases stay intact.
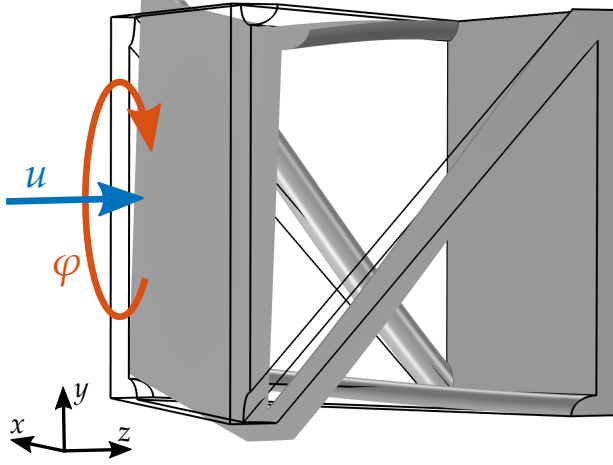
Figure A.2: Alternative uniaxial chiral cube cell. The simple geometry is potentially advantageous for an experimental realization. However, in the dynamic regime, the structure exhibits low-frequency resonances of the connecting beams, which couple with the mixed rotational-longitudinal modes and thereby interfere with the formation of topologically nontrivial bands and band gaps.

A.7 ALTERNATIVE CHIRAL CUBE CELL

An alternative chiral cube cell is shown in Figure A.2. This design goes along several previous publications [132, 138, 139]. It was briefly investigated within this work as potential building block for the chiral topological metamaterial beam but found unsuitable to induce large 1D band gaps for all mode types.

Bibliography

[1] J. Michael Kosterlitz, *Nobel Lecture 2016*, NobelPrize.org, Nobel Prize Outreach AB 2021, (2016) https://www.nobelprize.org/prizes/physics/2016/kosterlitz/lecture/ (visited on 11/19/2021) (cited on page 3).

[2] K. v. Klitzing, G. Dorda, and M. Pepper, "New Method for High-Accuracy Determination of the Fine-Structure Constant Based on Quantized Hall Resistance", Phys. Rev. Lett. 45, 494–497 (1980) (cited on pages 3, 10).

[3] D. J. Thouless, M. Kohmoto, M. P. Nightingale, and M. den Nijs, "Quantized Hall Conductance in a Two-Dimensional Periodic Potential", Phys. Rev. Lett. 49, 405–408 (1982) (cited on pages 3, 10).

[4] M. Z. Hasan and C. L. Kane, "Colloquium : Topological Insulators", Rev. Mod. Phys. 82, 3045–3067 (2010) (cited on pages 3, 11, 16).

[5] A. P. Schnyder, S. Ryu, A. Furusaki, and A. W. W. Ludwig, "Classification of Topological Insulators and Superconductors in Three Spatial Dimensions", Phys. Rev. B 78, 195125 (2008) (cited on pages 3, 16).

[6] L. Lu, J. D. Joannopoulos, and M. Soljačić, "Topological Photonics", Nat. Photon. 8, 821–829 (2014) (cited on pages 3, 8, 16, 18).

[7] R. Süsstrunk and S. D. Huber, "Classification of Topological Phonons in Linear Mechanical Metamaterials", PNAS 113, E4767–E4775 (2016) (cited on pages 3, 17, 18, 23, 30).

[8] F. Zangeneh-Nejad, A. Alù, and R. Fleury, "Topological Wave Insulators: A Review", C. R. Phys. 21, 467–499 (2020) (cited on pages 3, 16, 18, 30, 112).

[9] W. P. Su, J. R. Schrieffer, and A. J. Heeger, "Soliton Excitations in Polyacetylene", Phys. Rev. B 22, 2099–2111 (1980) (cited on pages 4, 18).

[10] M. Kadic, G. W. Milton, M. van Hecke, and M. Wegener, "3D Metamaterials", Nat. Rev. Phys. 1, 198–210 (2019) (cited on pages 4, 42).

[11] X. Zheng, H. Lee, T. H. Weisgraber, M. Shusteff, J. DeOtte, E. B. Duoss, J. D. Kuntz, M. M. Biener, Q. Ge, J. A. Jackson, S. O. Kucheyev, N. X. Fang, and C. M. Spadaccini, "Ultralight, Ultrastiff Mechanical Metamaterials", Science 344, 1373–1377 (2014) (cited on pages 4, 42).

[12] R. V. Craster and S. Guenneau, eds., *Acoustic Metamaterials: Negative Refraction, Imaging, Lensing and Cloaking*, Springer Series in Materials Science (Springer Science+Business Media, Dordrecht, 2013) (cited on pages 4, 18, 42).

[13] Y. Chen, M. Kadic, and M. Wegener, "Roton-like Acoustical Dispersion Relations in 3D Metamaterials", Nat Commun **12**, 3278 (2021) (cited on page 4).

[14] J. A. Iglesias Martínez, M. F. Groß, Y. Chen, T. Frenzel, V. Laude, M. Kadic, and M. Wegener, "Experimental Observation of Roton-like Dispersion Relations in Metamaterials", Sci. Adv. **7**, eabm2189 (2021) (cited on page 4).

[15] T. Frenzel, M. Kadic, and M. Wegener, "Three-Dimensional Mechanical Metamaterials with a Twist", Science **358**, 1072–1074 (2017) (cited on pages 4, 41–45, 58, 69, 105).

[16] T. Frenzel, "On 3D Chiral Mechanical Metamaterials", PhD thesis (Karlsruher Institut für Technologie (KIT), Karlsruhe, 2020) (cited on pages 4, 41–43, 86).

[17] T. Frenzel, J. Köpfler, E. Jung, M. Kadic, and M. Wegener, "Ultrasound Experiments on Acoustical Activity in Chiral Mechanical Metamaterials", Nat. Commun. **10**, 3384 (2019) (cited on pages 4, 41, 43, 69, 86, 89, 91).

[18] H. Eschrig, *Topology and Geometry for Physics* (Springer-Verlag, Berlin Heidelberg, 2011) (cited on page 7).

[19] M. Asorey, "Space, Matter and Topology", Nat. Phys. **12**, 616–618 (2016) (cited on pages 7, 8, 15).

[20] B. Hopkins and R. J. Wilson, "The Truth about Königsberg", Coll. Math. J. **35**, 198–207 (2004) (cited on page 8).

[21] L. Euler, "Solutio Problematis Ad Geometriam Situs Pertinentis", Comment. Acad. Sci. Imp. Petropolitanae **8**, 128–140 (1736) (cited on page 8).

[22] J. E. Greene and A. Lobb, *The Rectangular Peg Problem*, (May 18, 2020) http://arxiv.org/abs/2005.09193 (visited on 10/10/2021) (cited on page 8).

[23] B. Matschke, "A Survey on the Square Peg Problem", Not. Am. Math. Soc. **61**, 346–352 (2014) (cited on page 8).

[24] Y. Aharonov and D. Bohm, "Significance of Electromagnetic Potentials in the Quantum Theory", Phys. Rev. **115**, 485–491 (1959) (cited on page 8).

[25] M. Fruchart and D. Carpentier, "An Introduction to Topological Insulators", C. R. Phys., Topological Insulators / Isolants Topologiques **14**, 779–815 (2013) (cited on pages 8, 9, 12).

[26] J. Köpfler, "On Three-Dimensional Topological Photonic Crystals Exhibiting Weyl Points", MA thesis (Karlsruher Institut für Technologie (KIT), 2017) (cited on pages 8, 10, 13).

[27] C. L. Kane, "Topological Band Theory and the Z2 Invariant", Contemp. Concepts Condens. Matter Sci., Topological Insulators **6**, 3–34 (2013) (cited on pages 8, 11, 12).

[28] M. Nakahara, *Geometry, Topology and Physics*, 2nd ed. (CRC Press, Boca Raton, 2017), 596 pp. (cited on page 9).

[29] B. Simon, "Holonomy, the Quantum Adiabatic Theorem, and Berry's Phase", Phys. Rev. Lett. **51**, 2167–2170 (1983) (cited on pages 10, 11).

[30] J. E. Avron, R. Seiler, and B. Simon, "Homotopy and Quantization in Condensed Matter Physics", Phys. Rev. Lett. **51**, 51–53 (1983) (cited on pages 10, 11).

[31] Y. Hatsugai, "Chern Number and Edge States in the Integer Quantum Hall Effect", Phys. Rev. Lett. **71**, 3697–3700 (1993) (cited on pages 10, 15, 115).

[32] M. V. Berry, "Quantal Phase Factors Accompanying Adiabatic Changes", Proc Phys Soc Lond. Sec A **392**, 45–57 (1984) (cited on pages 11, 13, 14, 115).

[33] B. A. Bernevig, *Topological Insulators and Topological Superconductors* (Princeton University Press, Princeton, 2013), 260 pp. (cited on pages 11, 14).

[34] J. Cayssol and J. N. Fuchs, "Topological and Geometrical Aspects of Band Theory", J. Phys. Mater. **4**, 034007 (2021) (cited on pages 11, 12, 15, 17, 21, 23, 30, 115).

[35] J. K. Asbóth, L. Oroszlány, and A. Pályi, *A Short Course on Topological Insulators: Band Structure and Edge States in One and Two Dimensions*, Lecture Notes in Physics (Springer International Publishing, Basel, 2016) (cited on pages 12–15, 21, 28, 30).

[36] E. Cohen, H. Larocque, F. Bouchard, F. Nejadsattari, Y. Gefen, and E. Karimi, "Geometric Phase from Aharonov–Bohm to Pancharatnam–Berry and Beyond", Nat. Rev. Phys. **1**, 437–449 (2019) (cited on page 13).

[37] J. Zak, "Berry's Phase for Energy Bands in Solids", Phys. Rev. Lett. **62**, 2747–2750 (1989) (cited on page 14).

[38] F. D. M. Haldane, "Model for a Quantum Hall Effect without Landau Levels: Condensed-Matter Realization of the "Parity Anomaly"", Phys. Rev. Lett. **61**, 2015–2018 (1988) (cited on page 16).

[39] C. L. Kane and E. J. Mele, "Quantum Spin Hall Effect in Graphene", Phys. Rev. Lett. **95**, 226801 (2005) (cited on page 16).

[40] C. L. Kane and E. J. Mele, "Z2 Topological Order and the Quantum Spin Hall Effect", Phys. Rev. Lett. **95**, 146802 (2005) (cited on page 16).

[41] M. König, S. Wiedmann, C. Brüne, A. Roth, H. Buhmann, L. W. Molenkamp, X.-L. Qi, and S.-C. Zhang, "Quantum Spin Hall Insulator State in HgTe Quantum Wells", Science **318**, 766–770 (2007) (cited on page 16).

[42] A. Altland and M. R. Zirnbauer, "Nonstandard Symmetry Classes in Mesoscopic Normal-Superconducting Hybrid Structures", Phys. Rev. B **55**, 1142–1161 (1997) (cited on pages 16, 48).

[43] T. L. Hughes, E. Prodan, and B. A. Bernevig, "Inversion-Symmetric Topological Insulators", Phys. Rev. B **83**, 245132 (2011) (cited on pages 17, 26, 112, 116).

[44] L. Fu, "Topological Crystalline Insulators", Phys. Rev. Lett. **106**, 106802 (2011) (cited on pages 17, 30).

[45] C.-K. Chiu and A. P. Schnyder, "Classification of Reflection-Symmetry-Protected Topological Semimetals and Nodal Superconductors", Phys. Rev. B **90**, 205136 (2014) (cited on page 17).

[46] E. Yablonovitch, "Inhibited Spontaneous Emission in Solid-State Physics and Electronics", Phys. Rev. Lett. **58**, 2059–2062 (1987) (cited on page 18).

[47] S. John, "Strong Localization of Photons in Certain Disordered Dielectric Superlattices", Phys. Rev. Lett. **58**, 2486–2489 (1987) (cited on page 18).

[48] J. D. Joannopoulos, R. D. Meade, and J. N. Winn, *Photonic Crystals: Molding the Flow of Light* (Princeton University Press, Princeton, 1995), 156 pp. (cited on page 18).

[49] M. S. Kushwaha, P. Halevi, L. Dobrzynski, and B. Djafari-Rouhani, "Acoustic Band Structure of Periodic Elastic Composites", Phys. Rev. Lett. **71**, 2022–2025 (1993) (cited on page 18).

[50] V. Laude, *Phononic Crystals, Artificial Crystals for Sonic, Acoustic, and Elastic Waves* (De Gruyter, Berlin Boston, 2015) (cited on page 18).

[51] F. D. M. Haldane and S. Raghu, "Possible Realization of Directional Optical Waveguides in Photonic Crystals with Broken Time-Reversal Symmetry", Phys. Rev. Lett. **100**, 013904 (2008) (cited on page 18).

[52] S. Raghu and F. D. M. Haldane, "Analogs of Quantum-Hall-effect Edge States in Photonic Crystals", Phys. Rev. A **78**, 033834 (2008) (cited on page 18).

[53] E. Prodan and C. Prodan, "Topological Phonon Modes and Their Role in Dynamic Instability of Microtubules", Phys. Rev. Lett. **103**, 248101 (2009) (cited on page 18).

[54] Y. Barlas and E. Prodan, "Topological Classification Table Implemented with Classical Passive Metamaterials", Phys. Rev. B **98**, 094310 (2018) (cited on page 18).

[55] A. B. Khanikaev, R. Fleury, S. H. Mousavi, and A. Alù, "Topologically Robust Sound Propagation in an Angular-Momentum-Biased Graphene-like Resonator Lattice", Nat. Commun. **6**, 8260 (2015) (cited on page 18).

[56] Z. Yang, F. Gao, X. Shi, X. Lin, Z. Gao, Y. Chong, and B. Zhang, "Topological Acoustics", Phys. Rev. Lett. **114**, 114301 (2015) (cited on page 18).

[57] A. Souslov, B. C. van Zuiden, D. Bartolo, and V. Vitelli, "Topological Sound in Active-Liquid Metamaterials", Nat. Phys. **13**, 1091–1094 (2017) (cited on page 18).

[58] Y. Ding, Y. Peng, Y. Zhu, X. Fan, J. Yang, B. Liang, X. Zhu, X. Wan, and J. Cheng, "Experimental Demonstration of Acoustic Chern Insulators", Phys. Rev. Lett. **122**, 014302 (2019) (cited on page 18).

[59] Z. Zhang, Y. Tian, Y. Cheng, X. Liu, and J. Christensen, "Experimental Verification of Acoustic Pseudospin Multipoles in a Symmetry-Broken Snowflakelike Topological Insulator", Phys. Rev. B **96**, 241306 (2017) (cited on page 18).

[60] Z.-G. Geng, Y.-G. Peng, Y.-X. Shen, D.-G. Zhao, and X.-F. Zhu, "Topologically Protected Edge Transport of Sound in Coupled Cavities of a Modified Honeycomb Lattice", J. Phys.: Condens. Matter **30**, 345401 (2018) (cited on page 18).

[61] M. Miniaci, R. K. Pal, B. Morvan, and M. Ruzzene, "Experimental Observation of Topologically Protected Helical Edge Modes in Patterned Elastic Plates", Phys. Rev. X **8**, 031074 (2018) (cited on page 18).

[62] R. Chaunsali, C.-W. Chen, and J. Yang, "Experimental Demonstration of Topological Waveguiding in Elastic Plates with Local Resonators", New J. Phys. **20**, 113036 (2018) (cited on page 18).

[63] S.-Y. Yu, C. He, Z. Wang, F.-K. Liu, X.-C. Sun, Z. Li, H.-Z. Lu, M.-H. Lu, X.-P. Liu, and Y.-F. Chen, "Elastic Pseudospin Transport for Integratable Topological Phononic Circuits", Nat. Commun. **9**, 3072 (2018) (cited on page 18).

[64] M. Xiao, W.-J. Chen, W.-Y. He, and C. T. Chan, "Synthetic Gauge Flux and Weyl Points in Acoustic Systems", Nat. Phys. **11**, 920–924 (2015) (cited on page 18).

[65] F. Li, X. Huang, J. Lu, J. Ma, and Z. Liu, "Weyl Points and Fermi Arcs in a Chiral Phononic Crystal", Nat. Phys. **14**, 30–34 (2018) (cited on page 18).

[66] M. Weiner, X. Ni, M. Li, A. Alù, and A. B. Khanikaev, "Demonstration of a Third-Order Hierarchy of Topological States in a Three-Dimensional Acoustic Metamaterial", Sci. Adv. **6**, eaay4166 (2020) (cited on page 18).

[67] C. L. Kane and T. C. Lubensky, "Topological Boundary Modes in Isostatic Lattices", Nat. Phys. **10**, 39 (2014) (cited on pages 18, 30).

[68] A. J. Heeger, S. Kivelson, J. R. Schrieffer, and W. .-. Su, "Solitons in Conducting Polymers", Rev. Mod. Phys. **60**, 781–850 (1988) (cited on page 19).

[69] J. Schmalian, "On the Quantization of the Zak Phase", Pers. Notes (2018) (cited on pages 26, 116).

[70] M. Atala, M. Aidelsburger, J. T. Barreiro, D. Abanin, T. Kitagawa, E. Demler, and I. Bloch, "Direct Measurement of the Zak Phase in Topological Bloch Bands", Nat. Phys. **9**, 795–800 (2013) (cited on pages 27, 30).

[71] H. Chen, H. Nassar, and G. L. Huang, "A Study of Topological Effects in 1D and 2D Mechanical Lattices", J. Mech. Phys. Solids **117**, 22–36 (2018) (cited on page 29).

[72] M. J. Rice and E. J. Mele, "Elementary Excitations of a Linearly Conjugated Diatomic Polymer", Phys. Rev. Lett. **49**, 1455–1459 (1982) (cited on page 30).

[73] C. W. Ling, M. Xiao, C. T. Chan, S. F. Yu, and K. H. Fung, "Topological Edge Plasmon Modes between Diatomic Chains of Plasmonic Nanoparticles", Opt. Express, OE **23**, 2021–2031 (2015) (cited on page 30).

[74] Q. Cheng, Y. Pan, Q. Wang, T. Li, and S. Zhu, "Topologically Protected Interface Mode in Plasmonic Waveguide Arrays", Laser Photonics Rev. **9**, 392–398 (2015) (cited on page 30).

[75] B. Midya and L. Feng, "Topological Multiband Photonic Superlattices", Phys. Rev. A **98**, 043838 (2018) (cited on page 30).

[76] C. E. Whittaker, E. Cancellieri, P. M. Walker, B. Royall, L. E. Tapia Rodriguez, E. Clarke, D. M. Whittaker, H. Schomerus, M. S. Skolnick, and D. N. Krizhanovskii, "Effect of Photonic Spin-Orbit Coupling on the Topological Edge Modes of a Su-Schrieffer-Heeger Chain", Phys. Rev. B **99**, 081402 (2019) (cited on page 30).

[77] Z. Yang, F. Gao, and B. Zhang, "Topological Water Wave States in a One-Dimensional Structure", Sci. Rep. **6**, 29202 (2016) (cited on page 30).

[78] M. Xiao, G. Ma, Z. Yang, P. Sheng, Z. Q. Zhang, and C. T. Chan, "Geometric Phase and Band Inversion in Periodic Acoustic Systems", Nat. Phys. **11**, 240–244 (2015) (cited on pages 30, 38).

[79] R. Chaunsali, E. Kim, A. Thakkar, P. G. Kevrekidis, and J. Yang, "Demonstrating an In Situ Topological Band Transition in Cylindrical Granular Chains", Phys. Rev. Lett. **119**, 024301 (2017) (cited on page 30).

[80] X. Li, Y. Meng, X. Wu, S. Yan, Y. Huang, S. Wang, and W. Wen, "Su-Schrieffer-Heeger Model Inspired Acoustic Interface States and Edge States", Appl. Phys. Lett. **113**, 203501 (2018) (cited on page 30).

[81] D. Zhao, M. Xiao, C. W. Ling, C. T. Chan, and K. H. Fung, "Topological Interface Modes in Local Resonant Acoustic Systems", Phys. Rev. B **98**, 014110 (2018) (cited on page 30).

[82] D. J. Apigo, W. Cheng, K. F. Dobiszewski, E. Prodan, and C. Prodan, "Observation of Topological Edge Modes in a Quasiperiodic Acoustic Waveguide", Phys. Rev. Lett. **122**, 095501 (2019) (cited on page 30).

[83] I. Kim, S. Iwamoto, and Y. Arakawa, "Topologically Protected Elastic Waves in One-Dimensional Phononic Crystals of Continuous Media", Appl. Phys. Express **11**, 017201 (2017) (cited on page 30).

[84] J. Yin, M. Ruzzene, J. Wen, D. Yu, L. Cai, and L. Yue, "Band Transition and Topological Interface Modes in 1D Elastic Phononic Crystals", Sci. Rep. **8**, 6806 (2018) (cited on page 30).

[85] H. Zhang, B. Liu, X. Zhang, Q. Wu, and X. Wang, "Zone Folding Induced Tunable Topological Interface States in One-Dimensional Phononic Crystal Plates", Phys. Lett. A **383**, 2797–2801 (2019) (cited on page 30).

[86] L.-Y. Zheng, V. Achilleos, O. Richoux, G. Theocharis, and V. Pagneux, "Observation of Edge Waves in a Two-Dimensional Su-Schrieffer-Heeger Acoustic Network", Phys. Rev. Applied **12**, 034014 (2019) (cited on page 30).

[87] Y. Hadad, V. Vitelli, and A. Alu, "Solitons and Propagating Domain Walls in Topological Resonator Arrays", ACS Photonics **4**, 1974–1979 (2017) (cited on page 30).

[88] S. D. Huber, "Topological Mechanics", Nat. Phys. **12**, 621–623 (2016) (cited on page 30).

[89] F. R. Blom, S. Bouwstra, M. Elwenspoek, and J. H. J. Fluitman, "Dependence of the Quality Factor of Micromachined Silicon Beam Resonators on Pressure and Geometry", J. Vac. Sci. Technol. B **10**, 19–26 (1992) (cited on page 32).

[90] J. Schmalian, "On the Role of Dissipation in Topological Mechanical Materials", Pers. Notes (2021) (cited on page 32).

[91] Y. Ashida, Z. Gong, and M. Ueda, "Non-Hermitian Physics", Adv. Phys. **69**, 249–435 (2020) (cited on page 32).

[92] D. C. Brody, "Biorthogonal Quantum Mechanics", J. Phys. A: Math. Theor. **47**, 035305 (2013) (cited on page 33).

[93] J. C. Garrison and E. M. Wright, "Complex Geometrical Phases for Dissipative Systems", Phys. Lett. A **128**, 177–181 (1988) (cited on page 33).

[94] K. Esaki, M. Sato, K. Hasebe, and M. Kohmoto, "Edge States and Topological Phases in Non-Hermitian Systems", Phys. Rev. B **84**, 205128 (2011) (cited on page 33).

[95] S. Lieu, "Topological Phases in the Non-Hermitian Su-Schrieffer-Heeger Model", Phys. Rev. B **97**, 045106 (2018) (cited on pages 33, 34).

[96] M. Wagner, F. Dangel, H. Cartarius, J. Main, and G. Wunner, "Numerical Calculation of the Complex Berry Phase in Non-Hermitian Systems", Acta Polytech. **57**, 470–476 (2017) (cited on page 33).

[97] F. Dangel, M. Wagner, H. Cartarius, J. Main, and G. Wunner, "Topological Invariants in Dissipative Extensions of the Su-Schrieffer-Heeger Model", Phys. Rev. A **98**, 013628 (2018) (cited on page 34).

[98] P. Haupt, *Continuum Mechanics and Theory of Materials*, 2nd ed., Advanced Texts in Physics (Springer-Verlag, Berlin Heidelberg, 2002) (cited on pages 34, 36).

[99] W. S. Slaughter, *The Linearized Theory of Elasticity* (Birkhäuser, Basel, 2002) (cited on page 34).

[100] A. F. (U. Bower, *Applied Mechanics of Solids*, 1st ed. (Taylor & Francis Inc, Boca Raton, 2009), 820 pp. (cited on pages 34, 35, 37, 118, 119).

[101] S. P. Timoshenko and J. N. Goodier, *Theory of Elasticity*, Vol. Engineering societies monographs (McGraw-Hill Education Pvt Limited, New York Toronto London, 2010) (cited on page 35).

[102] H. A. Barnes, J. F. Hutton, and K. Walters, *An Introduction to Rheology* (Elsevier Science Publishing Co Inc, Amsterdam New York, 1989), 212 pp. (cited on page 36).

[103] K.-J. Bathe, *Finite Element Procedures*, second edition (Klaus-Jürgen Bathe, Watertown, 2014), 1043 pp. (cited on pages 37, 118).

[104] J. Köpfler, T. Frenzel, M. Kadic, J. Schmalian, and M. Wegener, "Topologically Protected Twist Edge States for a Resonant Mechanical Laser-Beam Scanner", Phys. Rev. Applied **11**, 034059 (2019) (cited on pages 41, 47, 49, 51, 53, 57, 60).

[105] R. M. Walser, "Electromagnetic Metamaterials", in Complex Mediums II: Beyond Linear Isotropic Dielectrics, Vol. 4467 (July 9, 2001), pp. 1–15 (cited on page 42).

[106] M. Kadic, T. Bückmann, R. Schittny, and M. Wegener, "Metamaterials beyond Electromagnetism", Rep. Prog. Phys. **76**, 126501 (2013) (cited on page 42).

[107] M. Wegener, "Metamaterials Beyond Optics", Science **342**, 939–940 (2013) (cited on page 42).

[108] H. Chen, C. T. Chan, and P. Sheng, "Transformation Optics and Metamaterials", Nat. Mater. **9**, 387–396 (2010) (cited on page 42).

[109] T. J. Cui, D. Smith, and R. Liu, eds., *Metamaterials: Theory, Design, and Applications* (Springer Science+Business Media, Boston, 2010) (cited on page 42).

[110] C. M. Soukoulis and M. Wegener, "Past Achievements and Future Challenges in the Development of Three-Dimensional Photonic Metamaterials", Nat. Photonics **5**, 523–530 (2011) (cited on page 42).

[111] S. A. Cummer, J. Christensen, and A. Alù, "Controlling Sound with Acoustic Metamaterials", Nat. Rev. Mater. **1**, 1–13 (2016) (cited on page 42).

[112] A. A. Zadpoor, "Mechanical Meta-Materials", Mater. Horiz. **3**, 371–381 (2016) (cited on page 42).

[113] J. Christensen, M. Kadic, O. Kraft, and M. Wegener, "Vibrant Times for Mechanical Metamaterials", MRS Commun. **5**, 453–462 (2015) (cited on page 42).

[114] J. U. Surjadi, L. Gao, H. Du, X. Li, X. Xiong, N. X. Fang, and Y. Lu, "Mechanical Metamaterials and Their Engineering Applications", Adv. Eng. Mater. **21**, 1800864 (2019) (cited on pages 42, 112).

[115] R. A. Shelby, D. R. Smith, and S. Schultz, "Experimental Verification of a Negative Index of Refraction", Science **292**, 77–79 (2001) (cited on page 42).

[116] G. Dolling, M. Wegener, C. M. Soukoulis, and S. Linden, "Negative-Index Metamaterial at 780 Nm Wavelength", Opt. Lett., OL **32**, 53–55 (2007) (cited on page 42).

[117] R. Schittny, M. Kadic, S. Guenneau, and M. Wegener, "Experiments on Transformation Thermodynamics: Molding the Flow of Heat", Phys. Rev. Lett. **110**, 195901 (2013) (cited on page 42).

[118] M. Briane and G. W. Milton, "Homogenization of the Three-dimensional Hall Effect and Change of Sign of the Hall Coefficient", Arch. Rational. Mech. Anal. **193**, 715–736 (2009) (cited on page 42).

[119] M. Kadic, R. Schittny, T. Bückmann, C. Kern, and M. Wegener, "Hall-Effect Sign Inversion in a Realizable 3D Metamaterial", Phys. Rev. X **5**, 021030 (2015) (cited on page 42).

[120] C. Kern, M. Kadic, and M. Wegener, "Experimental Evidence for Sign Reversal of the Hall Coefficient in Three-Dimensional Metamaterials", Phys. Rev. Lett. **118**, 016601 (2017) (cited on page 42).

[121] X. Zhang, A. Vyatskikh, H. Gao, J. R. Greer, and X. Li, "Lightweight, Flaw-Tolerant, and Ultrastrong Nanoarchitected Carbon", PNAS **116**, 6665–6672 (2019) (cited on page 42).

[122] G. N. Greaves, A. L. Greer, R. S. Lakes, and T. Rouxel, "Poisson's Ratio and Modern Materials", Nat. Mater. **10**, 823–837 (2011) (cited on page 42).

[123] T. Bückmann, R. Schittny, M. Thiel, M. Kadic, G. W. Milton, and M. Wegener, "On Three-Dimensional Dilational Elastic Metamaterials", New J. Phys. **16**, 033032 (2014) (cited on page 42).

[124] M. Yang, S. Chen, C. Fu, and P. Sheng, "Optimal Sound-Absorbing Structures", Mater. Horiz. **4**, 673–680 (2017) (cited on page 42).

[125] T. Frenzel, C. Findeisen, M. Kadic, P. Gumbsch, and M. Wegener, "Tailored Buckling Microlattices as Reusable Light-Weight Shock Absorbers", Adv. Mater. **28**, 5865–5870 (2016) (cited on page 42).

[126] J. Qu, M. Kadic, A. Naber, and M. Wegener, "Micro-Structured Two-Component 3D Metamaterials with Negative Thermal-Expansion Coefficient from Positive Constituents", Sci. Rep. **7**, 40643 (2017) (cited on pages 42, 87, 88).

[127] J. Qu, M. Kadic, and M. Wegener, "Poroelastic Metamaterials with Negative Effective Static Compressibility", Appl. Phys. Lett. **110**, 171901 (2017) (cited on page 42).

[128] R. V. Craster, J. Kaplunov, and A. V. Pichugin, "High-Frequency Homogenization for Periodic Media", Proc. R. Soc. Math. Phys. Eng. Sci. **466**, 2341–2362 (2010) (cited on page 42).

[129] T. W. Kelvin, "The Second Robert Boyle Lecture", J. Oxf. Jr. Sci. Club **18** (1894) (cited on page 43).

[130] L. L. Whyte, "Chirality", Nature **180**, 513–513 (1957) (cited on page 43).

[131] L. L. Whyte, "Chirality", Nature **182**, 198–198 (1958) (cited on page 43).

[132] J. Reinbold, T. Frenzel, A. Münchinger, and M. Wegener, "The Rise of (Chiral) 3D Mechanical Metamaterials", Materials **12**, 3527 (2019) (cited on pages 43, 58, 121).

[133] L. A. Nguyen, H. He, and C. Pham-Huy, "Chiral Drugs: An Overview", Int. J. Biomed. Sci. **2**, 85–100 (2006) (cited on page 43).

[134] M. Kadic, A. Diatta, T. Frenzel, S. Guenneau, and M. Wegener, "Static Chiral Willis Continuum Mechanics for Three-Dimensional Chiral Mechanical Metamaterials", Phys. Rev. B **99**, 214101 (2019) (cited on page 43).

[135] R. S. Lakes and R. L. Benedict, "Noncentrosymmetry in Micropolar Elasticity", Int. J. Eng. Sci. **20**, 1161–1167 (1982) (cited on page 43).

[136] A. C. Eringen, *Microcontinuum Field Theories: I. Foundations and Solids*, Microcontinuum Field Theories (Springer Science+Business Media, New York, 1999) (cited on page 44).

[137] J. Köpfler, T. Frenzel, J. Schmalian, and M. Wegener, "Fused-Silica 3D Chiral Metamaterials via Helium-Assisted Microcasting Supporting Topologically Protected Twist Edge Resonances with High Mechanical Quality Factors", Adv. Mater. 33, 2103205 (2021) (cited on pages 45, 49, 50, 57, 67, 70, 76, 79, 81, 85, 91–94, 96, 98–100).

[138] C. S. Ha, M. E. Plesha, and R. S. Lakes, "Chiral Three-Dimensional Lattices with Tunable Poisson's Ratio", Smart Mater. Struct. 25, 054005 (2016) (cited on pages 58, 121).

[139] C. S. Ha, M. E. Plesha, and R. S. Lakes, "Chiral Three-Dimensional Isotropic Lattices with Negative Poisson's Ratio", Phys. Status Solidi B 253, 1243–1251 (2016) (cited on pages 58, 121).

[140] P. Patimisco, A. Sampaolo, V. Mackowiak, H. Rossmadl, A. Cable, F. K. Tittel, and V. Spagnolo, "Loss Mechanisms Determining the Quality Factors in Quartz Tuning Forks Vibrating at the Fundamental and First Overtone Modes", IEEE Trans. Ultrason. Ferroelectr. Freq. Control 65, 1951–1957 (2018) (cited on pages 64, 90, 94).

[141] Y.-H. Park and K. Park, "High-Fidelity Modeling of MEMS Resonators. Part I. Anchor Loss Mechanisms through Substrate", J. Microelectromech. Syst. 13, 238–247 (2004) (cited on pages 64, 94).

[142] M. Fukuhara, A. Sanpei, and K. Shibuki, "Low Temperature-Elastic Moduli, Debye Temperature and Internal Dilational and Shear Frictions of Fused Quartz", J. Mater. Sci. 32, 1207–1211 (1997) (cited on pages 65, 93).

[143] N. P. Bansal and R. H. Doremus, "Handbook of Glass Properties", (1986) (cited on pages 65, 93).

[144] T. Baldacchini, Three-Dimensional Microfabrication Using Two-Photon Polymerization: Fundamentals, Technology, and Applications (William Andrew, Amsterdam Boston, 2015), 512 pp. (cited on pages 68, 70).

[145] V. Hahn, F. Mayer, M. Thiel, and M. Wegener, "3-D Laser Nanoprinting", OPN 30, 28–35 (2019) (cited on pages 68, 70, 72).

[146] Y. Lakhdar, C. Tuck, J. Binner, A. Terry, and R. Goodridge, "Additive Manufacturing of Advanced Ceramic Materials", Prog. Mater. Sci. 116, 100736 (2021) (cited on page 68).

[147] A. Reiser, L. Koch, K. A. Dunn, T. Matsuura, F. Iwata, O. Fogel, Z. Kotler, N. Zhou, K. Charipar, A. Piqué, P. Rohner, D. Poulikakos, S. Lee, S. K. Seol, I. Utke, C. van Nisselroy, T. Zambelli, J. M. Wheeler, and R. Spolenak, "Metals by Micro-Scale Additive Manufacturing: Comparison of Microstructure and Mechanical Properties", Adv. Funct. Mater. 30, 1910491 (2020) (cited on page 68).

[148] D. Zhang, X. Liu, and J. Qiu, "3D Printing of Glass by Additive Manufacturing Techniques: A Review", Front. Optoelectron. **14**, 263–277 (2021) (cited on page 68).

[149] M. Vaezi, H. Seitz, and S. Yang, "A Review on 3D Micro-Additive Manufacturing Technologies", Int. J. Adv. Manuf. Technol. **67**, 1721–1754 (2013) (cited on page 68).

[150] M. A. Gibson, N. M. Mykulowycz, J. Shim, R. Fontana, P. Schmitt, A. Roberts, J. Ketkaew, L. Shao, W. Chen, P. Bordeenithikasem, J. S. Myerberg, R. Fulop, M. D. Verminski, E. M. Sachs, Y.-M. Chiang, C. A. Schuh, A. John Hart, and J. Schroers, "3D Printing Metals like Thermoplastics: Fused Filament Fabrication of Metallic Glasses", Mater. Today **21**, 697–702 (2018) (cited on page 68).

[151] L. Hirt, A. Reiser, R. Spolenak, and T. Zambelli, "Additive Manufacturing of Metal Structures at the Micrometer Scale", Adv. Mater. **29**, 1604211 (2017) (cited on page 68).

[152] A. Vyatskikh, S. Delalande, A. Kudo, X. Zhang, C. M. Portela, and J. R. Greer, "Additive Manufacturing of 3D Nano-Architected Metals", Nat. Commun. **9**, 593 (2018) (cited on page 68).

[153] D. W. Yee, M. L. Lifson, B. W. Edwards, and J. R. Greer, "Additive Manufacturing of 3D-Architected Multifunctional Metal Oxides", Adv. Mater. **31**, 1901345 (2019) (cited on page 68).

[154] D. Gailevičius, V. Padolskytė, L. Mikoliūnaitė, S. Šakirzanovas, S. Juodkazis, and M. Malinauskas, "Additive-Manufacturing of 3D Glass-Ceramics down to Nanoscale Resolution", Nanoscale Horiz. **4**, 647–651 (2019) (cited on page 68).

[155] H. Cui, R. Hensleigh, D. Yao, D. Maurya, P. Kumar, M. G. Kang, S. Priya, and X. (Zheng, "Three-Dimensional Printing of Piezoelectric Materials with Designed Anisotropy and Directional Response", Nat. Mater. **18**, 234–241 (2019) (cited on pages 68, 84).

[156] F. Kotz, K. Arnold, W. Bauer, D. Schild, N. Keller, K. Sachsenheimer, T. M. Nargang, C. Richter, D. Helmer, and B. E. Rapp, "Three-Dimensional Printing of Transparent Fused Silica Glass", Nature **544**, 337–339 (2017) (cited on page 68).

[157] I. Cooperstein, E. Shukrun, O. Press, A. Kamyshny, and S. Magdassi, "Additive Manufacturing of Transparent Silica Glass from Solutions", ACS Appl. Mater. Interfaces **10**, 18879–18885 (2018) (cited on page 68).

[158] D. G. Moore, L. Barbera, K. Masania, and A. R. Studart, "Three-Dimensional Printing of Multicomponent Glasses Using Phase-Separating Resins", Nat. Mater. **19**, 212–217 (2020) (cited on page 68).

[159] F. Kotz, A. S. Quick, P. Risch, T. Martin, T. Hoose, M. Thiel, D. Helmer, and B. E. Rapp, "Two-Photon Polymerization of Nanocomposites for the Fabrication of Transparent Fused Silica Glass Microstructures", Adv. Mater. 33, 2006341 (2021) (cited on pages 68, 69).

[160] X. Wen, B. Zhang, W. Wang, F. Ye, S. Yue, H. Guo, G. Gao, Y. Zhao, Q. Fang, C. Nguyen, X. Zhang, J. Bao, J. T. Robinson, P. M. Ajayan, and J. Lou, "3D-printed Silica with Nanoscale Resolution", Nat. Mater., 1–6 (2021) (cited on page 68).

[161] F. Kotz, K. Plewa, W. Bauer, N. Schneider, N. Keller, T. Nargang, D. Helmer, K. Sachsenheimer, M. Schäfer, M. Worgull, C. Greiner, C. Richter, and B. E. Rapp, "Liquid Glass: A Facile Soft Replication Method for Structuring Glass", Adv. Mater. 28, 4646–4650 (2016) (cited on pages 69, 76, 77).

[162] F. Kotz, N. Schneider, A. Striegel, A. Wolfschläger, N. Keller, M. Worgull, W. Bauer, D. Schild, M. Milich, C. Greiner, D. Helmer, and B. E. Rapp, "Glassomer—Processing Fused Silica Glass Like a Polymer", Adv. Mater. 30, 1707100 (2018) (cited on pages 69, 76).

[163] F. Kotz, P. Risch, K. Arnold, S. Sevim, J. Puigmartí-Luis, A. Quick, M. Thiel, A. Hrynevich, P. D. Dalton, D. Helmer, and B. E. Rapp, "Fabrication of Arbitrary Three-Dimensional Suspended Hollow Microstructures in Transparent Fused Silica Glass", Nat. Commun. 10, 1–7 (2019) (cited on pages 69, 79, 80).

[164] S. Kawata, H.-B. Sun, T. Tanaka, and K. Takada, "Finer Features for Functional Microdevices", Nature 412, 697–698 (2001) (cited on page 70).

[165] T. Bückmann, N. Stenger, M. Kadic, J. Kaschke, A. Frölich, T. Kennerknecht, C. Eberl, M. Thiel, and M. Wegener, "Tailored 3D Mechanical Metamaterials Made by Dip-in Direct-Laser-Writing Optical Lithography", Adv. Mater. 24, 2710–2714 (2012) (cited on pages 71, 87).

[166] E. H. Waller and G. Von Freymann, "Spatio-Temporal Proximity Characteristics in 3D Micro-Printing via Multi-Photon Absorption", Polymers 8, 297 (2016) (cited on page 72).

[167] M. Thiel, J. Fischer, G. von Freymann, and M. Wegener, "Direct Laser Writing of Three-Dimensional Submicron Structures Using a Continuous-Wave Laser at 532 Nm", Appl. Phys. Lett. 97, 221102 (2010) (cited on page 72).

[168] J. Fischer and M. Wegener, "Three-Dimensional Optical Laser Lithography beyond the Diffraction Limit", Laser Photonics Rev. 7, 22–44 (2013) (cited on page 72).

[169] J. B. Mueller, J. Fischer, F. Mayer, M. Kadic, and M. Wegener, "Polymerization Kinetics in Three-Dimensional Direct Laser Writing", Adv. Mater. 26, 6566–6571 (2014) (cited on page 72).

[170] L. Yang, A. Münchinger, M. Kadic, V. Hahn, F. Mayer, E. Blasco, C. Barner-Kowollik, and M. Wegener, "On the Schwarzschild Effect in 3D Two-Photon Laser Lithography", Adv. Opt. Mater. 7, 1901040 (2019) (cited on page 72).

[171] Glassomer GmbH, *Safety Data Sheet Glassomer L40*, 2019 (cited on page 76).

[172] H. Lin and B. D. Freeman, "Gas Solubility, Diffusivity and Permeability in Poly(Ethylene Oxide)", J. Membr. Sci. 239, 105–117 (2004) (cited on page 77).

[173] J. Qu, A. Gerber, F. Mayer, M. Kadic, and M. Wegener, "Experiments on Metamaterials with Negative Effective Static Compressibility", Phys. Rev. X 7, 041060 (2017) (cited on pages 77, 87, 92).

[174] J. H. Spurk and N. Aksel, *Fluid Mechanics* (Springer-Verlag, Berlin Heidelberg, 2020) (cited on page 78).

[175] M. Malinauskas, A. Žukauskas, V. Purlys, K. Belazaras, A. Momot, D. Paipulas, R. Gadonas, A. Piskarskas, H. Gilbergs, A. Gaidukevičiūtė, I. Sakellari, M. Farsari, and S. Juodkazis, "Femtosecond Laser Polymerization of Hybrid/Integrated Micro-Optical Elements and Their Characterization", J. Opt. 12, 124010 (2010) (cited on page 83).

[176] T. Gissibl, S. Thiele, A. Herkommer, and H. Giessen, "Two-Photon Direct Laser Writing of Ultracompact Multi-Lens Objectives", Nat. Photonics 10, 554–560 (2016) (cited on page 83).

[177] L. Yang, F. Mayer, U. H. F. Bunz, E. Blasco, and M. Wegener, "Multi-Material Multi-Photon 3D Laser Micro- and Nanoprinting", Light: Adv. Manuf. 2, 1–17 (2021) (cited on page 83).

[178] L. F. Admaiai, P. Grange, B. Delmon, M. Cassart, and J. P. Issi, "Synthesis of Bulk and Film YBa2Cu3O7-x High-Temperature Superconductor by the Sol-Gel Method", J. Mater. Sci. 29, 5817–5825 (1994) (cited on page 84).

[179] M. Kakihana, "Invited Review "Sol-Gel" Preparation of High Temperature Superconducting Oxides", J. Sol-Gel Sci. Technol. 6, 7–55 (1996) (cited on page 84).

[180] T. L. Liu, X. Wen, Y.-C. Kung, and P.-Y. Chiou, "Fabrication Strategy for Micro Soft Robotics with Semiconductor Devices Integration", in 2017 IEEE 30th International Conference on Micro Electro Mechanical Systems (MEMS) (Jan. 2017), pp. 663–666 (cited on page 84).

[181] F. Rothermel, S. Thiele, C. Jung, H. Giessen, and A. Herkommer, "Towards Magnetically Actuated 3D-printed Micro-Optical Elements", in Optomechanics and Optical Alignment, Vol. 11816 (Aug. 1, 2021), pp. 134–142 (cited on page 84).

[182] B. Pan, K. Qian, H. Xie, and A. Asundi, "Two-Dimensional Digital Image Correlation for in-Plane Displacement and Strain Measurement: A Review", Meas. Sci. Technol. 20, 062001 (2009) (cited on page 87).

[183] J. Xavier, A. M. R. Sousa, J. J. L. Morais, V. M. J. Filipe, and M. A. Vaz, "Measuring Displacement Fields by Cross-Correlation and a Differential Technique: Experimental Validation", OE 51, 043602 (2012) (cited on page 87).

[184] J. Zhao, Y. Sang, and F. Duan, "The State of the Art of Two-Dimensional Digital Image Correlation Computational Method", Eng. Rep. 1, e12038 (2019) (cited on page 87).

[185] J. Qu, "On Thermoelastic and Poroelastic Metamaterials", PhD thesis (Karlsruher Institut für Technologie (KIT), Karlsruhe, 2018) (cited on pages 87, 92).

[186] C. Eberl, T. Thompson, D. Gianola, W. Sharpe Jr., and K. Hemker, "Digital Image Correlation and Tracking", MatLabCentral Mathworks File Exch. Serv. (2006) (cited on page 87).

[187] T. Frenzel, J. Köpfler, A. Naber, and M. Wegener, "Atomic Scale Displacements Detected by Optical Image Cross-Correlation Analysis and 3D Printed Marker Arrays", Sci. Rep. 11, 2304 (2021) (cited on pages 88, 96).

[188] J. L. Rouzic, P. Delobelle, P. Vairac, and B. Cretin, "Comparison of Three Different Scales Techniques for the Dynamic Mechanical Characterization of Two Polymers (PDMS and SU8)", Eur. Phys. J. Appl. Phys. 48, 11201 (2009) (cited on page 91).

[189] S. T. S. Holmström, U. Baran, and H. Urey, "MEMS Laser Scanners: A Review", J. Microelectromech. Syst. 23, 259–275 (2014) (cited on pages 104, 107).

[190] T. Iseki, M. Okumura, and T. Sugawara, "High-Speed and Wide-Angle Deflection Optical MEMS Scanner Using Piezoelectric Actuation", IEEJ Trans. Electr. Electron. Eng. 5, 361–368 (2010) (cited on page 108).

[191] S. Kotler, G. A. Peterson, E. Shojaee, F. Lecocq, K. Cicak, A. Kwiatkowski, S. Geller, S. Glancy, E. Knill, R. W. Simmonds, J. Aumentado, and J. D. Teufel, "Direct Observation of Deterministic Macroscopic Entanglement", Science 372, 622–625 (2021) (cited on page 112).

[192]   D. Obana, F. Liu, and K. Wakabayashi, "Topological Edge States in the Su-Schrieffer-Heeger Model", Phys. Rev. B **100**, 075437 (2019) (cited on page 112).

Acknowledgments

I would like to thank all the people that have contributed to this work in any form.

Werner Gilde from the electronics workshop. They took care of various issues, such as the layout and repair of voltage amplifiers, the contacting of piezoelectric transducers, and they keep the IT system and servers running. Last but not least, I would like thank Ursula Mösle, Claudia Alaya, Monika Brenkmann, Petra Bauer, Patricia Jäger, and Christine Fischer for arranging all the organizational issues in the secretariats at APH and INT.

Finally, I would like to thank my roommates, my family, and my girlfriend for their great support, not only during my PhD time.